

## **Supporting Information**

Lubna Salah<sup>a</sup>, Marc K. Etherington<sup>b,c\*</sup>, Ali Shuaib<sup>d</sup>, Andrew Danos<sup>c</sup>, Ahmed Abdel Nazeer<sup>a</sup>, Basma Ghazal<sup>a</sup>, Antonio Prlj<sup>e</sup>, Andrew T. Turley<sup>e</sup>, Abhijit Mallick<sup>e</sup>, Paul R. McGonigal<sup>e</sup>, Basile F. E. Curchod<sup>e</sup>, Andrew P. Monkman<sup>c</sup> and Saad Makhseed<sup>a\*</sup>

\*E-mail: [saad.makhseed@ku.edu.kw](mailto:saad.makhseed@ku.edu.kw), [marc.k.etherington@northumbria.ac.uk](mailto:marc.k.etherington@northumbria.ac.uk)

<sup>a</sup>Department of Chemistry, Faculty of Science, Kuwait University, P.O. Box 5969, Safat-13060, Kuwait.

<sup>b</sup>Department of Mathematics, Physics & Electrical Engineering, Northumbria University, Ellison Place, Newcastle upon Tyne, NE1 8ST, UK

<sup>c</sup>Department of Chemistry, Durham University, South Road, Durham, DH1 3LE, UK

<sup>d</sup>Biomedical Engineering Unit, Department of Physiology, Faculty of Medicine, Kuwait University, P.O. Box 24923, Safat-13110, Kuwait

<sup>e</sup>Department of Chemistry, Durham University, South Road, Durham, DH1 3LE, UK

## **Table of Contents**

1. General Methods	3
2. Synthetic Methods	6
3. $^1\text{H}$ and $^{13}\text{C}$ NMR Spectroscopic Characterization of Synthesized Compounds	9
4. Thermogravimetric Analysis	17
5. Cyclic Voltammetry	18
6. X-ray Crystallography	21
7. Steady-state Photophysical Characterization	35
8. Time-resolved Photophysical Characterization	38
9. Theoretical Study	70
10. References	76

## 1. General Methods

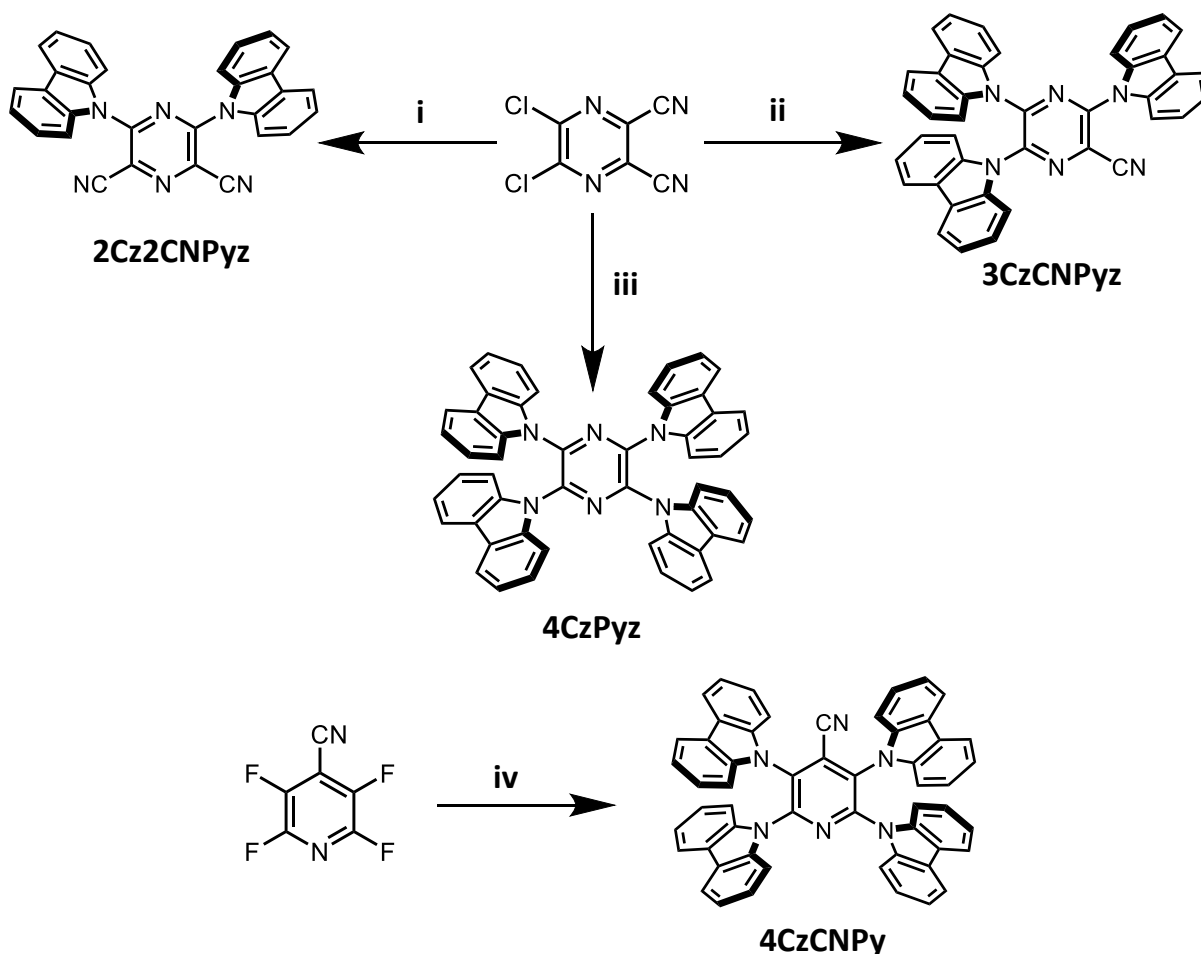
**Materials:** All reagents were used without further purification unless otherwise specified. 5,6-Dichloro-2,3-dicyanopyrazine {CAS No. 56413-95-7}, 2,3,5,6-Tetrafluoro-4-pyridinecarbonitrile {CAS No. 16297-07-7} and carbazole {CAS No. 86-74-8} were purchased from Sigma-Aldrich. Anhydrous solvents were either supplied from Sigma-Aldrich or dried as described by Perrin.<sup>1</sup> 4CzTPN was prepared according to the reported procedure.<sup>2,3</sup>

**Instrumentation and Analytical Techniques:** Thin-layer chromatography (TLC) was performed using Polygram sil G/UV 254 TLC plates and visualization was carried out by ultraviolet light at 254 nm and 350 nm. Column chromatography was performed using Merck silica gel 60 of mesh size 0.040 – 0.063 mm. Nuclear magnetic resonance (NMR) spectra were recorded using a Bruker Advance (III)-400 (<sup>1</sup>H 400.130 MHz and <sup>13</sup>C 100.613 MHz), spectrometer or a Bruker DPX 600 (<sup>1</sup>H 600.130 MHz and <sup>13</sup>C 150.903 MHz), at a constant temperature of 298 K. Chemical shifts ( $\delta$ ) are reported in parts per million (ppm) relative to the signals corresponding to residual non-deuterated solvents [CDCl<sub>3</sub>:  $\delta$  = 7.26 or 77.16, DMSO-d<sub>6</sub>:  $\delta$  = 2.50 or 39.52. Coupling constants ( $J$ ) are reported in Hertz (Hz). <sup>13</sup>C NMR Experiments were proton-decoupled. Assignments of <sup>1</sup>H and <sup>13</sup>C NMR signals were accomplished by two-dimensional NMR spectroscopy (COSY, NOESY, HSQC, HMBC). NMR spectra were processed using MestReNova version 11. Data are reported as follows: chemical shift; multiplicity; coupling constants; integral and assignment. High-resolution electrospray (HR-ESI) and ASAP (HR-ASAP) mass spectra were measured using a Waters LCT Premier XE high resolution, accurate mass UPLC ES MS (also with ASAP ion source) or on a Thermo GC-MS. IR spectra were obtained from a Jasco 6300 FTIR. UV-VIS studies were performed using a Shimadzu UV-3600 double beam spectrophotometer and steady-state photoluminescence spectra were obtained using a Jobin Yvon Fluorolog. Elemental analyses were carried out using an ElementarVario Micro Cube. Thermal analysis was performed using a Shimadzu DTG-60 and TMA-60H. X-ray single crystal data for **2Cz2CNPyz** and **3CzCNPyz** were collected on a Rigaku R-AXIS RAPID diffractometer

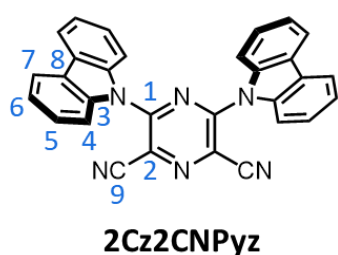
using filtered Mo-K $\alpha$  radiation. The structures were then solved by direct methods and expanded using Fourier techniques. X-ray single crystal data for **4CzPz** was measured on a Bruker X8 Prospector diffractometer, using CuK $\alpha$  radiation. The reflection frames were then integrated with the Bruker SAINT Software package using a narrow-frame algorithm. The calculations were performed using the 'Crystal Structure' crystallographic software package except for refinement, which was performed using SHELXL-97 and the structures were solved and refined using the Bruker SHELXTL Software Package. Crystallographic data for the structures has been deposited with the Cambridge Crystallographic Data Centre as supplementary publications CCDC-2007864-2007866. The X-ray single crystal data for **4CzCNPz** have been collected using  $\lambda$ MoK $\alpha$  radiation ( $\lambda = 0.71073 \text{ \AA}$ ) on a Bruker D8Venture (Photon100 CMOS detector,  $\mu$ S-microsource, focusing mirrors) diffractometer equipped with a Cryostream (Oxford Cryosystems) open-flow nitrogen cryostats at the temperature 120.0(2)K. The structures were solved by direct method and refined by full-matrix least squares on F<sup>2</sup> for all data using Olex2<sup>4</sup> and SHELXTL<sup>5</sup> software. All non-disordered non-hydrogen atoms were refined in anisotropic approximation, hydrogen atoms were placed in the calculated positions and refined in riding mode. Carbon atoms of the disordered DCM solvent molecules were refined isotropically with fixed SOF = 0.5. The C-Cl distances in disordered molecules were restrained to be similar (SADI). The structure was refined as a pseudo-merohedral twin (-1 0 0 0 -1 0 -1 0). Crystallographic data for the structure has been deposited with the Cambridge Crystallographic Data Centre as supplementary publication CCDC-2022458. The electrochemical properties of the pyrazine derivatives **2Cz2CNPz**, **3CzCNPz** and **4CzPz** were studied by cyclic voltammetry (CV) under inert atmosphere using glassy carbon as the working electrode, platinum wire as the counter electrode and SCE as the reference electrode. 0.1 M Tetrabutyl ammonium hexafluorophosphate solution was used as the supporting electrolyte and a concentration of  $10^{-4}$  M was used for the investigated compounds. The measurement was performed at a scan rate of  $50 \text{ mV s}^{-1}$ . The solutions were prepared at  $10 \text{ }\mu\text{M}$  concentration for absorption and photoluminescence measurements. The

zeonex films were drop cast from a mixture of the fluorophore and zeonex in toluene at the stated weight percentage and placed in a vacuum oven overnight. The DPEPO films were spin-coated from a mixture of fluorophore and DPEPO in chloroform at 2000 rpm. To perform the time-resolved measurements on the solutions, they were first degassed by five freeze-thaw cycles in a degassing cuvette. The films were placed in a cryostat and the measurements performed in vacuum at room temperature and under an inert nitrogen gas atmosphere at low temperature. The excitation pulses were provided by an Ekspla Nd:Yag laser at 355 nm and the emission collected after passing through a spectrograph on a Stanford Computer Optics ICCD camera to produce the time-resolved emission spectra. The laser fluence measurements were performed under 337 nm excitation by a (LTBMNL 100, Lasertechnik Berlin) nitrogen laser. The photoluminescence quantum yields of the systems were measured in 1 wt% zeonex and 10 wt% DPEPO host matrices using a Horiba Quanti-Phi integrating sphere and a Fluorolog-3.

## 2. Synthetic Methods



**Scheme S1.** Synthetic route used to prepare **2Cz2CNPyz**, **3CzCNPyz**, **4CzPyz** and **4CzCNPz**. Reagents and conditions: i) carbazole / Et<sub>3</sub>N / MeCN / rt / 24 h / 22%; ii) carbazole / CsF / DMF / rt / 16 h / 24%; iii) carbazole / CsF / DMF / 3 d / 130 °C / 2.5%; iv) carbazole / *n*-BuLi / THF / 0 → rt / 16 h / 60%.



**2Cz2CNPyz**

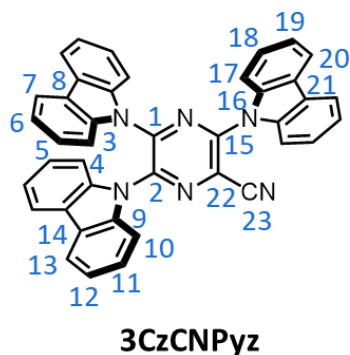
**3,5-Bis(9-carbazolyl)pyrazine-2,6-dicarbonitrile (2Cz2CNPyz):** 5,6-

Dichloro-2,3-dicyanopyrazine (1.0 g, 5.0 mmol) and carbazole (2.1 g, 12.5 mmol) were dissolved in anhydrous MeCN (20 mL) under a N<sub>2</sub>

atmosphere. Triethylamine (3.5 mL, 25.1 mmol) was then added to the

solution and the reaction mixture was allowed to stir for 24 h at room temperature. The solvent was removed under reduced pressure and the resulting crude mixture was purified by column chromatography, eluting with a 2:1 mixture of hexane/CH<sub>2</sub>Cl<sub>2</sub> to obtain **2Cz2CNPyz** as an orange solid (0.50 g, 1.1 mmol, 22%); **M.P.** 337 – 338 °C. <sup>1</sup>H NMR (400 MHz, DMSO-d<sub>6</sub>) δ 8.31 (d, *J* = 7.7 Hz, 4H, H<sub>7</sub>), 7.85 (d, *J* = 8.3 Hz, 4H, H<sub>4</sub>), 7.55 (m, 4H, H<sub>5</sub>), 7.46 (t, *J* = 7.7 Hz, 4H, H<sub>6</sub>). <sup>13</sup>C NMR (151 MHz, DMSO-d<sub>6</sub>) δ 150.2 (C<sub>1</sub>), 138.2 (C<sub>3</sub>), 126.7 (C<sub>5</sub>), 124.6 (C<sub>8</sub>), 123.3 (C<sub>6</sub>), 122.5 (C<sub>9</sub>), 120.9 (C<sub>7</sub>), 114.1 (C<sub>2</sub>), 112.4 (C<sub>4</sub>) **HR-**

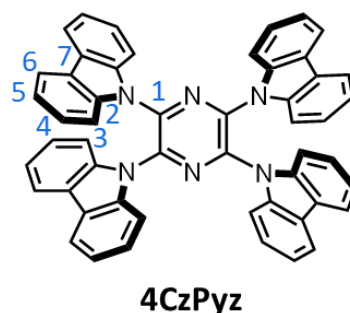
**ESI-MS**  $m/z = 460.1431 [M]^+$  (calculated for  $C_{30}H_{16}N_6 = 460.1431$ ). **Elemental analysis** calculated (%) for  $C_{30}H_{16}N_6$ : C, 78.25; H, 3.50; N, 18.25, Found: C, 78.40; H, 3.68; N, 18.16. **FT-IR**,  $\nu_{max}/cm^{-1}$  3434.60, 3060.48, 2920.88, 2852.2, 2231.24.



**3,5,6-Tris(9-carbazolyl)pyrazine-2-carbonitrile (3CzCNPyz):** 5,6-Dichloro-2,3-dicyanopyrazine (1.0 g, 5.0 mmol) and carbazole (2.6 g, 15.5 mmol) were dissolved in anhydrous DMF (30 mL) under a  $N_2$  atmosphere. Anhydrous CsF (3.8 g, 25.0 mmol) was then added to the solution and the reaction mixture was allowed to stir overnight at room temperature. The reaction mixture was then

diluted with  $H_2O$  until no further precipitation occurred. The precipitated compound was isolated using Buchner filtration. The crude solid material was then purified by column chromatography, eluting with a 2:1 mixture of hexane/ $CH_2Cl_2$  to obtain **3CzCNPyz** as a yellow solid (0.70 g, 1.2 mmol, 24% yield).

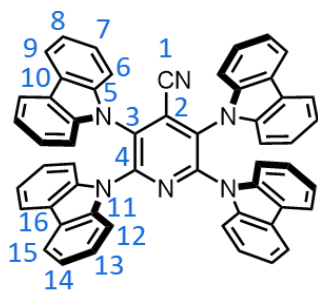
**M.P.** 232 – 233 °C.  **$^1H$  NMR** (400 MHz,  $DMSO-d_6$ )  $\delta$  8.34 (d,  $J = 7.8$  Hz, 2H,  $H_{13}$ ), 8.00 (m, 4H,  $H_{7+20}$ ), 7.94 (d,  $J = 7.7$  Hz, 2H,  $H_4$ ), 7.66 – 7.63 (m, 2H,  $H_{10}$ ), 7.60 (m, 2H,  $H_{12}$ ), 7.57 – 7.55 (m, 2H,  $H_{17}$ ), 7.46 (t,  $J = 7.5$  Hz, 2H,  $H_{11}$ ), 7.21 – 7.11 (m,  $H_6, H_{6+18+19}$ ), 7.04 (m, 2H,  $H_5$ ).  **$^{13}C$  NMR** (151 MHz,  $DMSO-d_6$ )  $\delta$  146.4 ( $C_2$ ), 143.7 ( $C_1$ ), 140.2 ( $C_{15}$ ), 139.3 ( $C_9$ ), 137.8 ( $C_3$ ), 137.6 ( $C_{16}$ ), 126.5 ( $C_{12}$ ), 125.9 ( $C_5$ ), 123.9 ( $C_6$ ), 123.9 ( $C_8$ ), 123.7 ( $C_{14}$ ), 122.1 ( $C_{21}$ ), 122.1 ( $C_{11}$ ), 121.9 ( $C_{22}$ ), 121.8 ( $C_{18}$ ), 121.7 ( $C_{13}$ ), 121.7 ( $C_{19}$ ), 120.2 ( $C_4$ ), 120.2 ( $C_{20}$ ), 114.8 ( $C_{23}$ ), 111.9 ( $C_7$ ), 111.4 ( $C_{17}$ ), 111.1 ( $C_{10}$ ). **HR-ESI-MS**  $m/z = 599.2917 [M]^+$  (calculated for  $C_{40}H_{25}N_6 = 599.2918$ ). **Elemental analysis** calculated (%) for  $C_{41}H_{24}N_6$ : C, 81.98; H, 4.03; N, 13.99, Found: C, 81.66; H, 4.66; N, 13.51. **FT-IR**,  $\nu_{max}/cm^{-1}$  3433.6, 3059.51, 2229.31, 1597.73.



**2,3,5,6-Tetrakis(9-carbazolyl)pyrazine (4CzPyz):** 5,6-Dichloro-2,3-dicyanopyrazine (1.0 g, 5.0 mmol) and carbazole (3.5 g, 20.9 mmol) were dissolved in anhydrous DMF (30 mL) under a  $N_2$  atmosphere. Anhydrous CsF (3.8 g, 25.0 mmol) was then added to the solution and the reaction mixture was heated to 130 °C for 3 d. After completion,

the reaction mixture was diluted in cold water and the precipitated material was then filtered out using

Buchner filtration. The crude product was purified by column chromatography, eluting with a 1:3 mixture of hexane/toluene to afford **4CzPyz** as a light green solid in (0.09 g, 0.12 mmol, 2.5 %). **M.P.** 453 – 454 °C.  $^1\text{H NMR}$  (400 MHz, DMSO- $d_6$ )  $\delta$  7.99 (m, 8H, H<sub>6</sub>), 7.81 (m, 8H, H<sub>3</sub>), 7.16 (m, 16H, H<sub>4+5</sub>).  $^{13}\text{C NMR}$  (151 MHz, DMSO- $d_6$ )  $\delta$  139.6 (C<sub>1</sub>), 138.6 (C<sub>2</sub>), 125.7 (C<sub>4</sub>), 123.5 (C<sub>7</sub>), 121.2 (C<sub>5</sub>), 120.1 (C<sub>6</sub>), 111.4 (C<sub>3</sub>). **HR-ESI-MS**  $m/z$  = 740.2671 [M]<sup>+</sup> (calculated for C<sub>52</sub>H<sub>32</sub>N<sub>6</sub> = 740.2688). **Elemental analysis** calculated (%) for C<sub>52</sub>H<sub>32</sub>N<sub>6</sub>: C, 84.30; H, 4.35; N, 11.34, Found: C, 80.81; H, 4.64; N, 10.50;



**4CzCNPY**

**4CzCNPY:** Carbazole (0.50 g, 2.84 mmol) in anhydrous THF (14 mL) was added to a two neck round bottom flask under a N<sub>2</sub> atmosphere. *n*-BuLi in hexanes (1.31 mL, 3.28 mmol) was added dropwise to the reaction flask at 0 °C leading to formation of a colourless precipitate. After complete addition, the reaction flask was warmed to room temperature

and stirred for 1 h. The reaction was then cooled back to 0 °C and solid 2,3,5,6-tetrafluoro-4-pyridinecarbonitrile (0.10 g, 0.57 mmol) was added in one portion. Immediately the colourless precipitate became a clear yellow solution. The reaction mixture was stirred at room temperature overnight and then quenched with a saturated aqueous solution of NH<sub>4</sub>Cl (5 mL) and extracted with CH<sub>2</sub>Cl<sub>2</sub> (100 mL). After removing the solvent under reduced pressure the crude product was purified by column chromatography (Teledyne Isco CombiFlash Rf+ system, 24 g SiO<sub>2</sub>, Hexane–EtOAc, gradient elution) using 7.5% EtOAc–Hexane as eluent to yield a yellow solid (0.261 g, 0.342 mmol, 60%). **M.P.** 380 – 382 °C.  $^1\text{H NMR}$  (400 MHz, Chloroform-*d*)  $\delta$  7.82 (dt,  $J$  = 7.5, 2.4 Hz, 4H, H<sub>15</sub>), 7.75 (d,  $J$  = 7.6 Hz, 4H, H<sub>9</sub>), 7.45 (dd,  $J$  = 8.0, 2.5 Hz, 4H, H<sub>12</sub>), 7.32 – 7.26 (m, 4H, H<sub>6</sub>), 7.23 – 7.16 (m, 8H, H<sub>8+14</sub>), 7.11 (dd,  $J$  = 8.6, 6.2 Hz, 4H, H<sub>13</sub>), 7.04 (m, 4H, H<sub>7</sub>).  $^{13}\text{C NMR}$  (151 MHz, Chloroform-*d*)  $\delta$  147.7 (C<sub>4</sub>), 138.6 (C<sub>11</sub>), 138.5 (C<sub>5</sub>), 130.3 (C<sub>3</sub>), 126.7 (C<sub>2</sub>), 126.1 (C<sub>14</sub>), 125.8 (C<sub>7</sub>), 124.5 (C<sub>10+16</sub>), 121.8 (C<sub>8</sub>), 121.7 (C<sub>13</sub>), 120.6 (C<sub>15</sub>), 120.1 (C<sub>9</sub>), 112.0 (C<sub>1</sub>), 110.6 (C<sub>12</sub>), 109.8 (C<sub>6</sub>). **HR-ESI-MS**  $m/z$  = 765.2759 [M+H]<sup>+</sup> (calculated for C<sub>54</sub>H<sub>33</sub>N<sub>6</sub> = 765.2761).

### 3. $^1\text{H}$ and $^{13}\text{C}$ NMR Spectroscopic Characterization of Synthesized Compounds

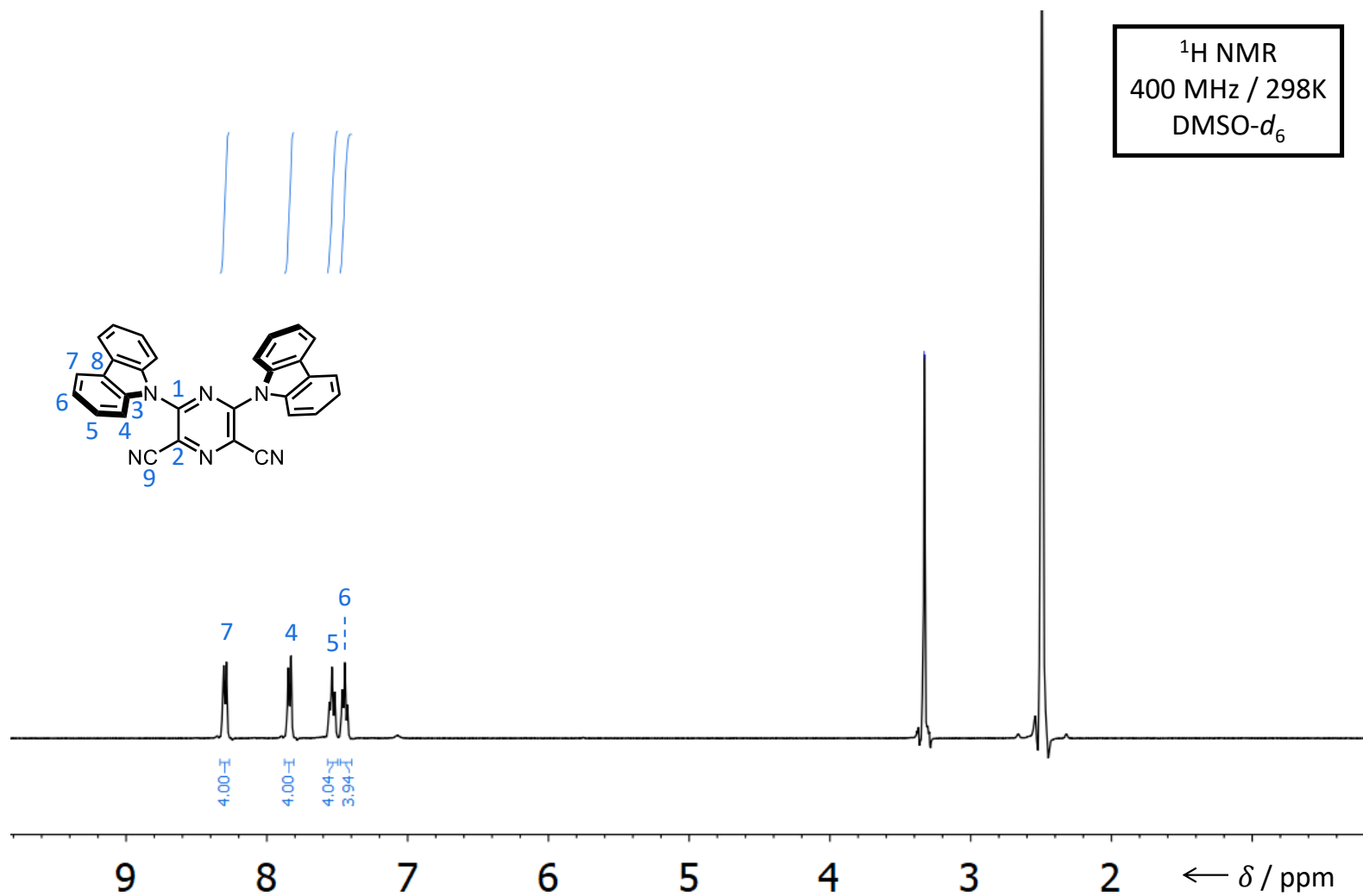


Figure S1  $^1\text{H}$  NMR spectrum of 2Cz2CNPyz in DMSO- $d_6$ .

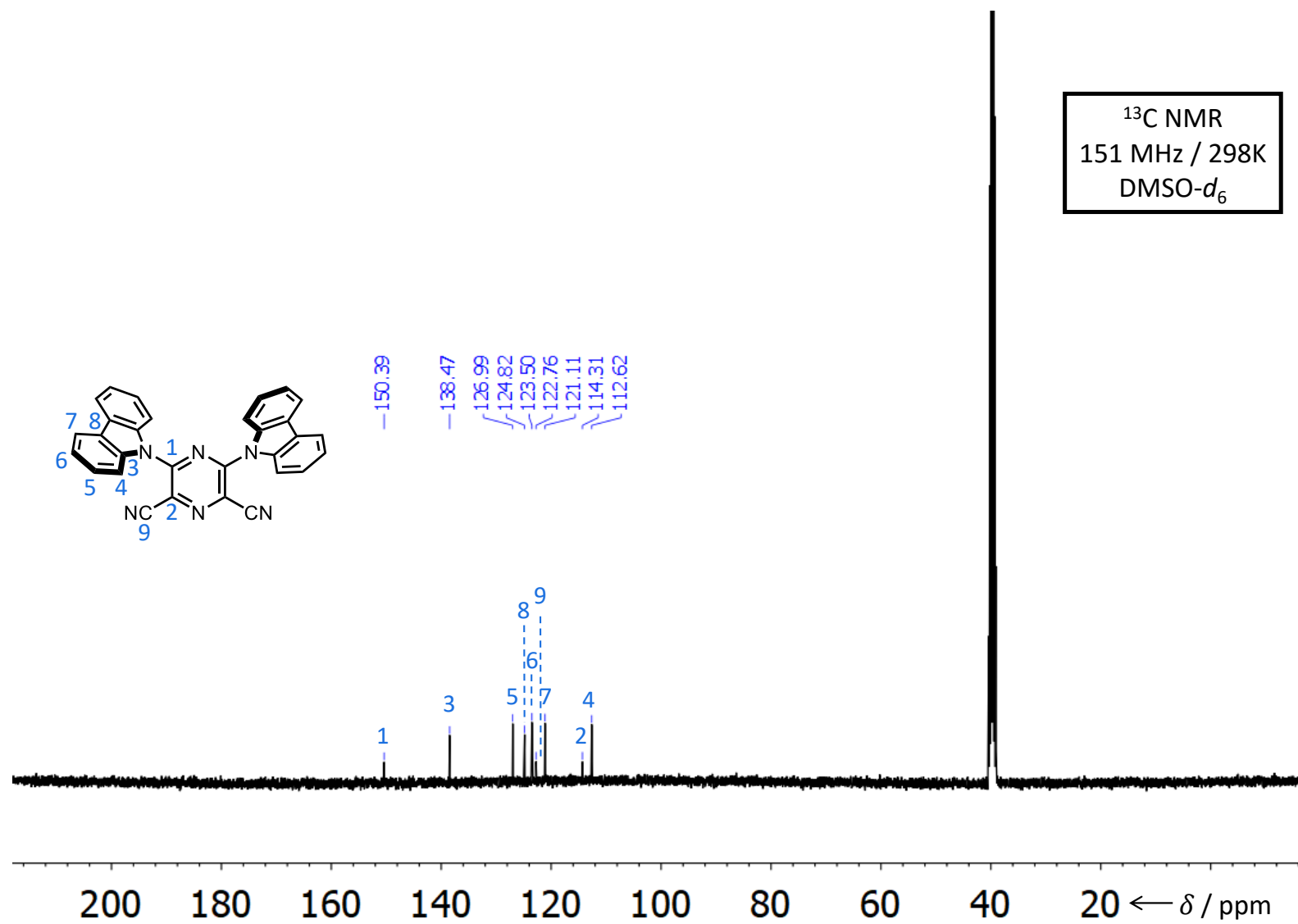


Figure S2 <sup>13</sup>C NMR spectrum of 2Cz2CNPyz in DMSO-*d*<sub>6</sub>.

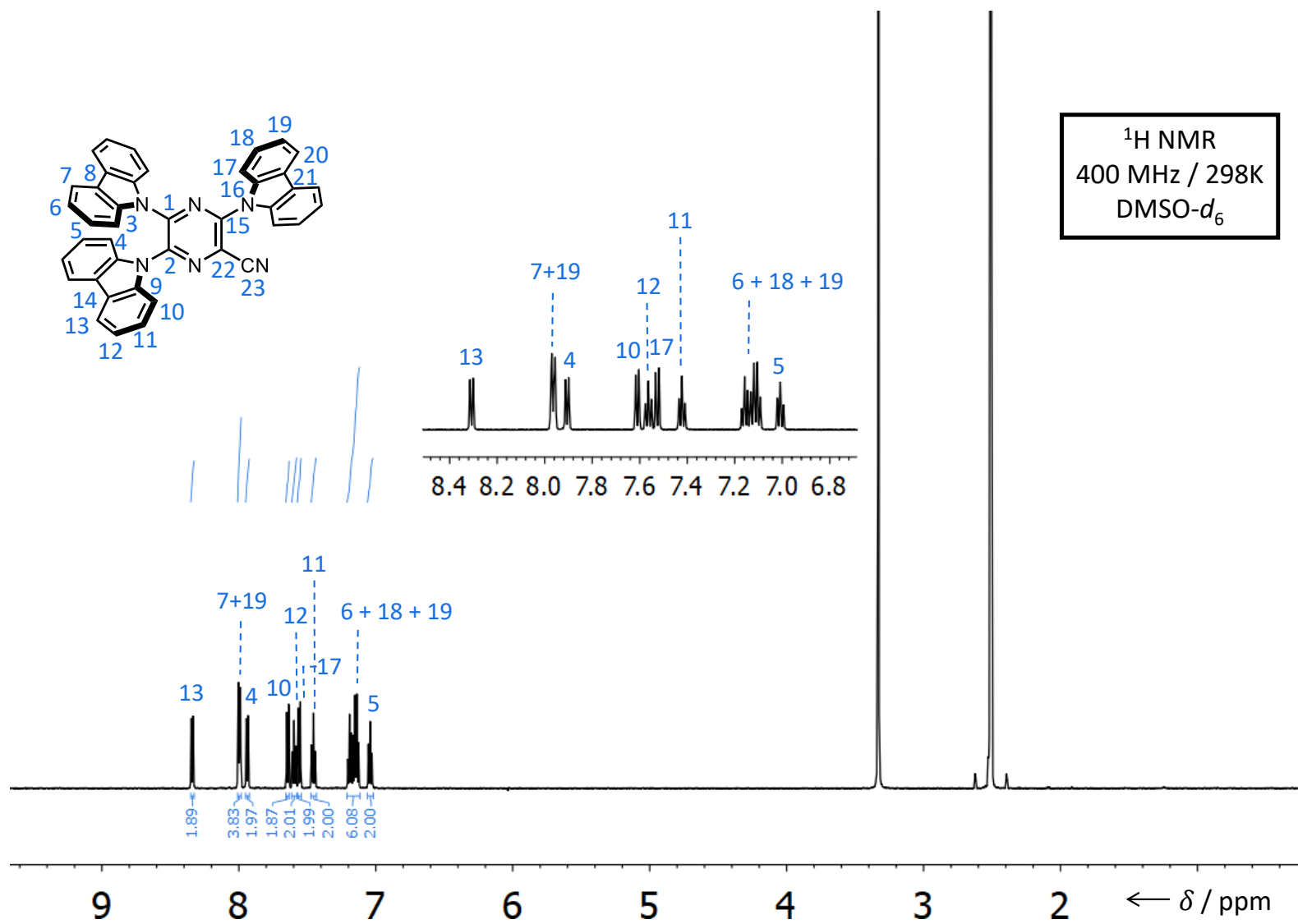


Figure S3 <sup>1</sup>H NMR spectrum of 3CzCNPyz in DMSO-*d*<sub>6</sub>.

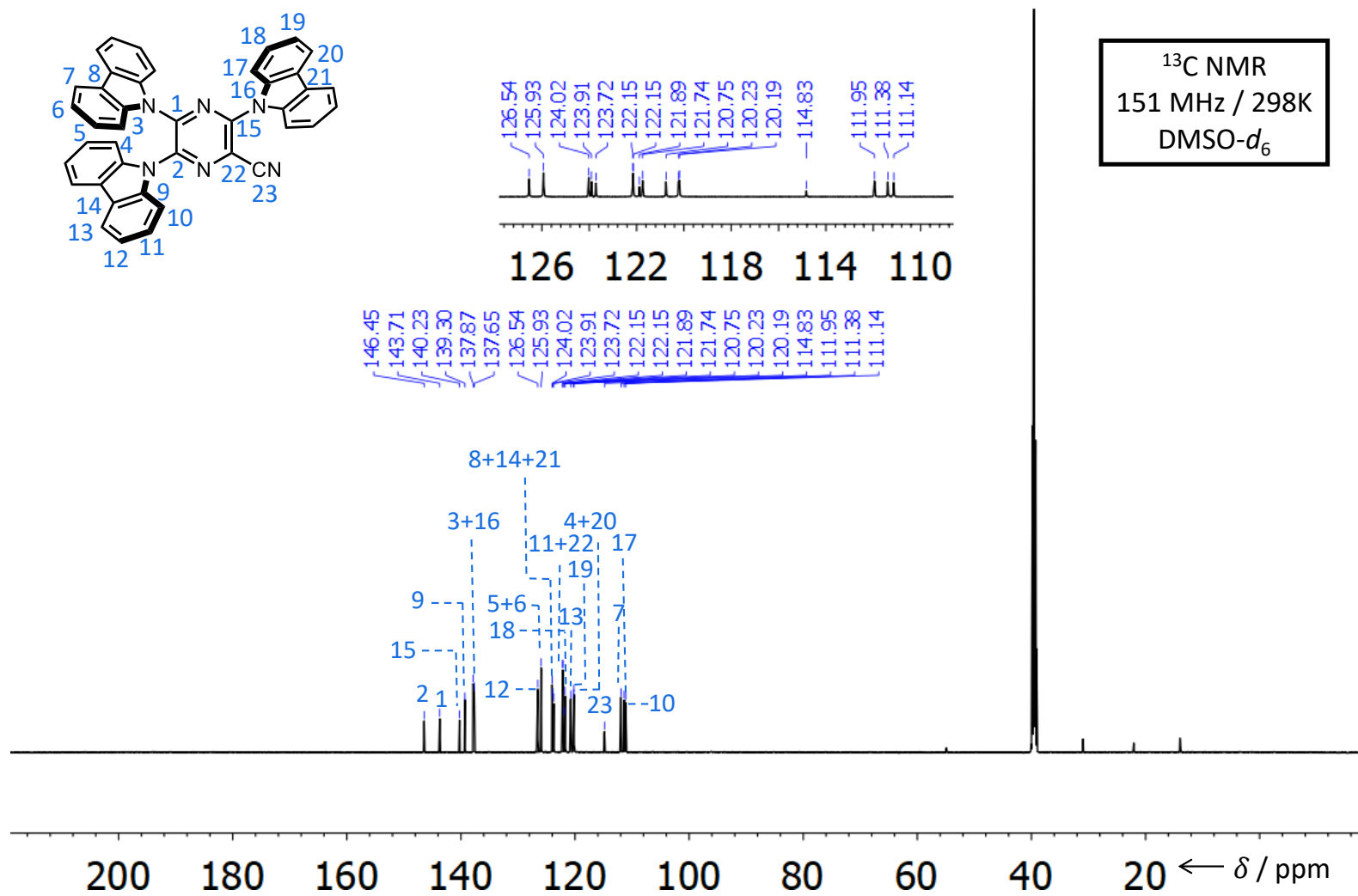


Figure S4 <sup>13</sup>C NMR spectrum of 3CzCNPyz in DMSO-*d*<sub>6</sub>.

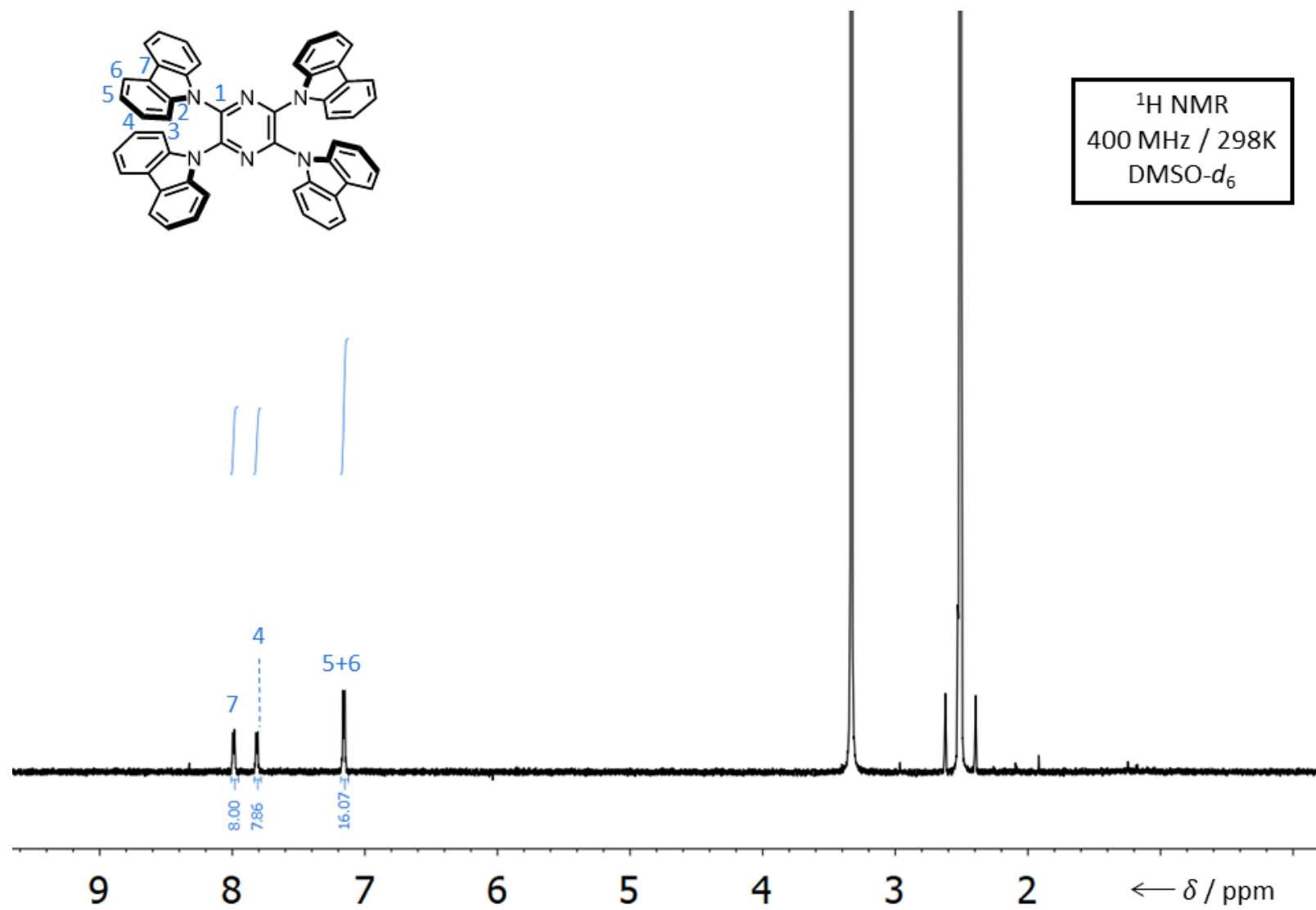


Figure S5 <sup>1</sup>H NMR spectrum of 4CzPz in DMSO-*d*<sub>6</sub>.

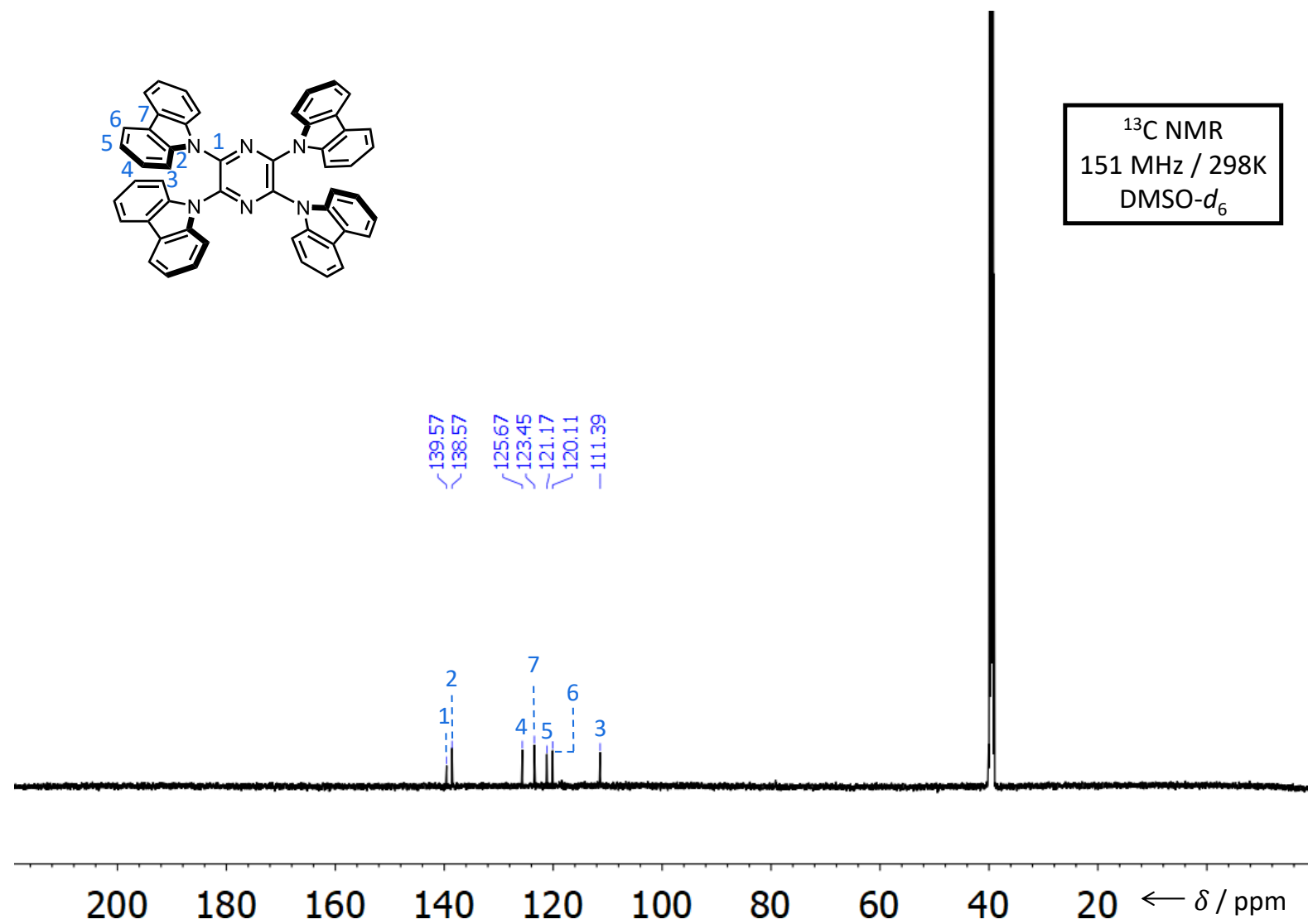


Figure S6 <sup>13</sup>C NMR of 4CzPyz in DMSO-*d*<sub>6</sub>.

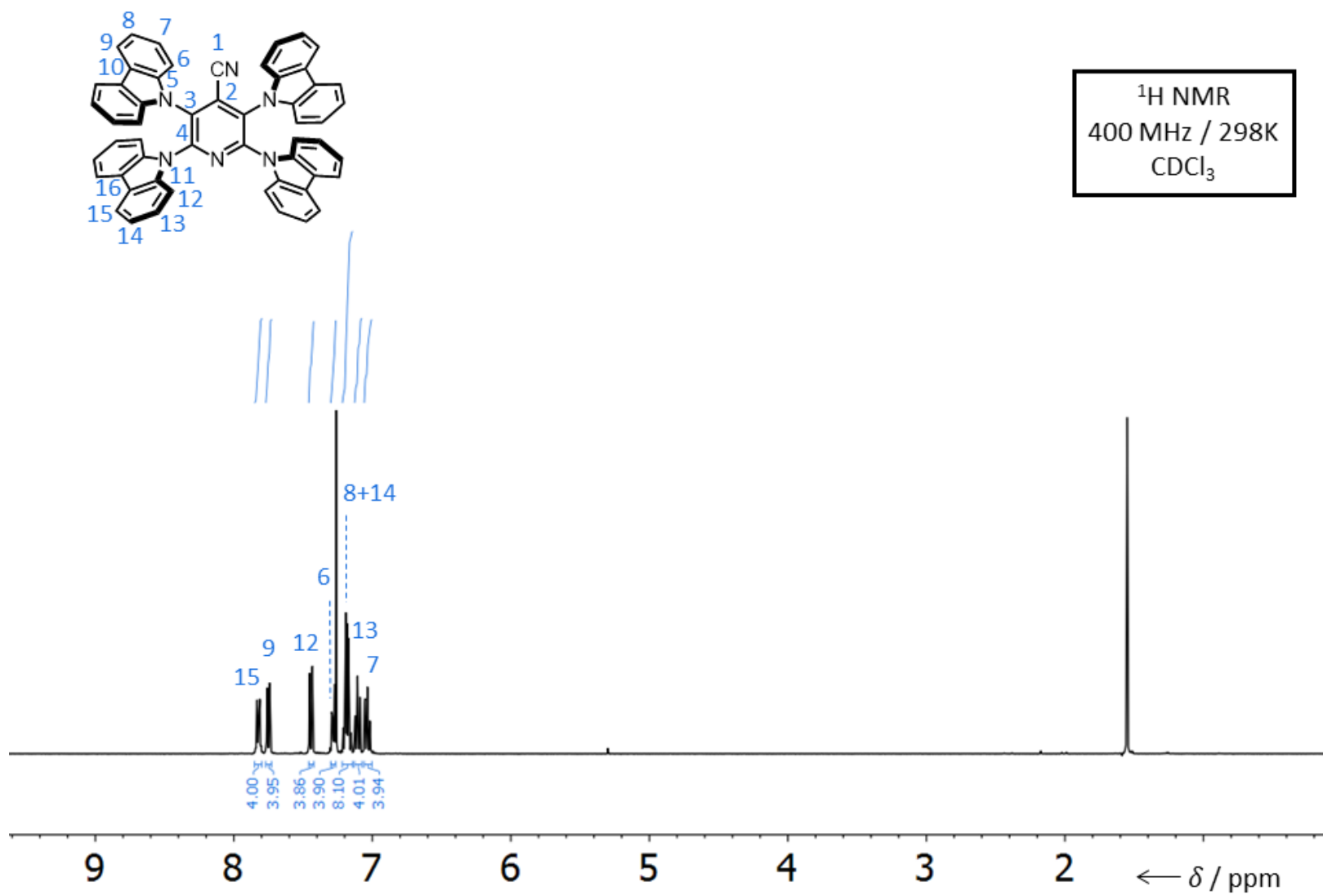


Figure S7 <sup>1</sup>H NMR of 4CzCNPy in CDCl<sub>3</sub>

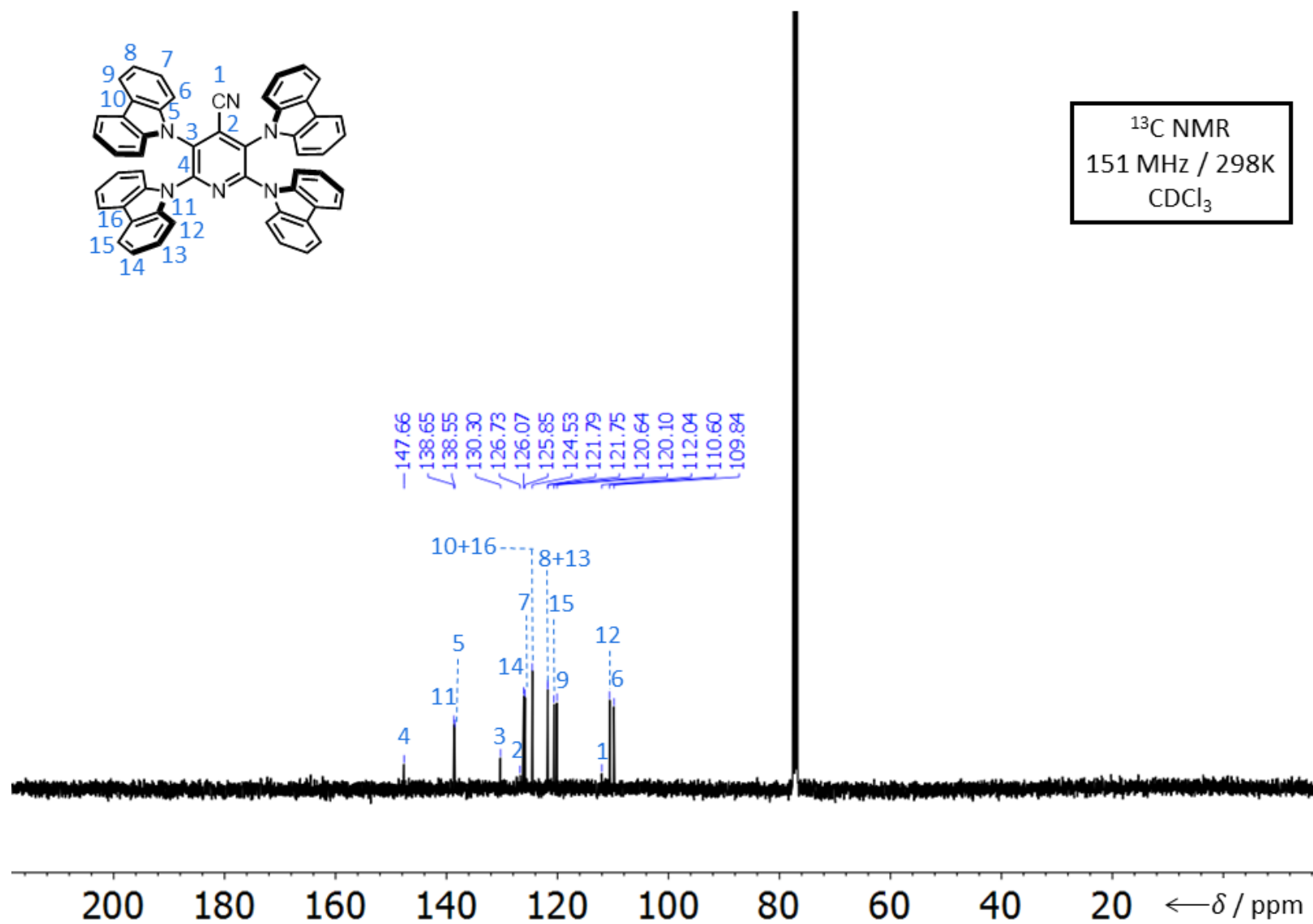
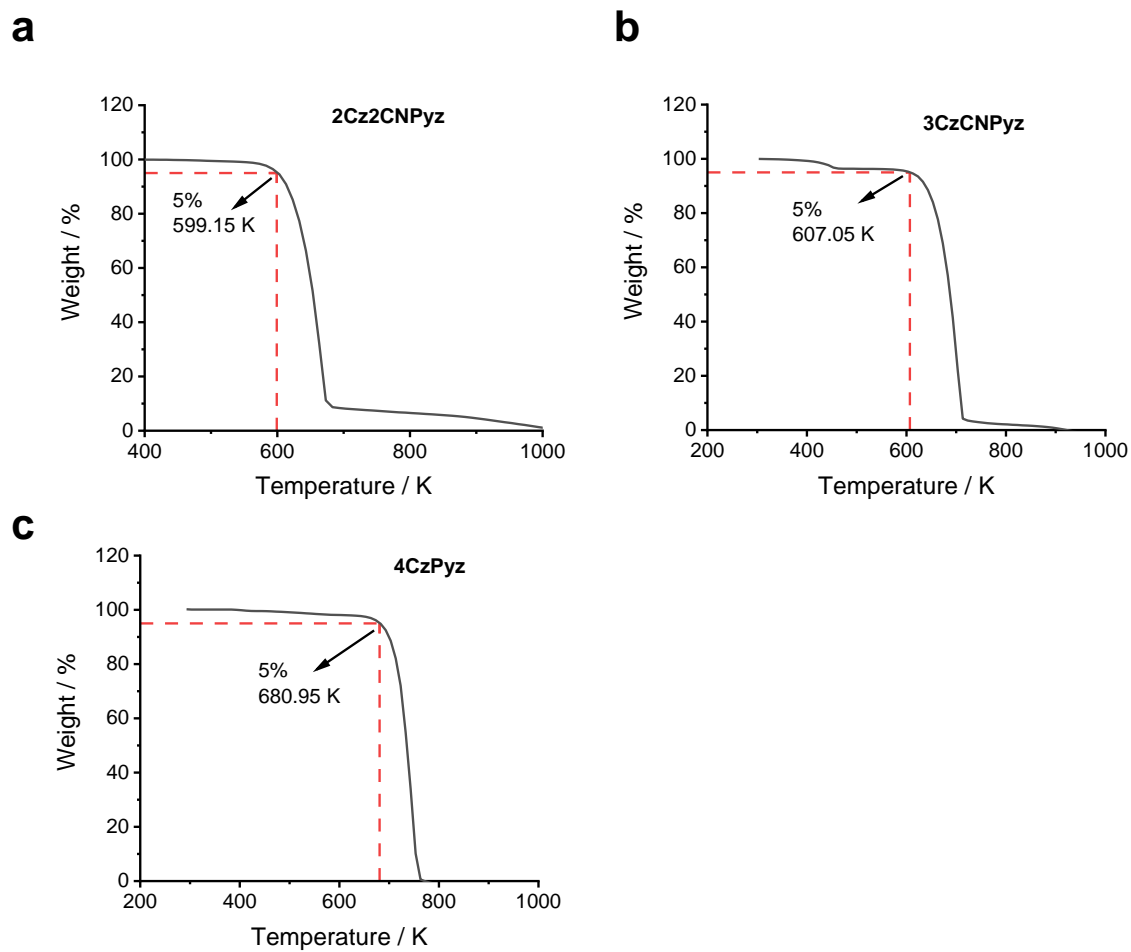


Figure S8 <sup>13</sup>C NMR of **4CzCNPY** in CDCl<sub>3</sub>.

## 4. Thermogravimetric Analysis (TGA)



**Figure S9** Thermogravimetric analysis profiles of (a) **2Cz2CNPyz**, (b) **3CzCNPyz** and (c) **4CzPyz**.

## 5. Cyclic Voltammetry

The electrochemical behavior of all three pyrazine compounds was assessed by cyclic voltammetry (CV) in CH<sub>2</sub>Cl<sub>2</sub> solution versus SCE using ferrocene as the internal standard and NBu<sub>4</sub>PF<sub>6</sub> as the supporting electrolyte (Figure S10). Values of the half wave potential of the first oxidation and reduction processes are listed in Table S1.

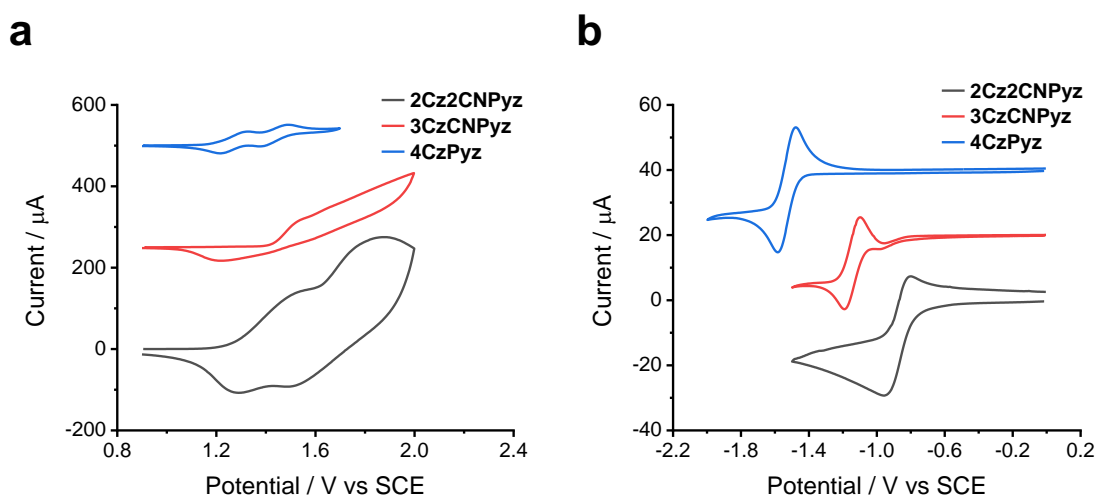


**Figure S10** (a) The cyclic voltammograms of anodic part of **2Cz2CNPyz**, **3CzCNPyz** and **4CzPyz** in CH<sub>2</sub>Cl<sub>2</sub> / 0.1 M NBu<sub>4</sub>PF<sub>6</sub> at SR 50 mVs<sup>-1</sup>. (b) The cyclic voltammograms of the cathodic part of the compounds in CH<sub>2</sub>Cl<sub>2</sub> / 0.1 M NBu<sub>4</sub>PF<sub>6</sub> at SR 50 mVs<sup>-1</sup>.

**Table S1** Electrochemical data of the compounds in CH<sub>2</sub>Cl<sub>2</sub>.

Compound	E <sub>oxd1</sub> /V <sub>SCE</sub>	E <sub>red1</sub> /V <sub>SCE</sub>	HOMO (eV)	LUMO (eV)	E <sub>g</sub>
<b>2Cz2CNPyz</b>	1.28	-0.78	-5.68	3.62	2.06
<b>3CzCNPyz</b>	1.43	-1.07	-5.83	3.33	2.50
<b>4Czpyz</b>	1.19	-1.47	-5.59	2.93	2.66

The HOMO energy levels for these compounds are determined from their onset of the first oxidation potentials located on the carbazole moiety (electron donating unit), while the LUMO energy level is located on the pyrazine ring (electron deficient unit). Within the electrochemical window of CH<sub>2</sub>Cl<sub>2</sub>/NBu<sub>4</sub>PF<sub>6</sub> electrolyte system, **2Cz2CNPyz** and **3CzCNPyz** underwent two quasi-reversible oxidation peaks and one quasi-reversible reduction peak while in case of **4CzPyz** two reversible oxidation and one reversible reduction were obtained. The chemical reversibility was pronounced according to the ratios of peak currents which are close to unity at different scan rates as shown in

Figure S11. All reduction waves could be assigned to the pyrazine ring due to its electron-deficient character.

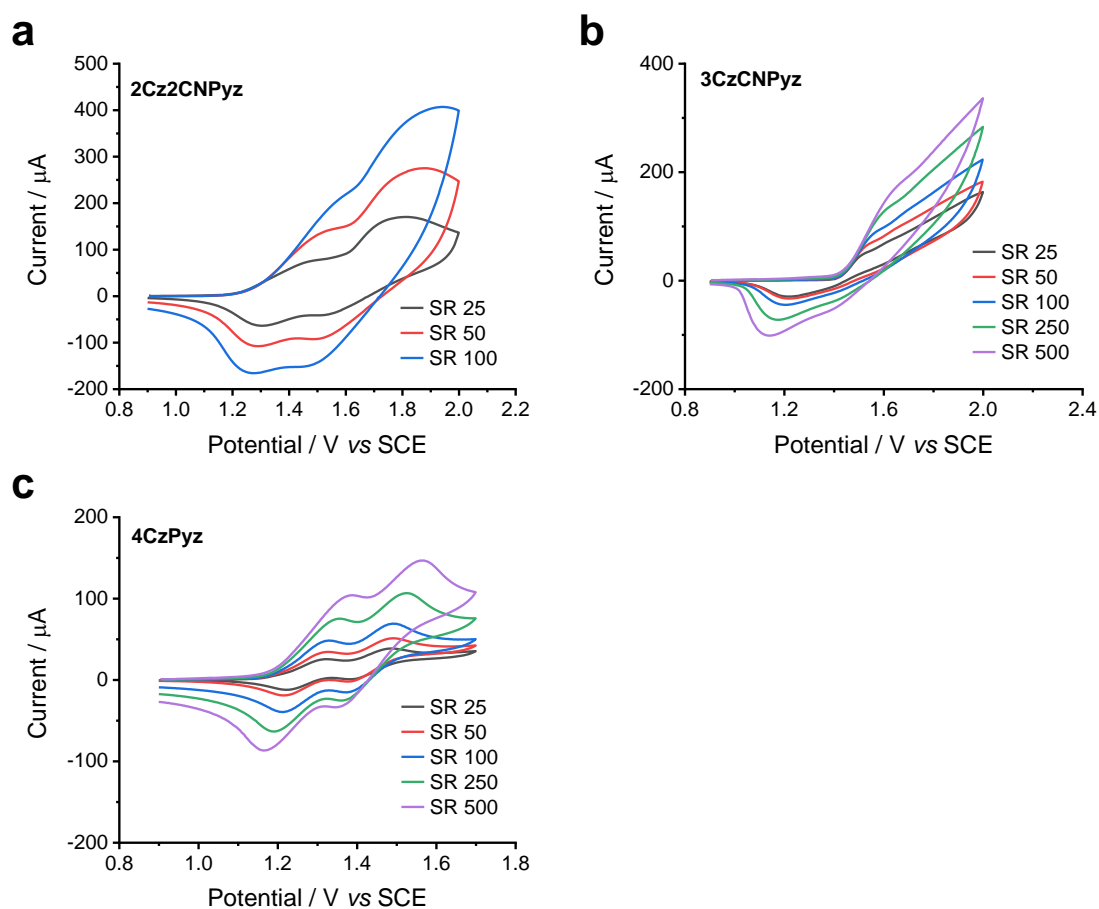


**Figure S11** Cyclic voltammograms of (a) **2Cz2CNPyz**, (b) **3CzCNPyz** and (c) **4CzPyz** at different scan rates. Figure S12 showed that **4CzPyz** maintained its electrochemical stability with cycling. While in case of **2Cz2CNPyz** and **3CzCNPyz** continuous electrochemical polymerization was observed with cycling, confirmed with increasing the peaks intensity maintaining their peaks without decomposition for the charge carrying species. These properties mean these pyrazine derivatives can be used in electrochromic devices (ECDs) applications.

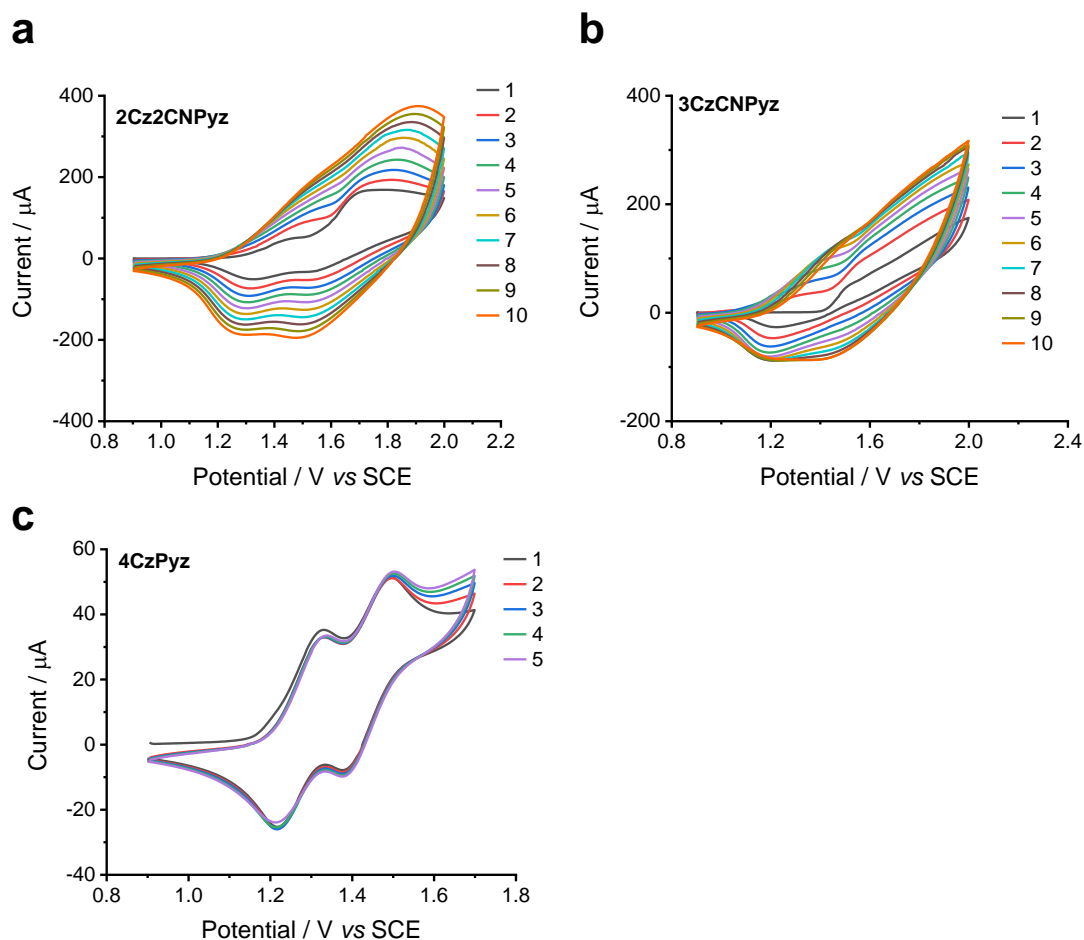


**Figure S12** Cyclic voltammograms of (a) **2Cz2CNPyz**, (b) **3CzCNPyz** and (c) **4CzPyz** for different cycles at scan rate  $25 \text{ mVs}^{-1}$

From Table S1, it can be well illustrated that **4CzPyz** has the lowest onset oxidation potential and hence the lowest HOMO energy level, due to the presence of four electron-donating carbazole units which decreases the electron deficiency of pyrazine ring and subsequently decreases the HOMO energy level. Also **2Cz2CNPyz** has the highest electron deficient character compared with **3CzCNPyz** and **4CzPyz**, which is confirmed by the lowest reduction potential at  $-0.78 \text{ mV}$ .

According to the electrochemical calculations, the investigated pyrazine derivatives have appropriate HOMO and LUMO energy values to be used as good phosphorescent hosts.<sup>6</sup>

## 6. X-ray Crystallography

The various crystallographic data including crystal nature and refinement parameters of all three compounds discussed in this study are summarized in **Table S2** below.

The molecular structures of all three compounds were obtained from single-crystal X-ray diffraction data. These are excellent tools to investigate the structural and packing features of these novel molecules in the solid state. The relative orientation of the carbazole groups and the effect of such orientations on their intermolecular interactions are demonstrated through their crystal structures. Such carbazole orientations with respect to the pyrazine plane are also very important to determine the structural characteristics of their molecular analogues.

Hirshfeld surfaces<sup>7</sup> were employed to provide insights into the intermolecular interactions between crystal molecules in the crystal lattice. We calculated Hirshfeld surfaces of **2Cz2CNPyz** (Figure S15), **3CzCNPyz** (Figure S18), **4CzPyz** (Figure S21), **4CzCNPyz** (Figure S24) and **4CzTPN** (Figure S26) in Crystal Explorer17<sup>8</sup> using an isovalue of 0.5 and mapping the normalized contact distance,  $d_{\text{norm}}$ . The surfaces highlight in red any regions in which the molecular surfaces meet at distances shorter than the sum of the van der Waals radii, while white and blue illustrate regions where they meet at distances that are the sum of the van der Waals radii or longer, respectively. The detailed results and interpretations of each Hirshfeld surfaces are outlined underneath their respective figures.

**Table S2** Summary on the nature of the crystals and various crystallographic parameters of **2Cz2CNPyz**, **3CzCNPyz**, **4CzPyz** and **4CzCNPz**.

Entry	Compound	2Cz2CNPyz	3CzCNPyz	4CzPyz	4CzCNPz
1	Crystal Size/mm <sup>3</sup>	0.20, 0.05, 0.03	0.20, 0.19, 0.03	0.08, 0.25, 0.27	0.16, 0.15, 0.14
2	Empirical formula	C <sub>30</sub> H <sub>16</sub> N <sub>6</sub>	C <sub>41</sub> H <sub>24</sub> N <sub>6</sub>	C <sub>58</sub> H <sub>46</sub> N <sub>8</sub> O <sub>2</sub>	C <sub>54</sub> H <sub>32</sub> N <sub>6</sub>
3	Crystal system	Monoclinic	Triclinic	Triclinic	Triclinic
4	Space group (no.)	P2 <sub>1</sub> /c (#14)	P1 (#1)	P-1 (#2)	P-1
5	T/K	150	150	150	120
6	a/Å	18.0403(12)	13.6993(13)	10.6664(6)	14.0191(10)
7	b/Å	13.8056(9)	16.5231(17)	14.5341(8)	17.6599(14)
8	c/Å	9.0654(7)	22.924(2)	16.6218(9)	17.6613(14)
9	α	90	80.013(7)	73.381(3)	93.434(3)
10	β	91.784(6)	77.096(7)	83.358(3)	97.217(3)
11	γ	90	89.966(6)	71.661(3)	97.245(3)
12	V/ Å <sup>3</sup>	2256.7(3)	4977.3(9)	2342.8(2)	4290.5(6)
13	Z	4	6	2	4
14	μ/ mm <sup>-1</sup>	0.840	0.073	0.618	0.214
15	ρ <sub>calcd</sub> /g cm <sup>-3</sup>	1.355	1.202	1.257	1.332
16	θ <sub>max</sub> /deg	25.99	26.37	66.16	54.99
17	Reflections collected	10063	44377	40984	78470
18	Unique reflections	4330	20199	8008	19689
19	R <sub>int</sub>	0.0395	0.0947	0.0385	0.0660
20	R (I > 2σ)	0.0469	0.0952	0.0682	0.0877
21	R (all data)	0.0998	0.1634	0.0915	0.1340
22	R <sub>w</sub> (all data)	0.1159	0.2704	0.2302	0.2606

**Crystal structure and packing features of 2Cz2CNPyz:** The crystal structure of **2Cz2CNPyz** is depicted in Figure S13. In this molecule the orientation carbazole groups are around 40 to 55 degrees twisted with respect to the plane of dicyanopyrazine moiety (Table S3). The carbazole groups are directed in such a way that the angle between their mutual plane of orientation is about 80 degrees. The pyrazine unit is also deformed slightly from planarity. As a result, the carbonitriles are not in the same plane but twisted to each other about 10 degrees (Figure S14).

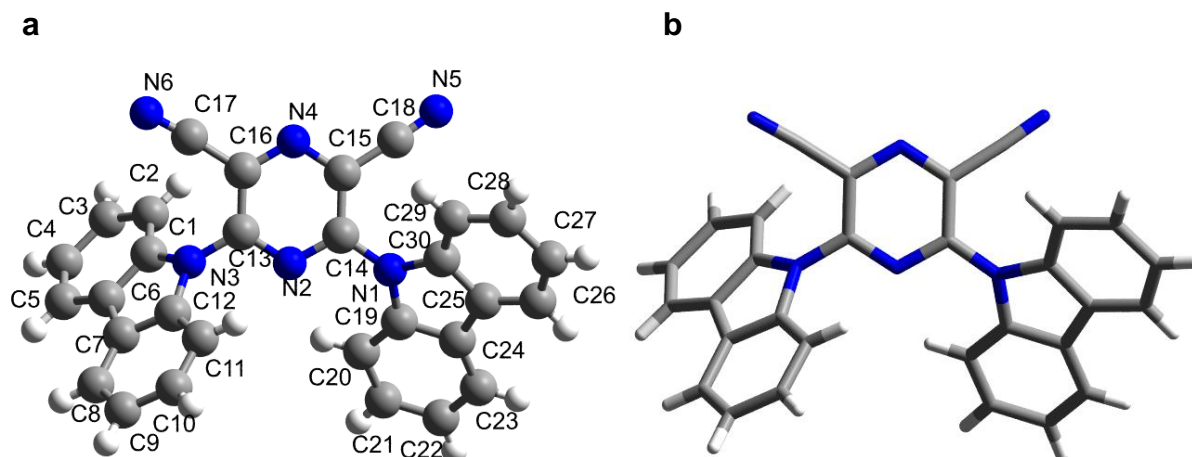


**Figure S13** Crystal structure of **2Cz2CNPyz** (a); Ball and stick representation (Atom Labelled); (b); stick representation. Colour code: blue (nitrogen); grey (carbon) and white (hydrogen).

**Table S3** Torsion angles ( $\varphi$ ) correspond to the carbazole moieties with respect to the pyrazine ring in **2Cz2CNPyz**.

Entry	Constituent atoms	$\varphi / ^\circ$	Entry	Constituent atoms	$\varphi / ^\circ$
1	N2 C13 N3 C12	41.62	5	N2 C13 N3 C1	-125.47
2	C16 C13 N3 C12	-136.32	6	C16 C13 N3 C1	56.60
3	C15 C14 N1 C30	39.83	7	C15 C14 N1 C19	-133.58
4	N2 C14 N1 C30	-145.10	8	N2 C14 N1 C19	41.49

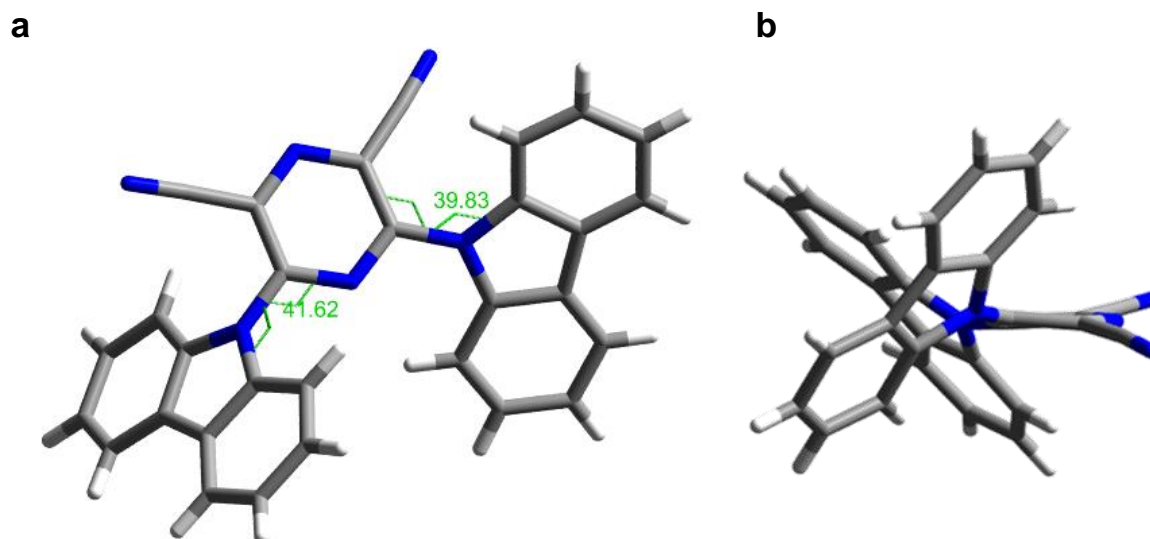


**Figure S14** Structure of **2Cz2CNPyz** shows (a) orientations of carbazole moieties with respect to the pyrazine ring and (b) deformed pyrazine ring from planarity. Colour code: blue (nitrogen); grey (carbon) and black (hydrogen).

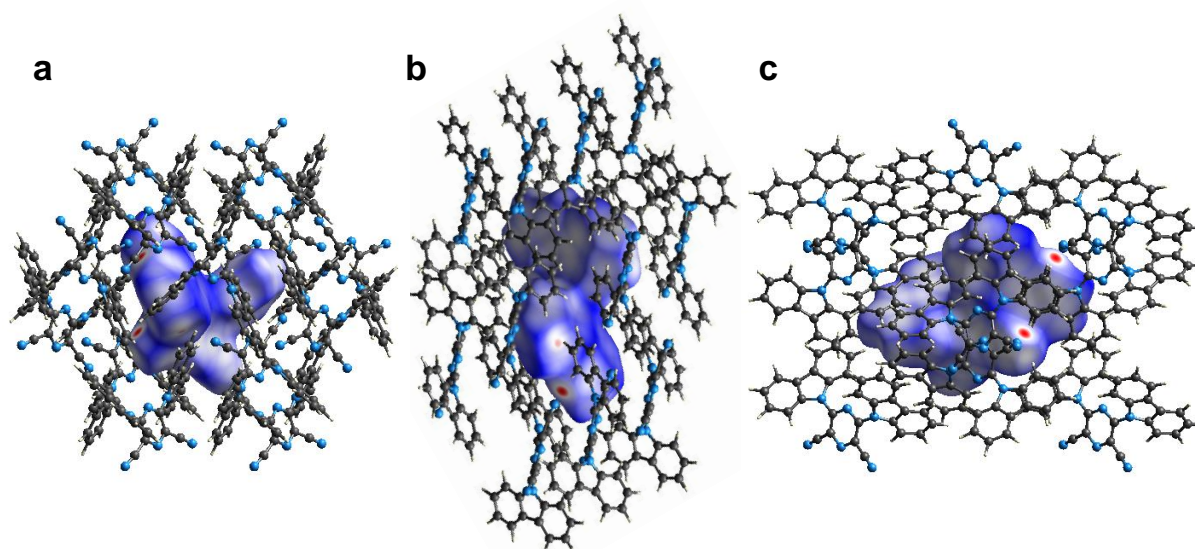


**Figure S15** Hirshfeld surface and packing pattern of **2Cz2CNPyz** (a) in a- direction; (b) in b-direction and (c) in c- direction.

Overall, the Hirshfeld surface of **2Cz2CNPyz** (Figures S15) reveals the highest number of close contacts that are slightly shorter than the sum of van der Waals radii in our reported series of compounds. This is demonstrated by the number of red patches which are bright in colour and moderately sized. This data suggests multiple strong intermolecular N...H hydrogen bonding occurring from the peripheral CN groups and neighbouring carbazole units in the solid state. We can, therefore, assume that their contributions will influence crystal packing.

**Crystal structure and packing features of 3CzCNPyz:** The molecular structure of **3CzCNPyz** is depicted in Figure S16. The asymmetric unit of this crystal contains as much as six **3CzCNPyz** molecules in the crystal network. Sometimes, molecules pack awkwardly with each other in the solid state and for energy minimization crystals containing multiple independent molecules in the asymmetric unit ( $Z' > 1$ ) are formed. As mentioned above even if they not related to each other by crystallographic symmetry, these six structures are the same chemical species and hence the structural features of **3CzCNPyz** could be explained by taking any one of these molecules as a representative example. As in the case of its dicarbazole-dicarbonitrile analogues, the carbazole moieties in this molecule are also oriented randomly in three dimensions with respect to the pyrazine fraction having torsion angles ranging from 35 to 55 degrees (Table S4). The mutual orientation of the two adjacent carbazole groups is found to be more or less 60 degree and the third carbazole is directed almost right angles from them. In this molecule also the pyrazine unit is deformed from planarity as evident from Figure S17.

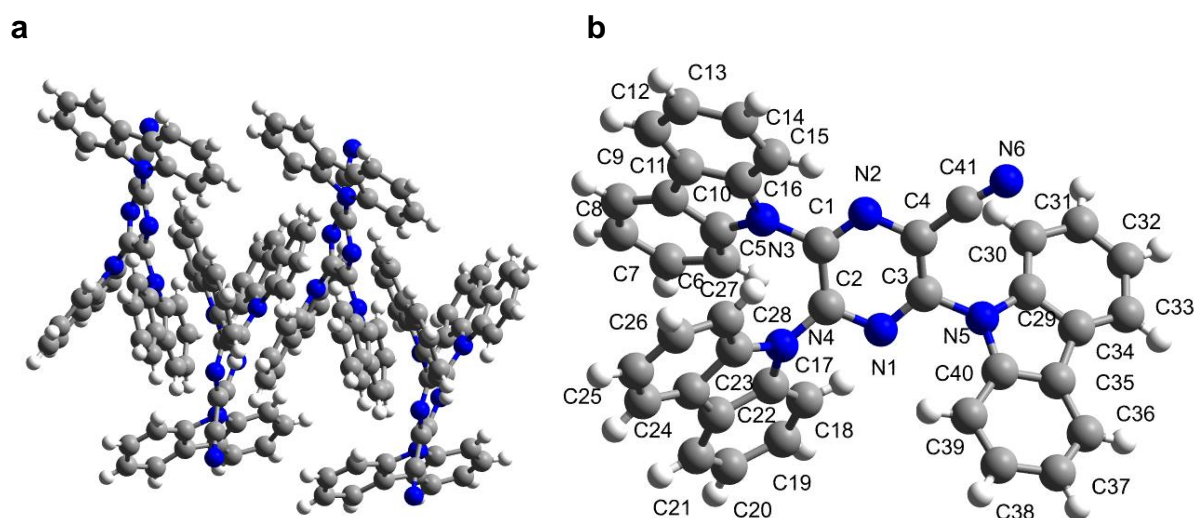


**Figure S16** Crystal structure of **3CzCNPyz** (a); Ball and stick representation showing the asymmetric unit; (b) Ball and stick representation. Colour code: blue (nitrogen); grey (carbon) and white (hydrogen)

**Table S4** Torsion angles ( $\varphi$ ) correspond to the carbazole moieties with respect to the pyrazine ring in **3CzCNPyz**.

Entry	Constituent atoms				$\varphi / ^\circ$	Entry	Constituent atoms				$\varphi / ^\circ$
1	C1	C2	N4	C17	134.62	7	C1	C2	N4	C28	-36.70
2	N1	C2	N4	C17	-53.52	8	N1	C2	N4	C28	135.16
3	C2	C1	N3	C5	-36.06	9	C2	C1	N3	C16	139.00
4	N2	C1	N3	C5	141.86	10	N2	C1	N3	C16	-43.08
5	C4	C3	N5	C29	-52.17	11	C4	C3	N5	C40	129.85
6	N1	C3	N5	C29	132.82	12	N1	C3	N5	C40	-45.16

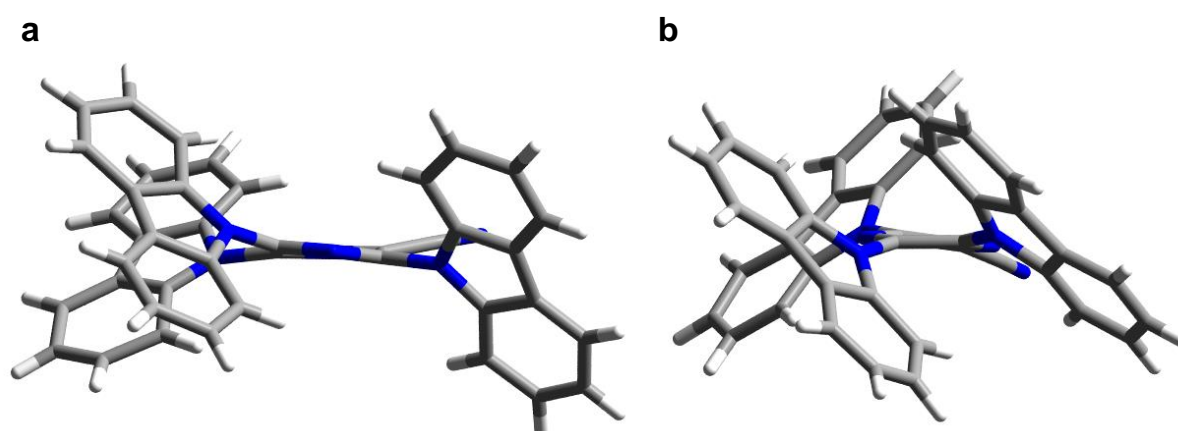


**Figure S17** Structure of **3CzCNPyz** shows (a) orientations of carbazole moieties with respect to the pyrazine ring and (b) deformed pyrazine ring from planarity. Colour code: blue (nitrogen); grey (carbon) and black (hydrogen).

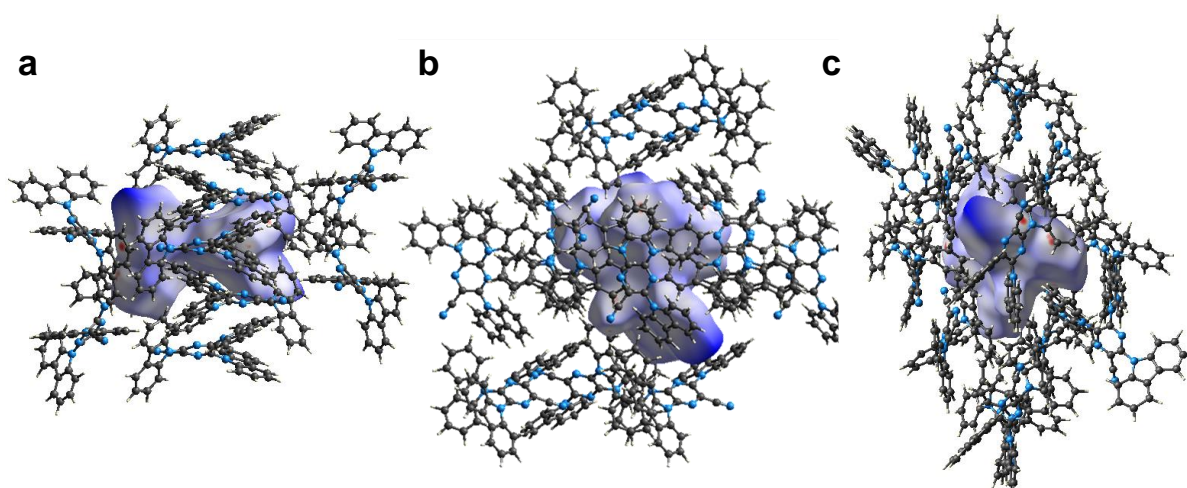


**Figure S18.** Hirshfeld surface and packing pattern of **3CzCNPyz** (a) in a- direction; (b) in b- direction and (c) in c- direction.

Overall, the Hirshfeld surface of **3CzCNPyz** (Figure S18) reveals there are only a few contacts that are slightly shorter than the sum of van der Waals radii, demonstrated by the small number red patches. The small red spot that can be seen arises from intermolecular N...H hydrogen bonding between neighbouring carbazole units in some instances.

**Crystal structure and packing features of 4CzPyz:** The asymmetric unit of this crystal contains only half fragment of **4CzPyz** and the whole molecule can be generated by appropriate symmetry expansion. At the same time the asymmetric unit has two such half compound intermediates fragments along with two molecules of DMF which are also co-crystallized along with **4CzPyz** as the interstitial solvent. The molecular structure of **4CzPyz**, after symmetry expansion and hiding the second **4CzPyz** as well as the solvent molecules is depicted in Figure S19b. In this molecule the orientation carbazole groups are around 45- 65 degrees twisted with respect to the plane of pyrazine moiety and the mutual orientation of carbazole groups in the molecule is more or less 90 degree (Table S5). Unlike **2Cz2CNPyz**, the pyrazine unit of **4CzPyz** is planar and the carbazole molecules are oriented along its sides as widely as possible in order to minimize steric constraints (Figure S20a).

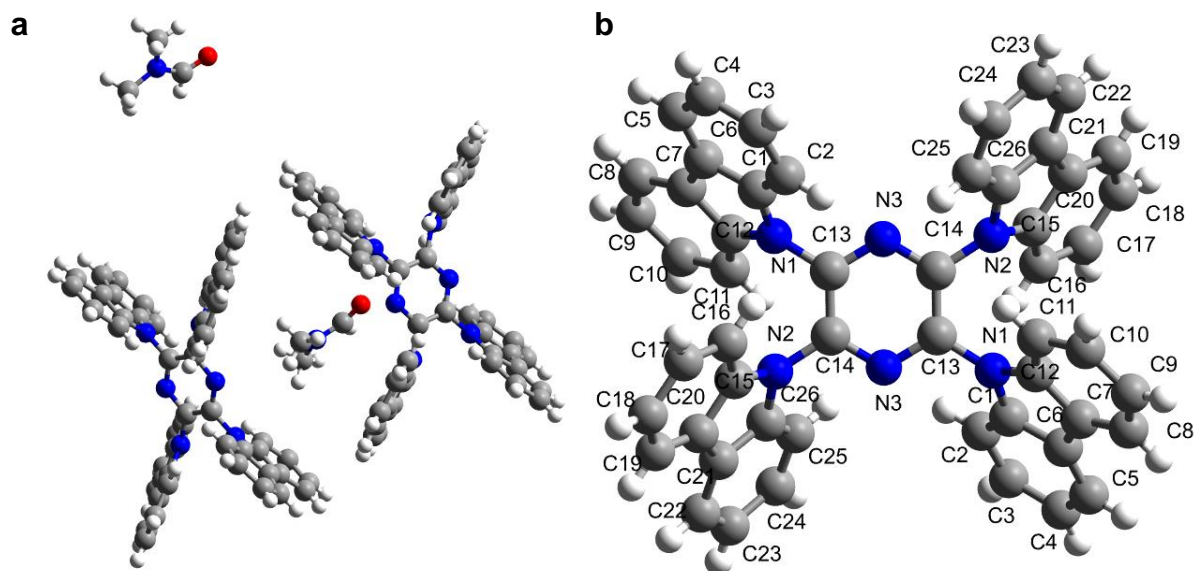


**Figure S19.** Crystal structure of **4CzPyz** (a); Ball and stick representation showing the asymmetric unit; (b); ball and stick representation of one molecule. Colour code: blue (nitrogen); grey (carbon); white (hydrogen) and red (oxygen).

**Table S5** Torsion angles ( $\varphi$ ) correspond to the carbazole moieties with respect to the pyrazine ring in compound **4CzPyz**.

Entry	Constituent atoms	$\varphi / ^\circ$	Entry	Constituent atoms	$\varphi / ^\circ$
1	N3 C13 N1 C1	-49.35	9	N3 C13 N1 C12	119.16
2	C14 C13 N1 C1	132.39	10	C14 C13 N1 C12	-59.10
3	C13 C14 N2 C15	-67.94	11	C13 C14 N2 C26	138.55
4	N3 C14 N2 C15	108.77	12	N3 C14 N2 C26	-44.74
5	C40 C39 N5 C27	127.10	13	C40 C39 N5 C38	-59.82
6	N6 C39 N5 C27	-55.58	14	N6 C39 N5 C38	117.50
7	N6 C40 N4 C41	-47.95	15	N6 C40 N4 C52	114.22
8	C39 C40 N4 C41	134.45	16	C39 C40 N4 C52	-63.38

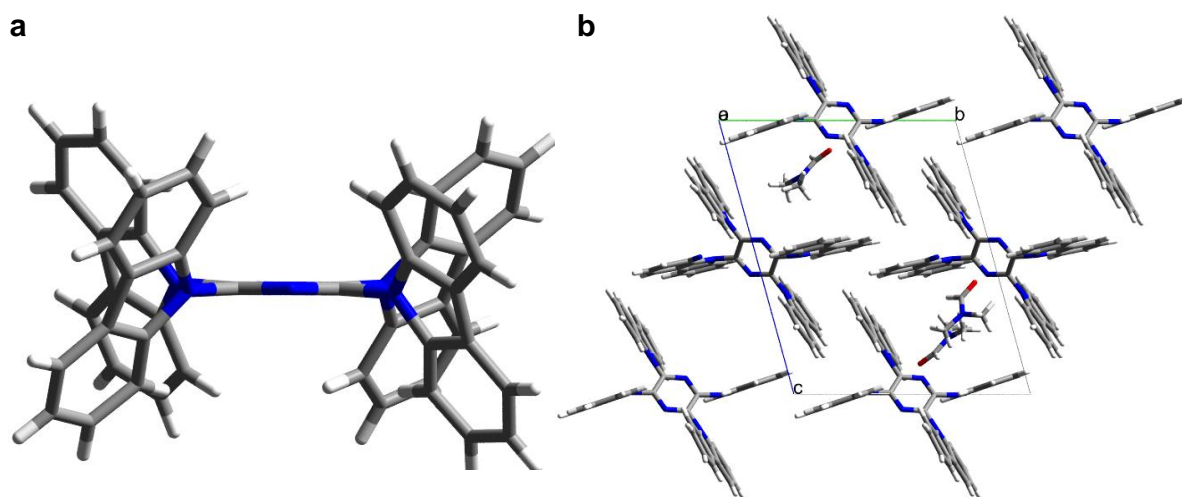


**Figure S20** (a) Structure of **4CzPyz** showing the planar pyrazine central ring and (b) Crystal packing of **4CzPyz**, demonstrating that the carbazole moieties are interlocked efficiently in the crystal network. Colour code: blue (nitrogen); grey (carbon); white (hydrogen) and red (oxygen).

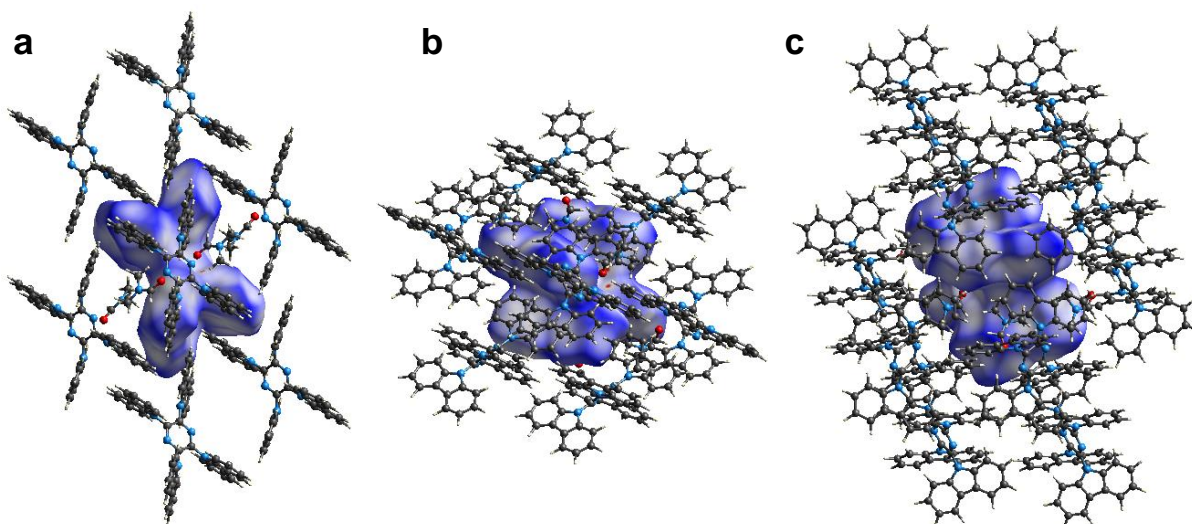


**Figure S21** Hirshfeld surface and packing pattern of **4CzPyz** (a) in a- direction; (b) in b- direction and (c) in c- direction.

Overall, the Hirshfeld surface of **4CzPyz** (Figure S21) reveals the lowest number of close contacts throughout the series of compounds we report, demonstrated by the lack of red patches arising from intermolecular interaction. The small red spot that can be seen arises from interactions with the crystallised solvent.

### Crystal structure and packing features of 4CzCNPy:

The asymmetric unit of this crystal contains two molecules. The asymmetric unit also contains dichloromethane molecules as interstitial solvents whose overall contribution is 2.25 molecules per asymmetric unit (Figure S22a). Unlike, the other three carbazole derivatives discussed in this **4CzCNPy** section, the **4CzCNPy** molecule has a (4- cyano)pyridine ring with at the core instead of the central pyrazine moiety. This pyridine unit is found to be planar in the crystal structure (Figure S22b) and the carbazole units are oriented randomly at both sides of it, twisted around 50- 80 degree ranges with respect to the pyridine plane (Table S6). An interesting feature of this molecule is that the adjacent carbazole moieties in each **4CzCNPy** are oriented face to face to engage intramolecular  $\pi\cdots\pi$  interaction as depicted in Figure S23a. The face to face distance between the adjacent carbazoles are found to be around 4Å which is sufficient to cause appreciable  $\pi\cdots\pi$  interactions. At the same time no intermolecular  $\pi\cdots\pi$  interactions are possible in the crystals as there are no interlocking of carbazole moieties among neighbouring **4CzCNPy** molecules (Figure S23b).

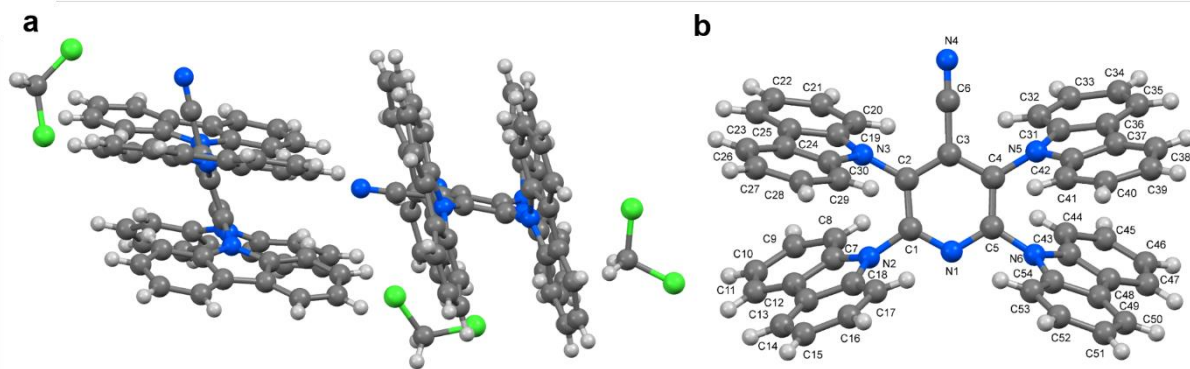


**Figure S22.** Crystal structure of **4CzCNPy** (a); Ball and stick representation showing the asymmetric unit; (b); ball and stick representation of one molecule. Colour code: blue (nitrogen); grey (carbon); white (hydrogen) and green (chlorine). **N.B.** Solvent disorder has been removed from these plots for clarity but the full system can be observed in the CIF file.

**Table S6** Torsion angles ( $\varphi$ ) correspond to the carbazole moieties with respect to the pyrazine ring in compound **4CzCNP**y.

Entry	Constituent atoms				$\varphi / ^\circ$	Entry	Constituent atoms				$\varphi / ^\circ$
1	C3	C2	N3	C19	78.56	9	C3	C2	N3	C30	-124.89
2	C1	C2	N3	C19	-105.85	10	C1	C2	N3	C30	50.70
3	N1	C1	N2	C7	-123.33	11	N1	C1	N2	C18	65.90
4	C2	C1	N2	C7	57.43	12	C2	C1	N2	C18	-113.34
5	C3	C4	N5	C31	-78.01	13	C3	C4	N5	C42	128.11
6	C5	C4	N5	C31	106.84	14	C5	C4	N5	C42	-47.03
7	C4	C5	N6	C43	-55.33	15	C4	C5	N6	C54	115.42
8	N1	C5	N6	C43	123.99	16	N1	C5	N6	C54	-65.27

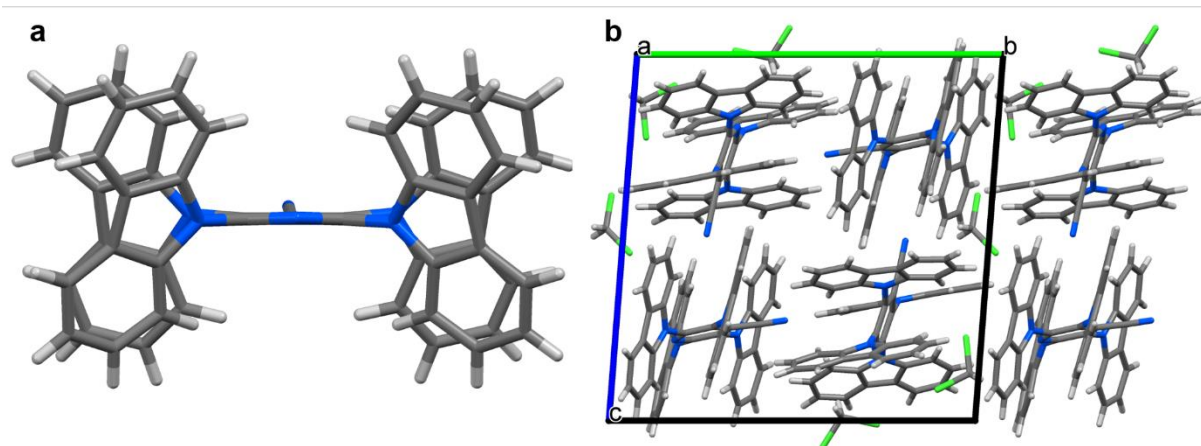


**Figure S23** (a) Structure of **4CzCNP**y shows its planar pyrazine ring and intramolecular  $\pi \cdots \pi$  interactions between opposite carbazole units (b) Crystal packing of **4CzCNP**y, demonstrating no interlocking and that the packing is independent of intermolecular interactions. Colour code: blue (nitrogen); grey (carbon); white (hydrogen) and red (oxygen). **N.B.** Solvent disorder has been removed from these plots for clarity but the full system can be observed in the CIF file.

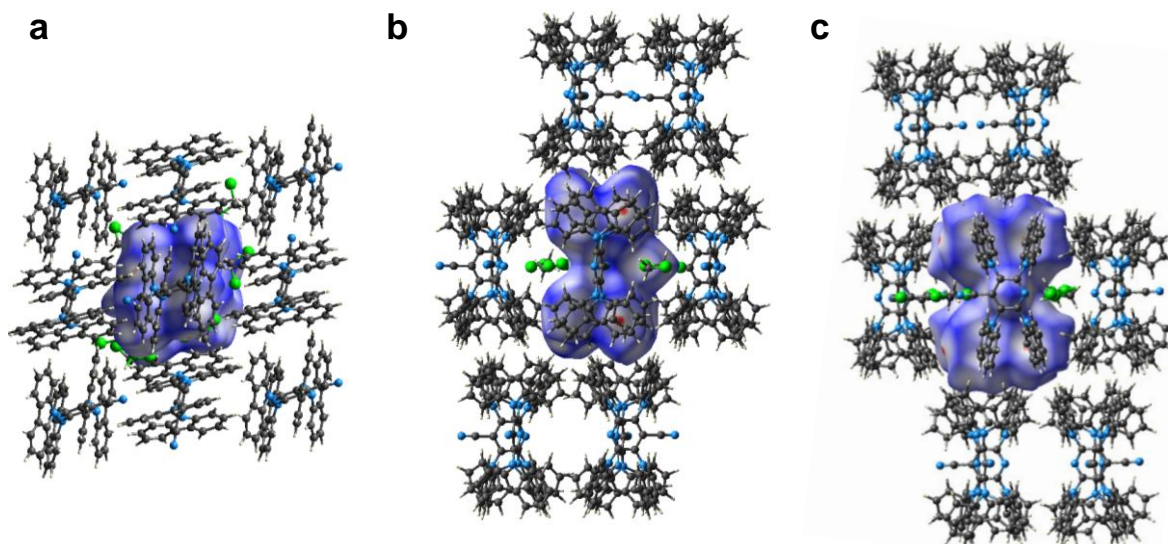


**Figure S24** Hirshfeld surface and packing pattern of **4CzCNPy** (a) in a- direction; (b) in b- direction and (c) in c- direction.

Overall, the Hirshfeld surface of **4CzCNPy** (Figure S24) reveals a moderate number of close contacts that are slightly shorter than the sum of van der Waals radii, demonstrated by the small number red patches. The small red spot that can be seen arises from intermolecular CH $\cdots$  $\pi$  interactions with neighbouring molecules in the solid state.

**Crystal structure and packing features of 4CzTPN:** General descriptions of the **4CzTPN** crystal packing and structure (Figure S25) can be found in the work by Etherington *et al.*<sup>3</sup>

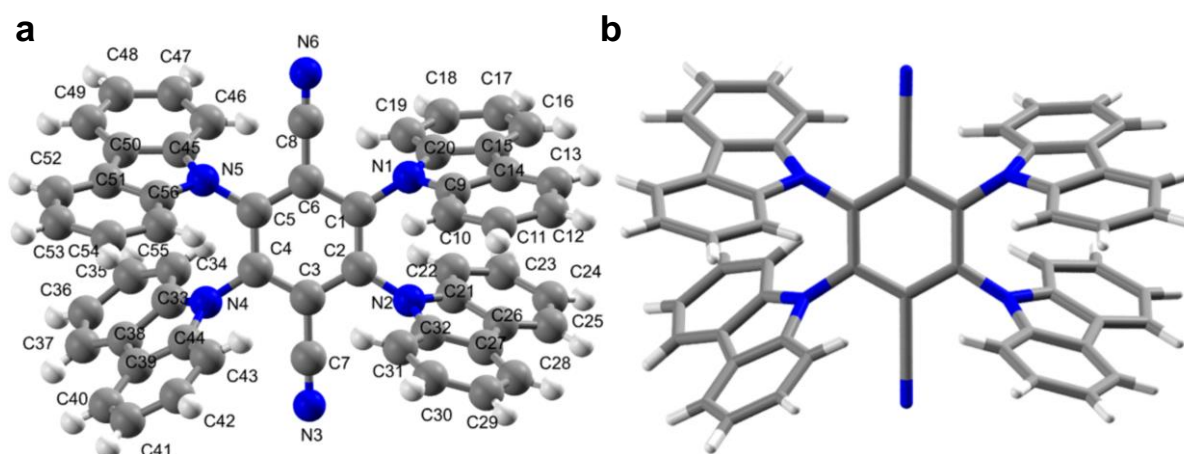


**Figure S25** Crystal structure of **4CzTPN** (a); Ball and stick representation (Atom Labelled); (b); stick representation. Colour code: blue (nitrogen); grey (carbon) and white (hydrogen).

**Table S7** Torsion angles ( $\varphi$ ) correspond to the carbazole moieties with respect to the pyrazine ring in compound **4CzTPN**.

Entry	Constituent atoms	$\varphi / ^\circ$	Entry	Constituent atoms	$\varphi / ^\circ$
1	C6 C5 N5 C45	77.21	9	C6 C5 N5 C56	-135.08
2	C4 C5 N5 C45	-105.01	10	C4 C5 N5 C56	42.69
3	C5 C4 N4 C33	63.63	11	C5 C4 N4 C44	-117.48
4	C3 C4 N4 C33	-113.84	12	C3 C4 N4 C44	65.05
5	C6 C1 N1 C20	-82.77	13	C6 C1 N1 C9	132.32
6	C2 C1 N1 C20	98.62	14	C2 C1 N1 C9	-46.30
7	C1 C2 N2 C21	-56.96	15	C1 C2 N2 C32	107.80
8	C3 C2 N2 C21	121.67	16	C3 C2 N2 C32	-73.58

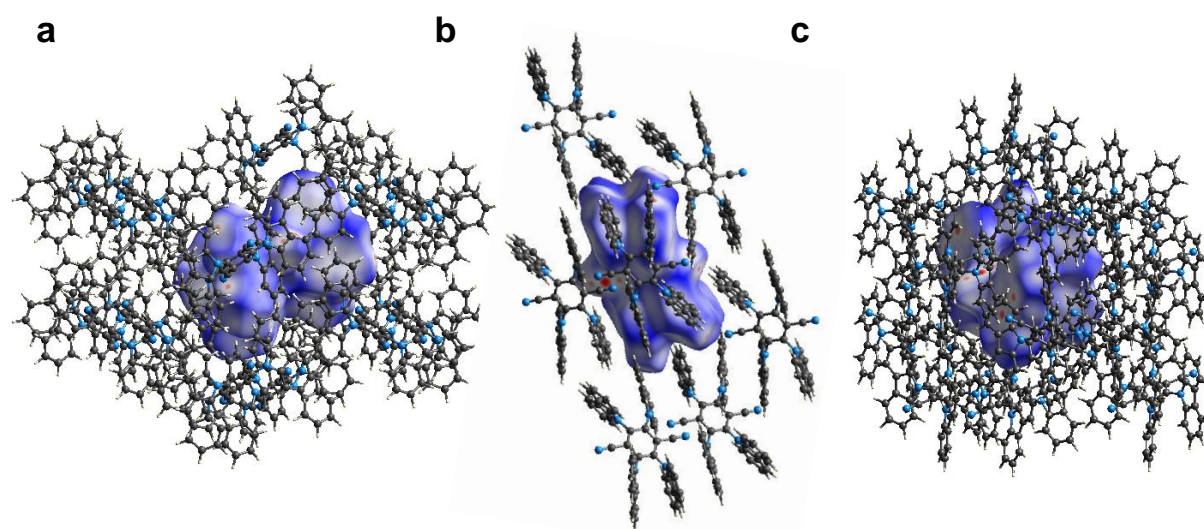


**Figure S26** Hirshfeld surface and packing pattern of **4CzTPN** (a) in a- direction; (b) in b- direction and (c) in c- direction.

Overall, the Hirshfeld surface of **4CzTPN** (Figure S25) reveals there are only a few contacts that are slightly shorter than the sum of van der Waals radii, demonstrated by the small number red patches. The red spots that can be seen arise from both the presence of intermolecular  $\text{CH}\cdots\pi$  and  $\pi\cdots\pi$  interactions with neighbouring molecules in the solid state.

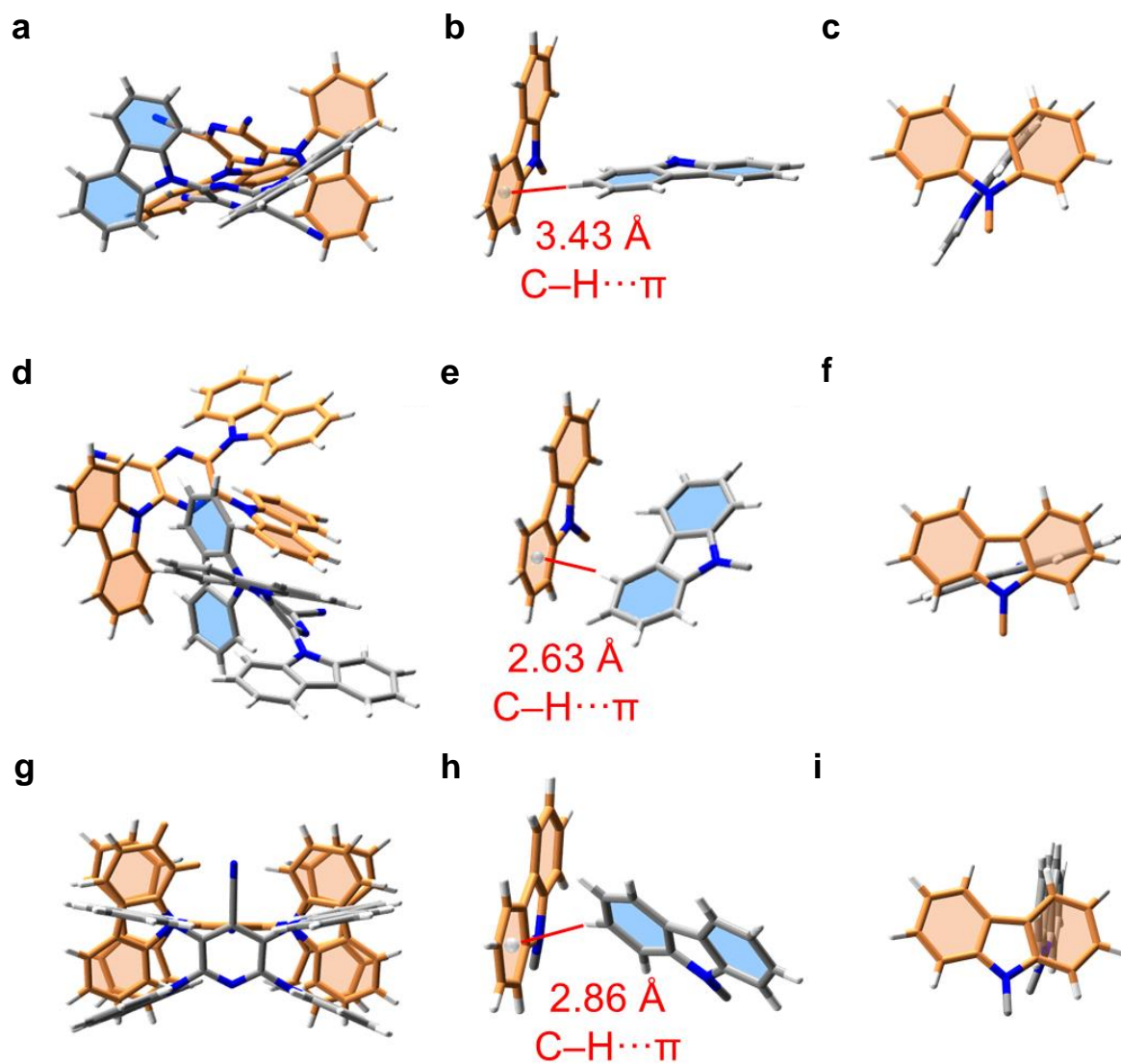


**Figure S27** The crystal structures of **2Cz2CNPyz**, **3CzCNPyz** and **4CzCNPz**. (a) **2Cz2CNPyz** packing behaviour, (b) the shortest distance between interacting molecules and (c) the overlap between the carbazoles. (d) **3CzCNPyz** packing behaviour, (e) the shortest distance between interacting molecules and (f) the overlap between the carbazoles. (g) **4CzCNPz** packing behaviour, (h) the shortest distance between interacting molecules and (i) the overlap between the carbazoles.

## 7. Steady-state Photophysical Characterization

The steady-state absorption and photoluminescence spectra of the compounds were measured in solution as a function of solvent polarity.

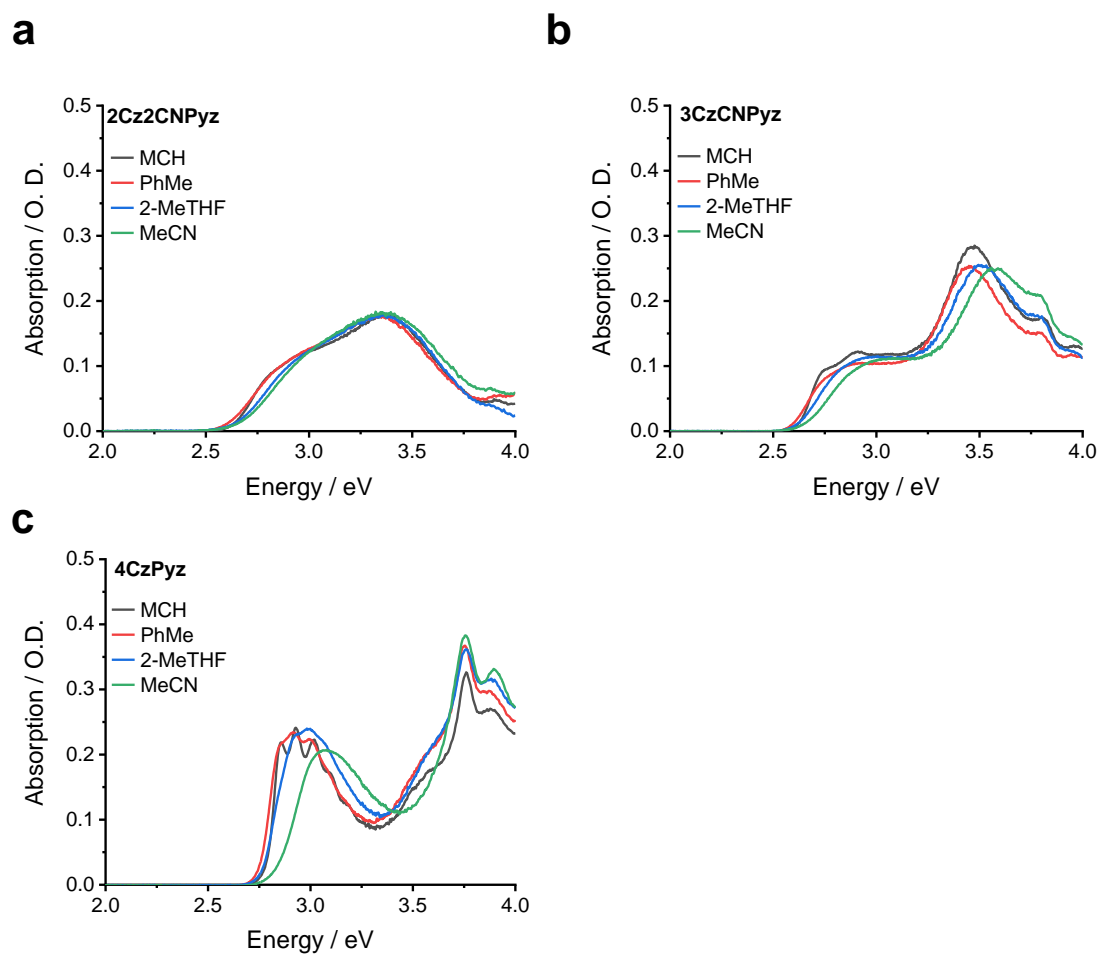


**Figure S28** Absorption spectra measured at 10  $\mu$ M concentration as a function of solvent polarity for (a) **2Cz2CNPyz** (b) **3CzCNPyz** and (c) **4CzPyz**.

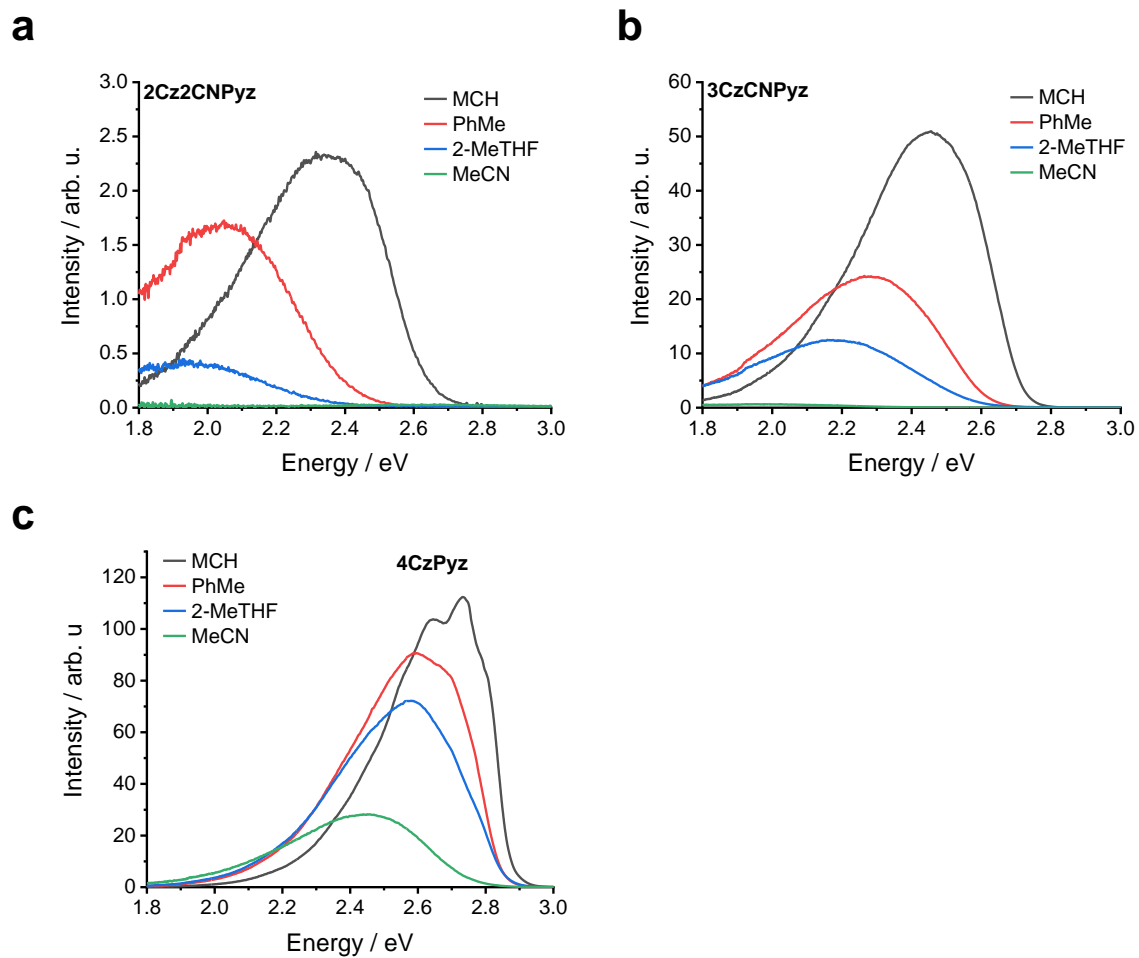


**Figure S29** Photoluminescence spectra measured at 10  $\mu\text{M}$  concentration as a function of solvent polarity for (a) **2Cz2CNPyz**, (b) **3CzCNPyz** and (c) **4CzPyz**.

### CIE 1931

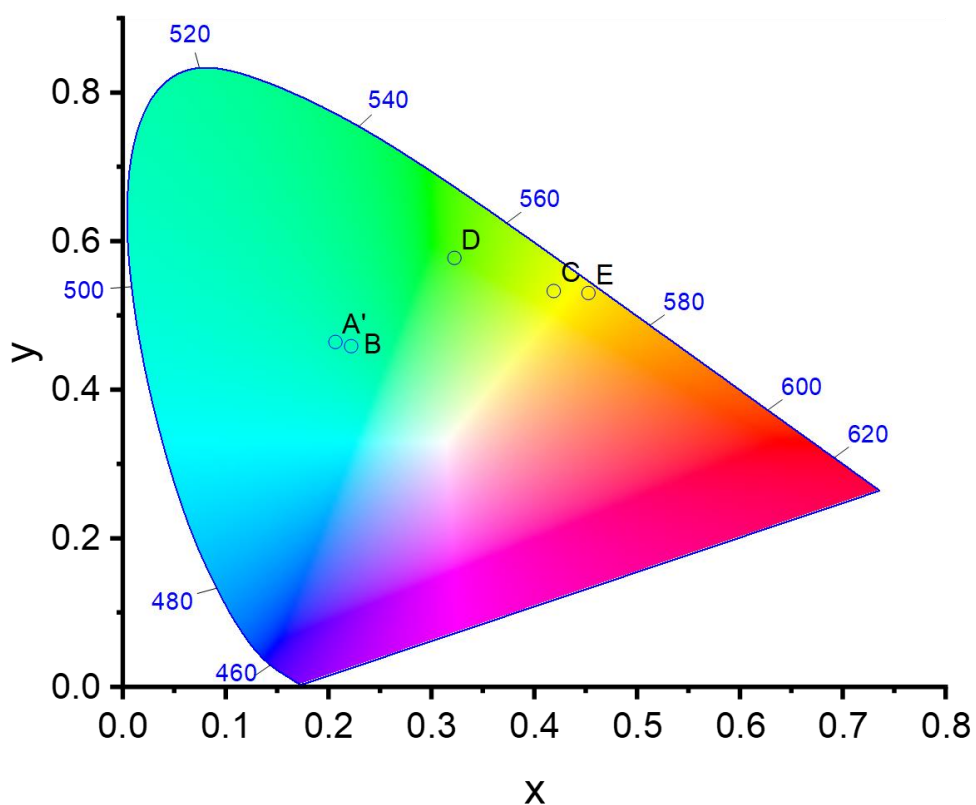
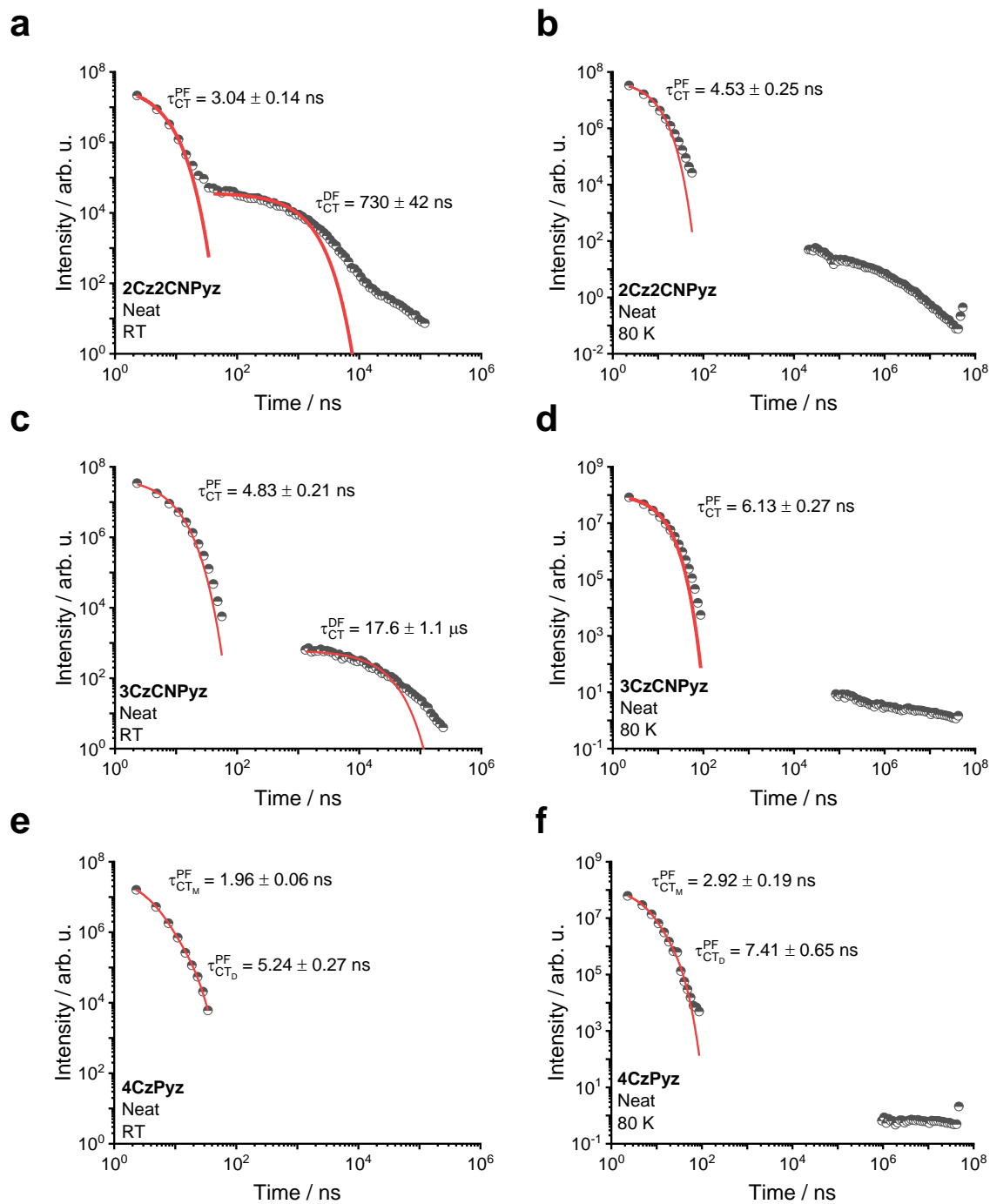


**Figure S30** CIE 1931 curve for the photoluminescence of **4CzIPN** in a series of films. A'=0.3 wt% zeonex, B = 1 wt% zeonex, C = 10 wt% zeonex, D = 10 wt% DPEPO and E = neat film. Photoluminescence spectra used to calculate the CIE curves was obtained from the raw data of films used in Etherington *et al.*<sup>3</sup>

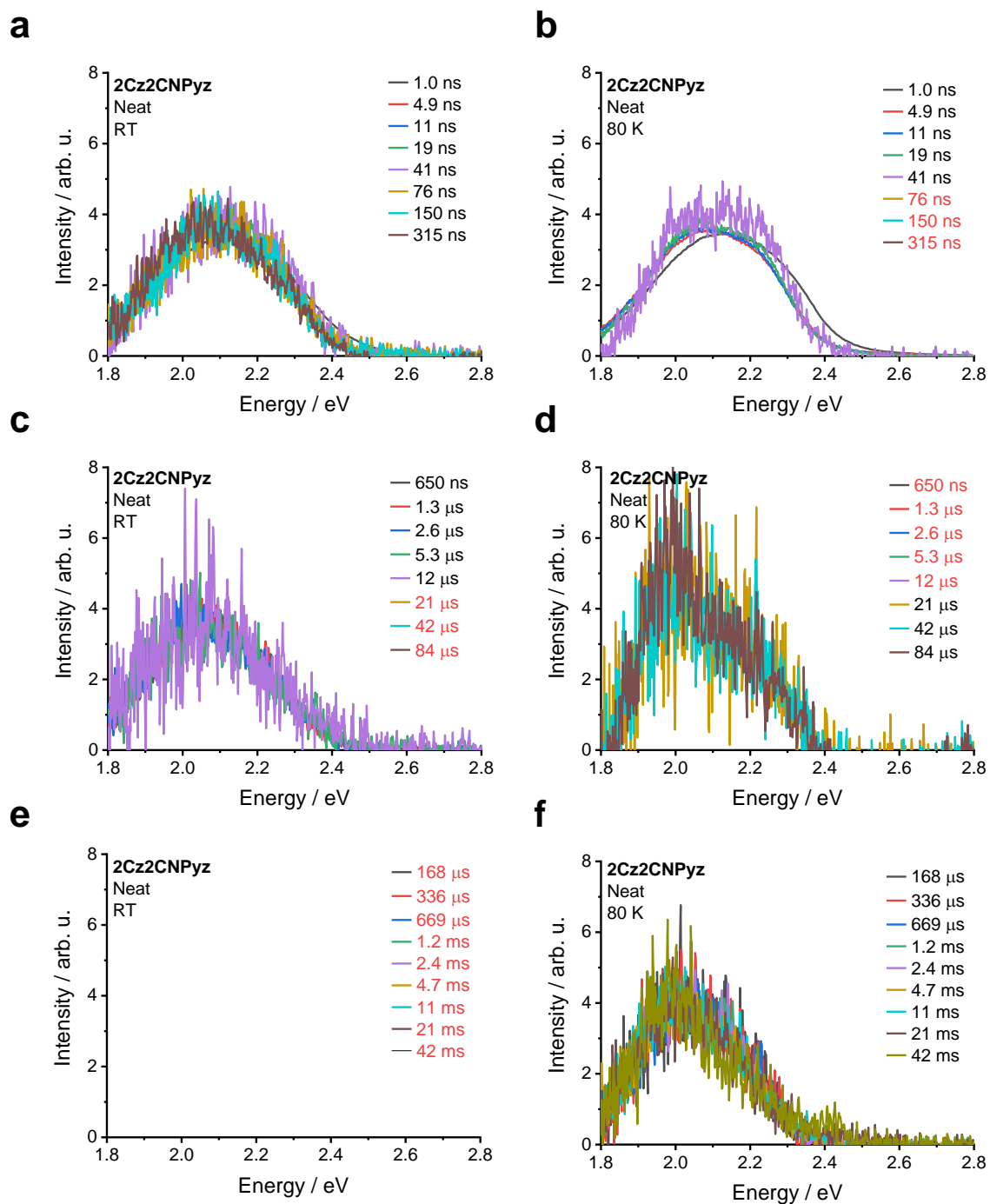
**Table S8** Onset energies of the steady state fluorescence of the compounds. Energies are in eV.

Environment	4CzTPN	4CzCNPY	4CzPyz
MCH (Hexane)	2.65 <sup>3</sup>	(2.7) <sup>9</sup>	2.9
MeCN (DMF)	2.5 <sup>3</sup>	(2.63) <sup>9</sup>	2.8
Neat Film	2.3 <sup>3</sup>	2.5 <sup>9-11</sup>	2.8
$E_{\text{MeCN(DMF)}} - E_{\text{Neat}}$	0.2	(0.13)	0

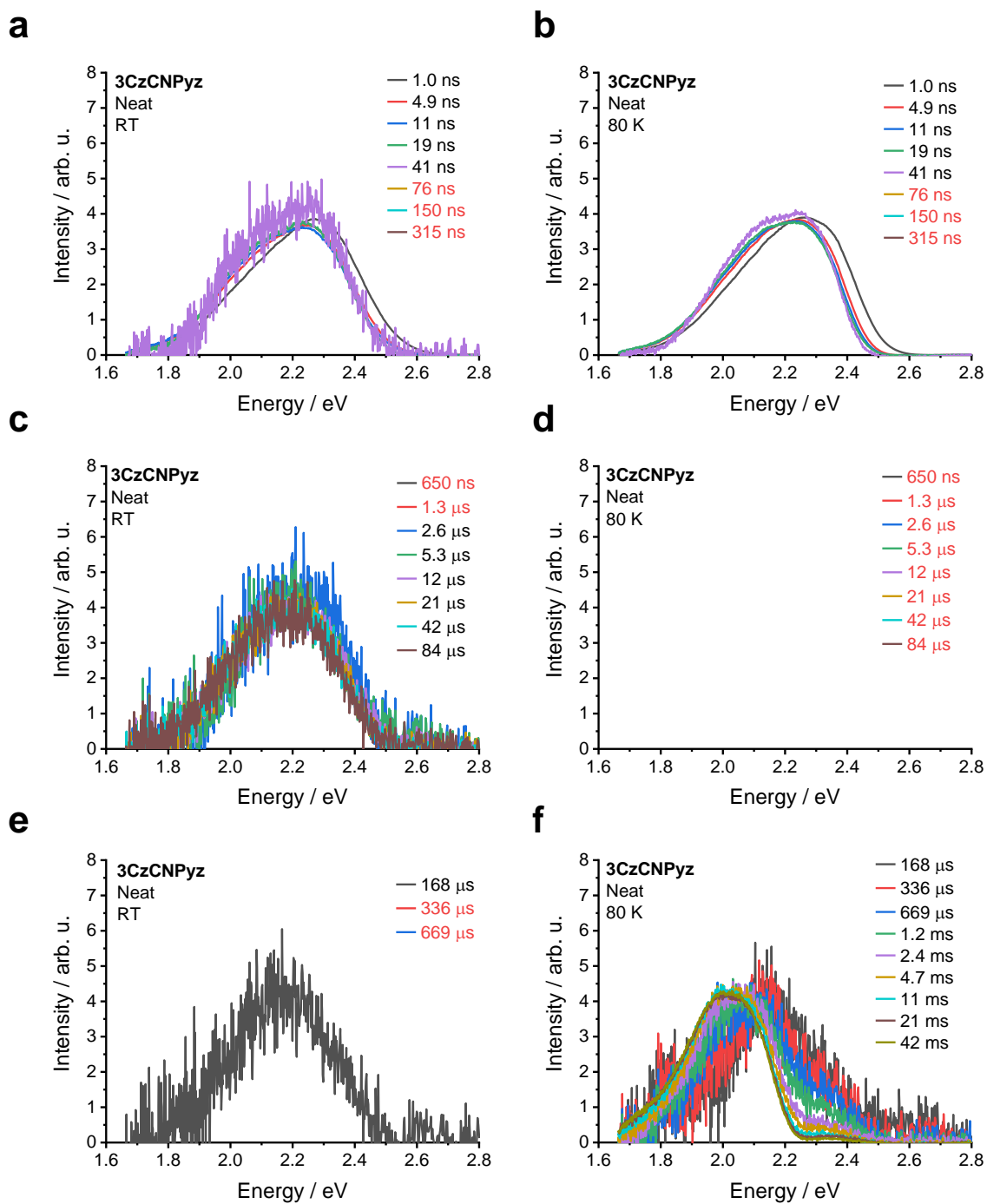
## 8. Time-resolved Photophysical Characterisation



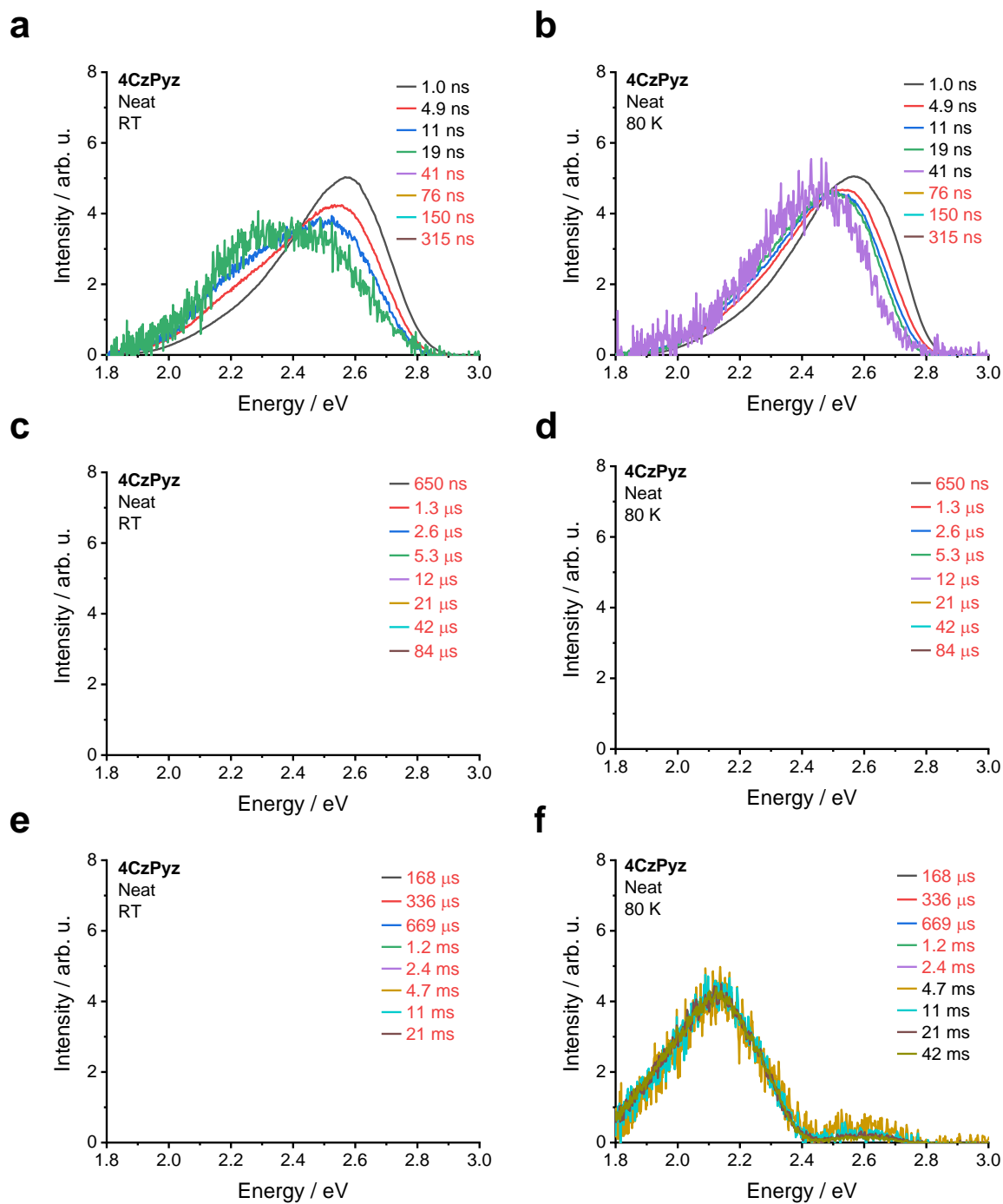
**Figure S31** The time-resolved photoluminescence kinetics in a neat film for (a,b) **2Cz2CNPyz**, (c,d) **3CzCNPyz** and (e,f) **4CzPyz** at (a,c,e) room temperature (RT) and (d,e,f) 80 K.



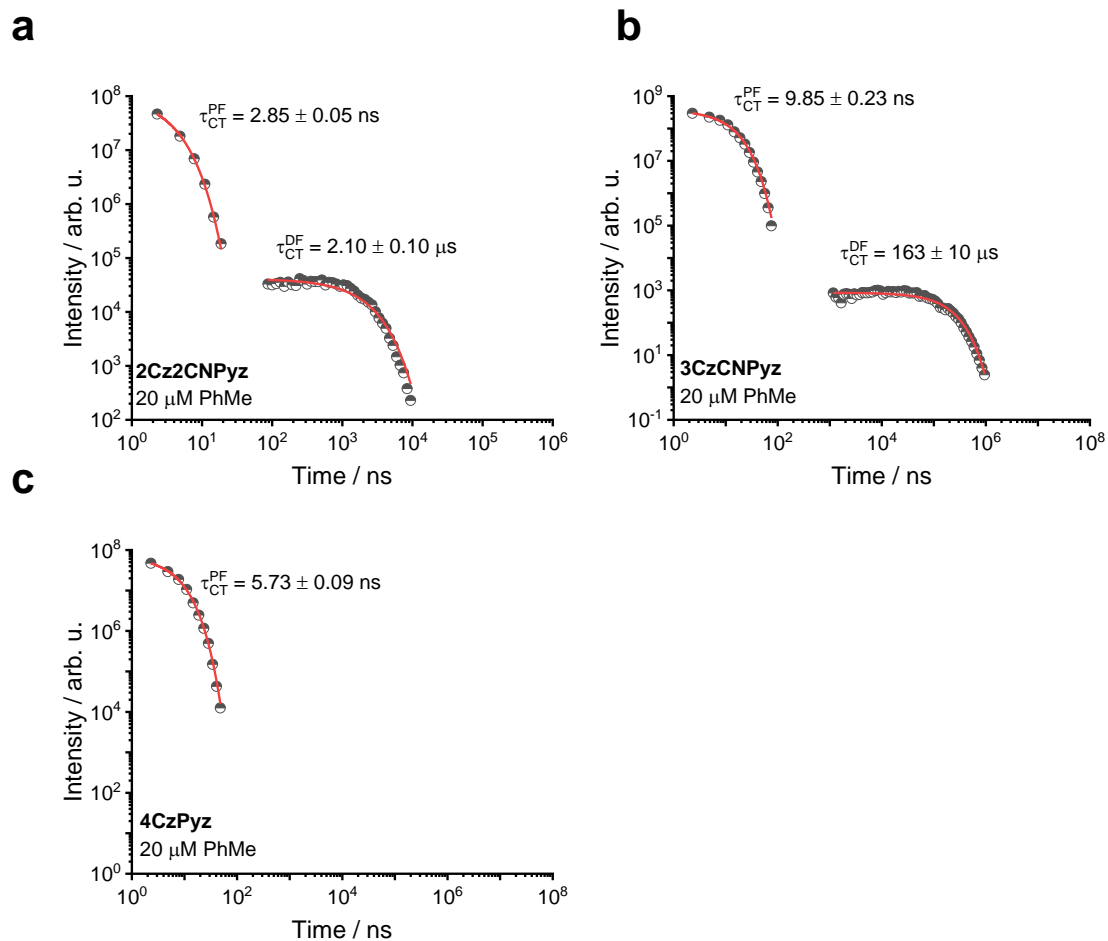
**Figure S32** The time-resolved photoluminescence spectra of a neat film of **2Cz2CNPyz** measured at (a,c,e) room temperature (RT) and (b,d,f) 80 K. The times in red indicate delay times where no measurable signal was found.



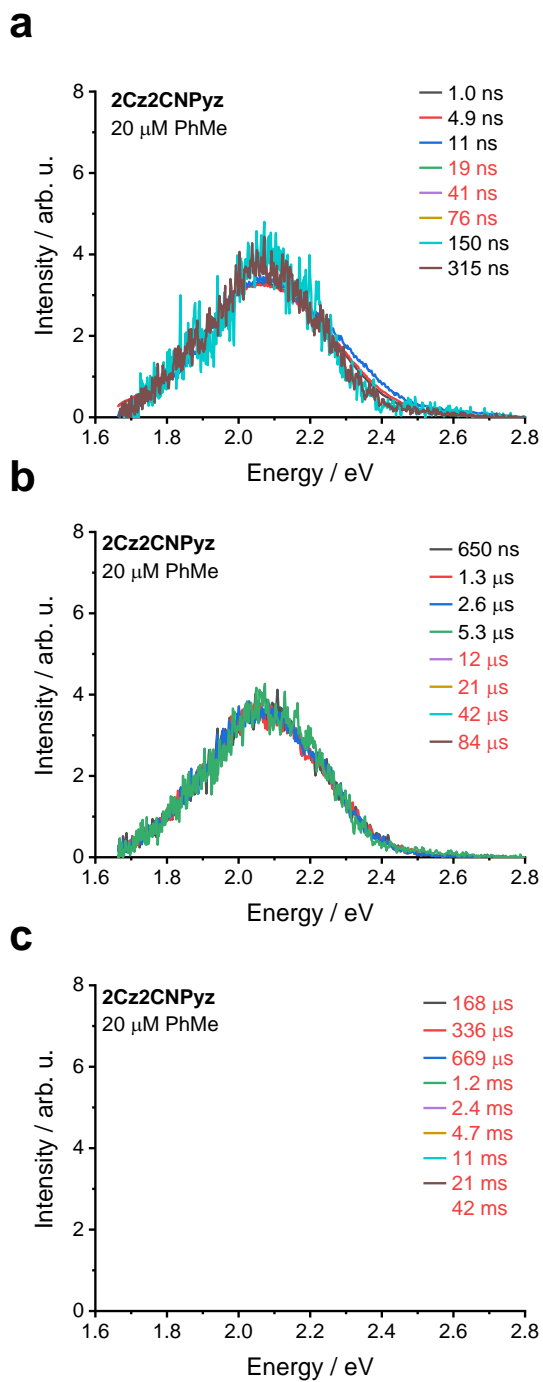
**Figure S33** The time-resolved photoluminescence spectra of a neat film of **3CzCNPyz** measured at (a,c,e) room temperature (RT) and (b,d,f) 80 K. The times in red indicate times where no measurable signal was found.



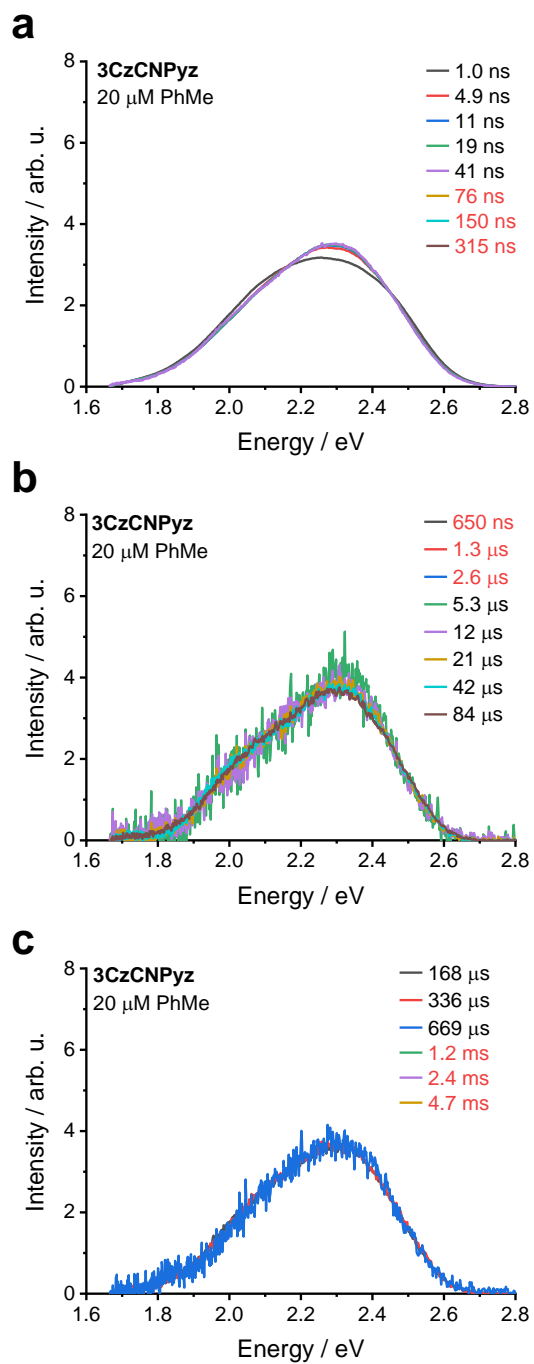
**Figure S34** The time-resolved photoluminescence spectra of a neat film of **4CzPyz** measured at (a,c,e) room temperature (RT) and (b,d,f) 80 K. The times in red indicate times where no measurable signal was found.



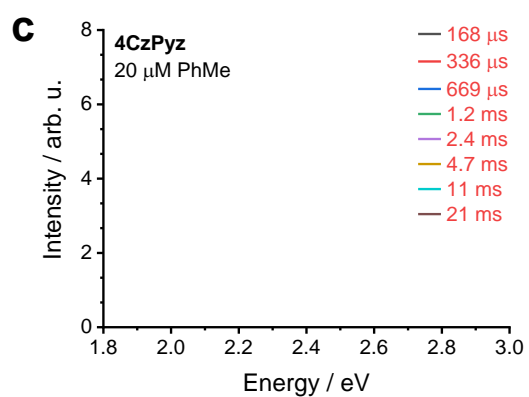
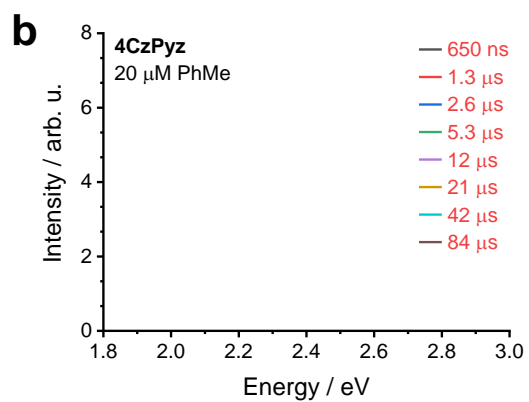
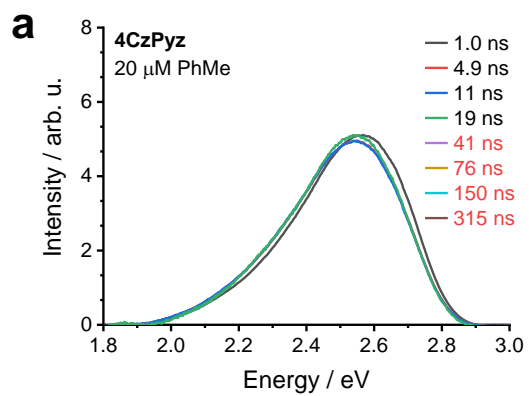
**Figure S35** The time-resolved photoluminescence kinetics in degassed toluene solution for (a) **2Cz2CNPyz**, (b) **3CzCNPyz** and (c) **4CzPyz** at room temperature (RT).



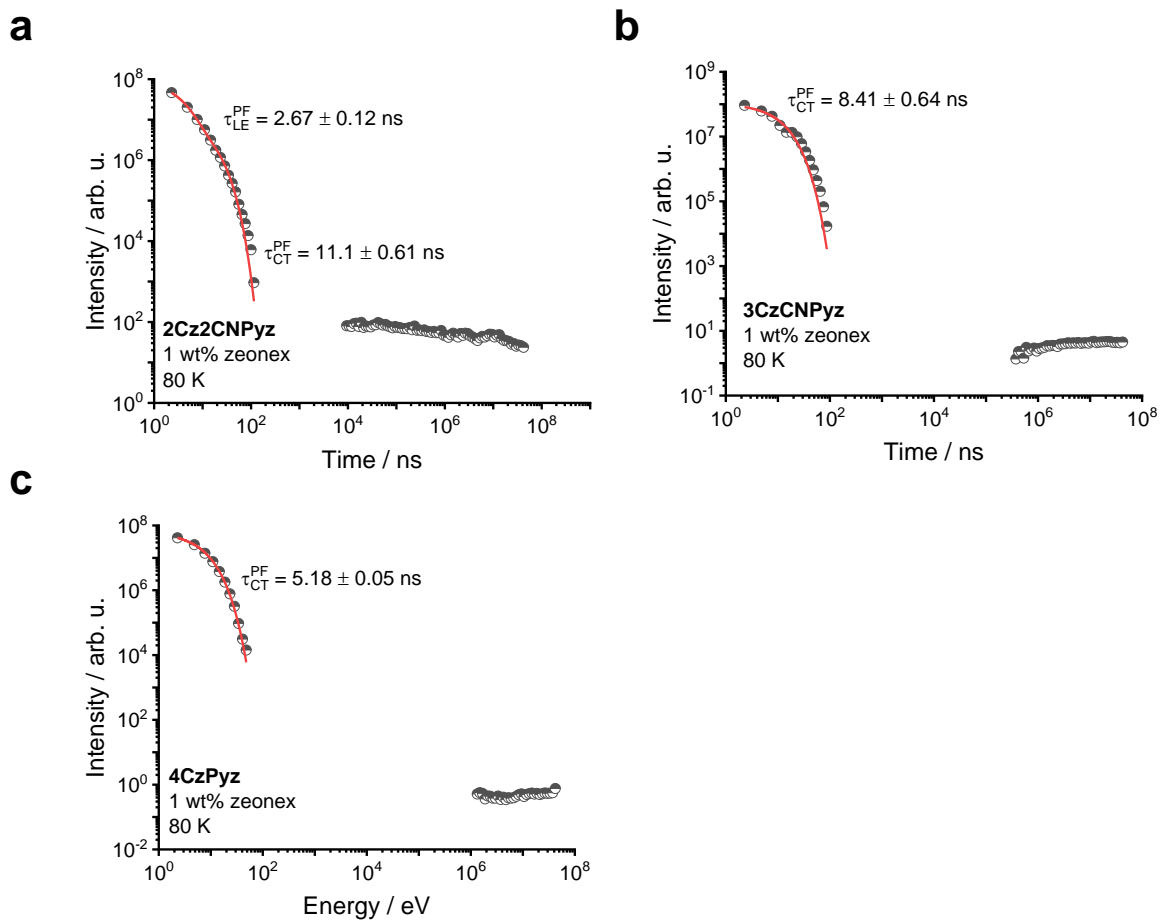
**Figure S36** The time-resolved photoluminescence spectra of a toluene solution of **2Cz2CNPyz** measured at (a,b, c) room temperature (RT). The times in red indicate times where no measurable signal was found.



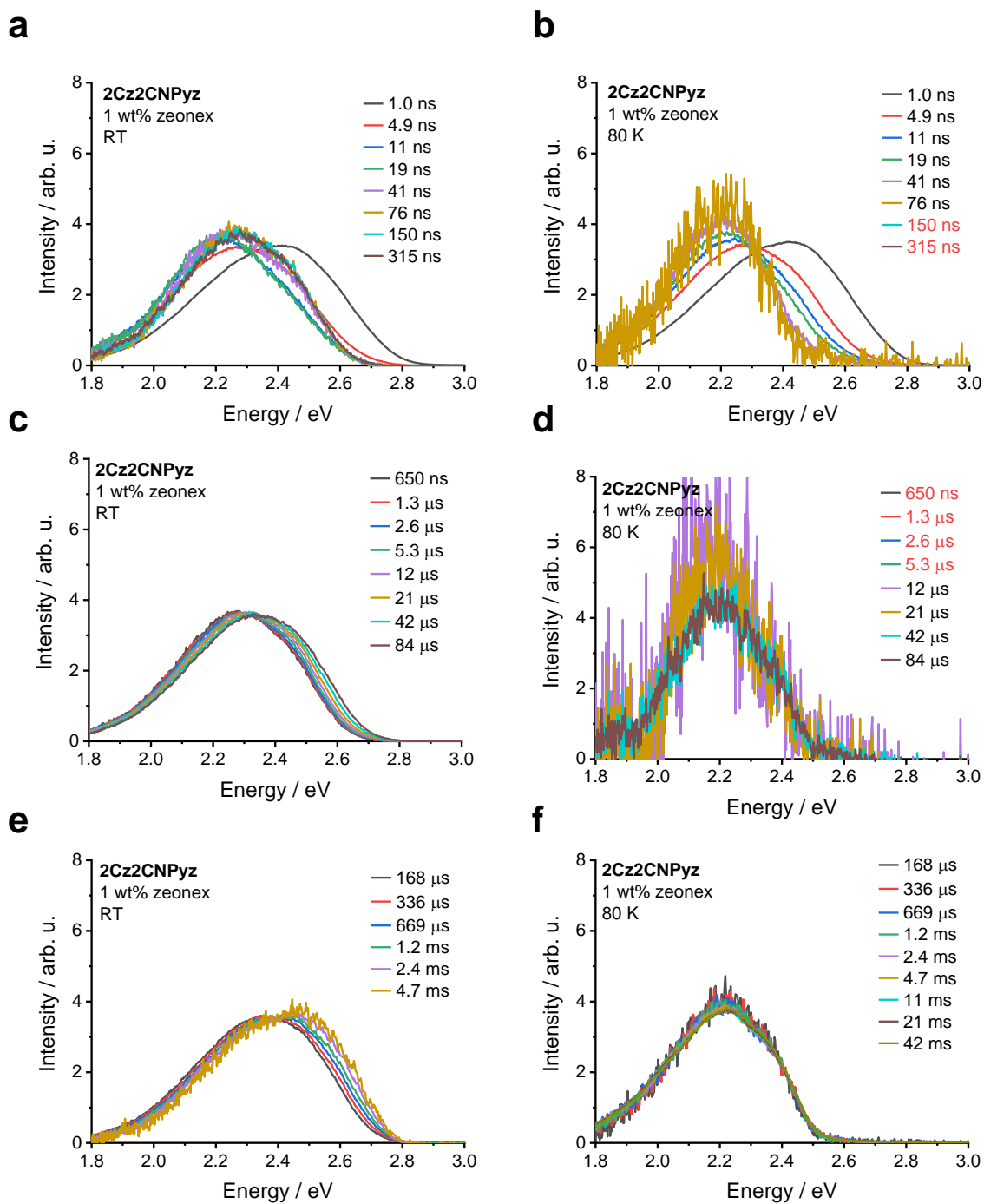
**Figure S37** The time-resolved photoluminescence spectra of a toluene solution of **3CzCNPyz** measured at (a,b,c) room temperature (RT). The times in red indicate times where no measurable signal was found.



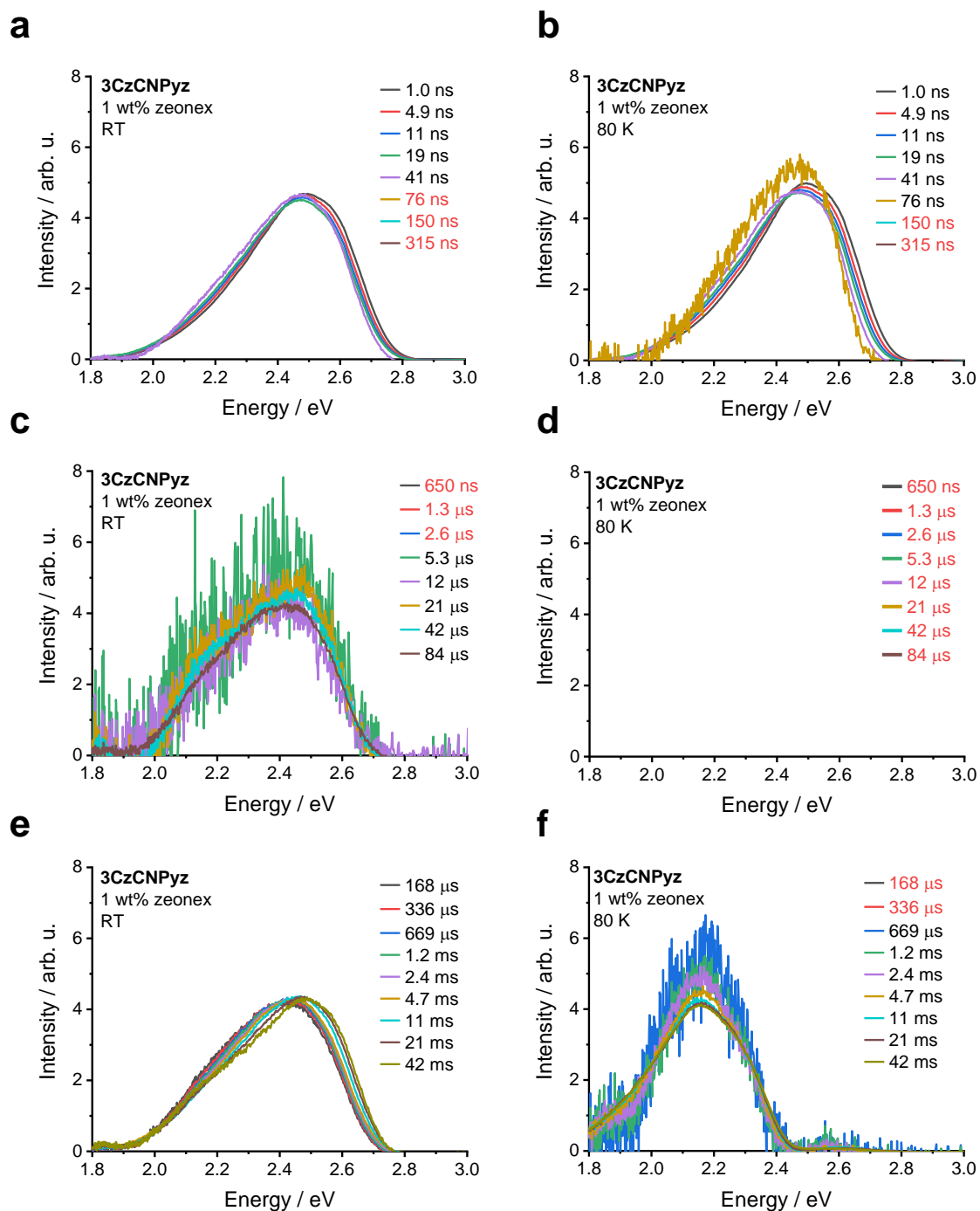
**Figure S38** The time-resolved photoluminescence spectra of a toluene solution of **4CzPyz** measured at (a,b,c) room temperature (RT). The times in red indicate times where no measurable signal was found.



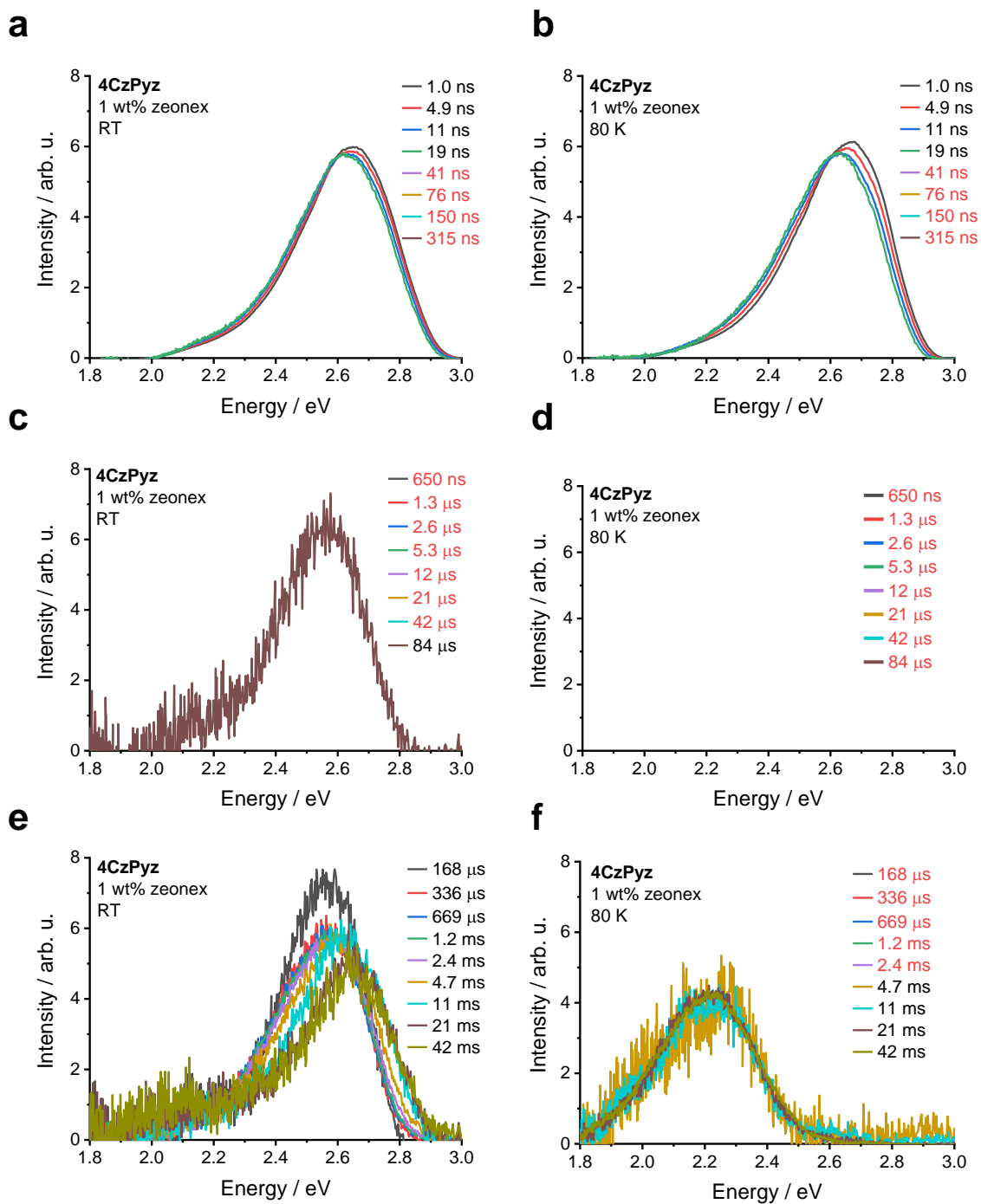
**Figure S39** The time-resolved photoluminescence kinetics in a 1 wt% zeonex film for (a) **2Cz2CNPyz**, (b) **3CzCNPyz** and (c) **4CzPyz** at 80 K.



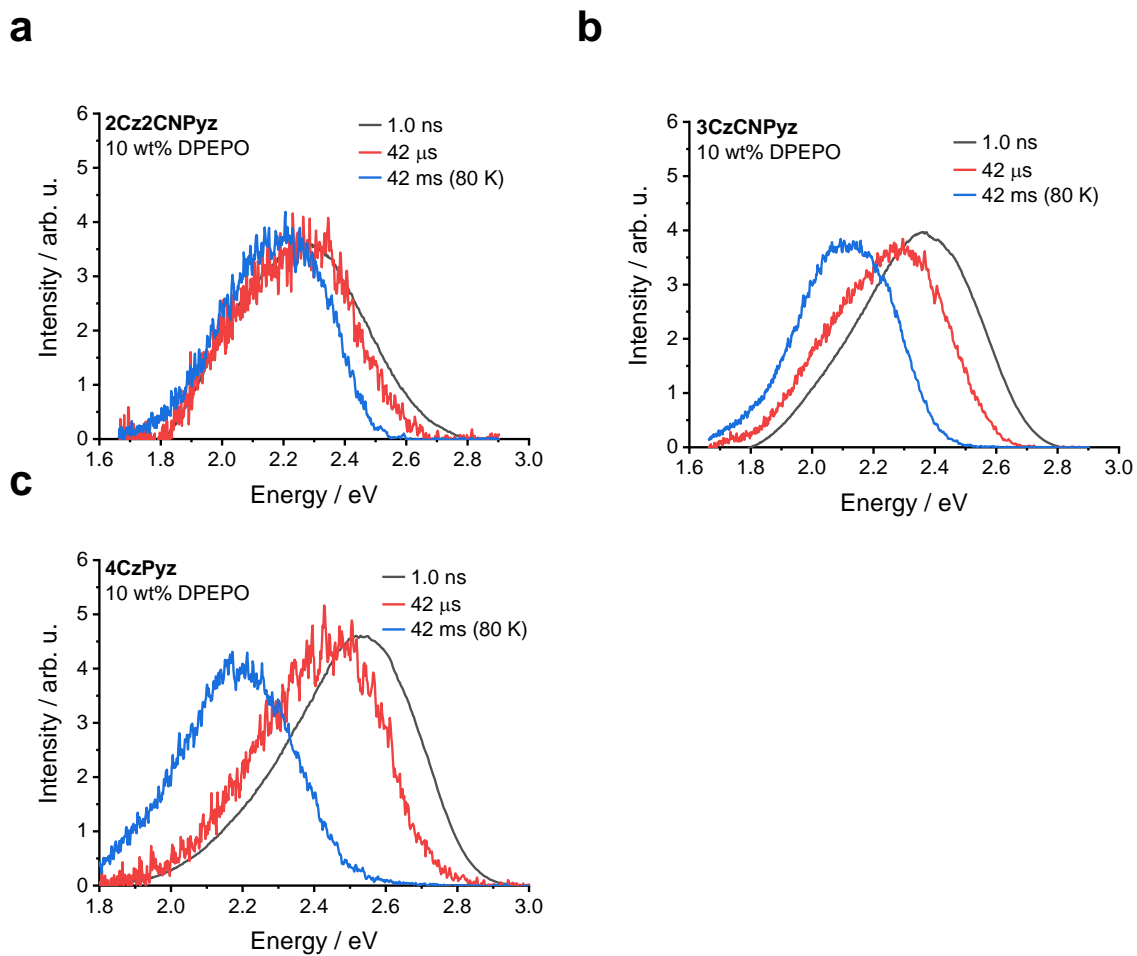
**Figure S40** The time-resolved photoluminescence spectra of a 1wt% zeonex film of **2Cz2CNPyz** measured at (a,c,e) room temperature (RT) and (b,d,f) 80 K. The times in red indicate times where no measurable signal was found.



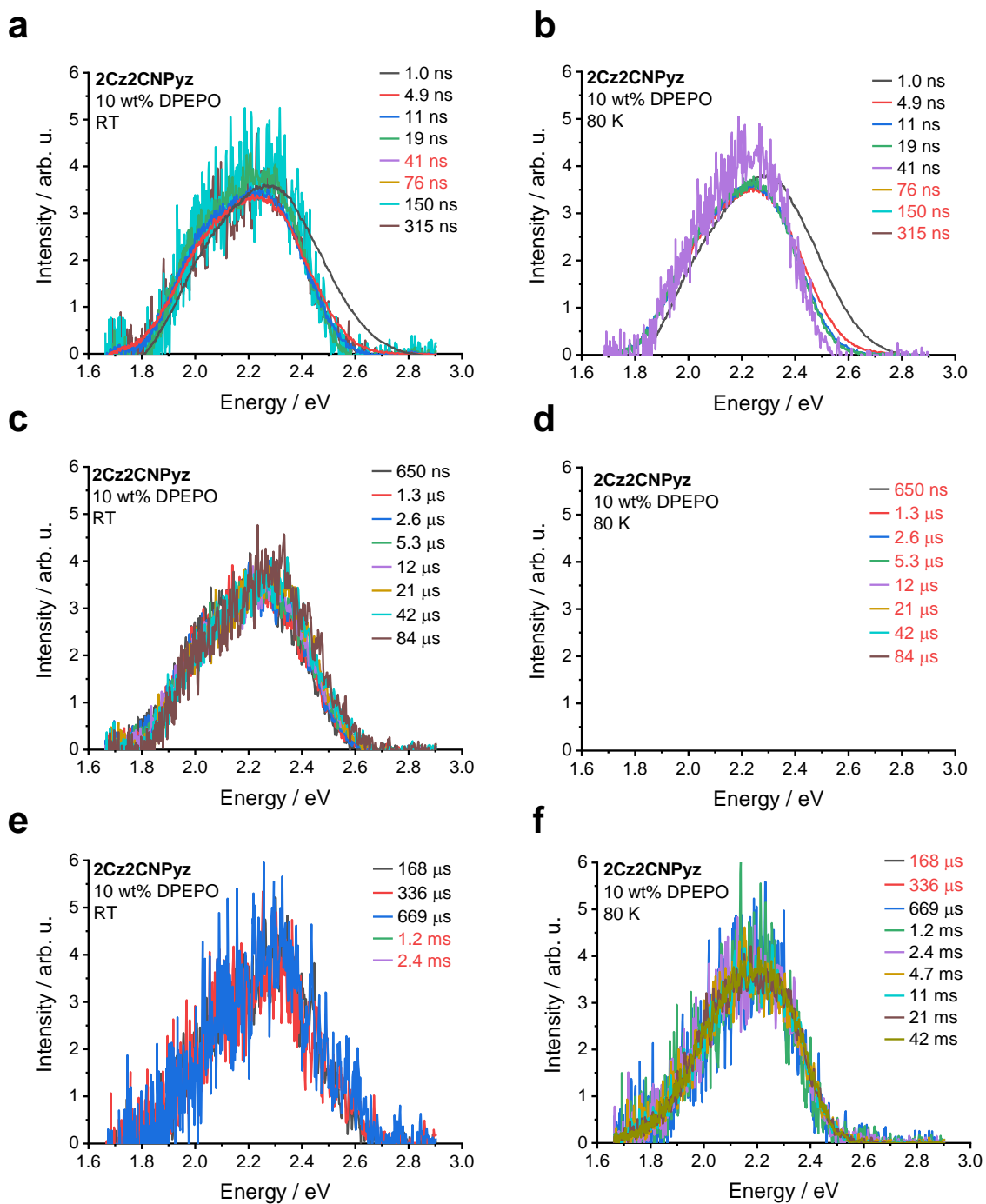
**Figure S41** The time-resolved photoluminescence spectra of a 1 wt% zeonex film of **3CzCNPyz** measured at (a,c,e) room temperature (RT) and (b,d,f) 80 K. The times in red indicate times where no measurable signal was found.



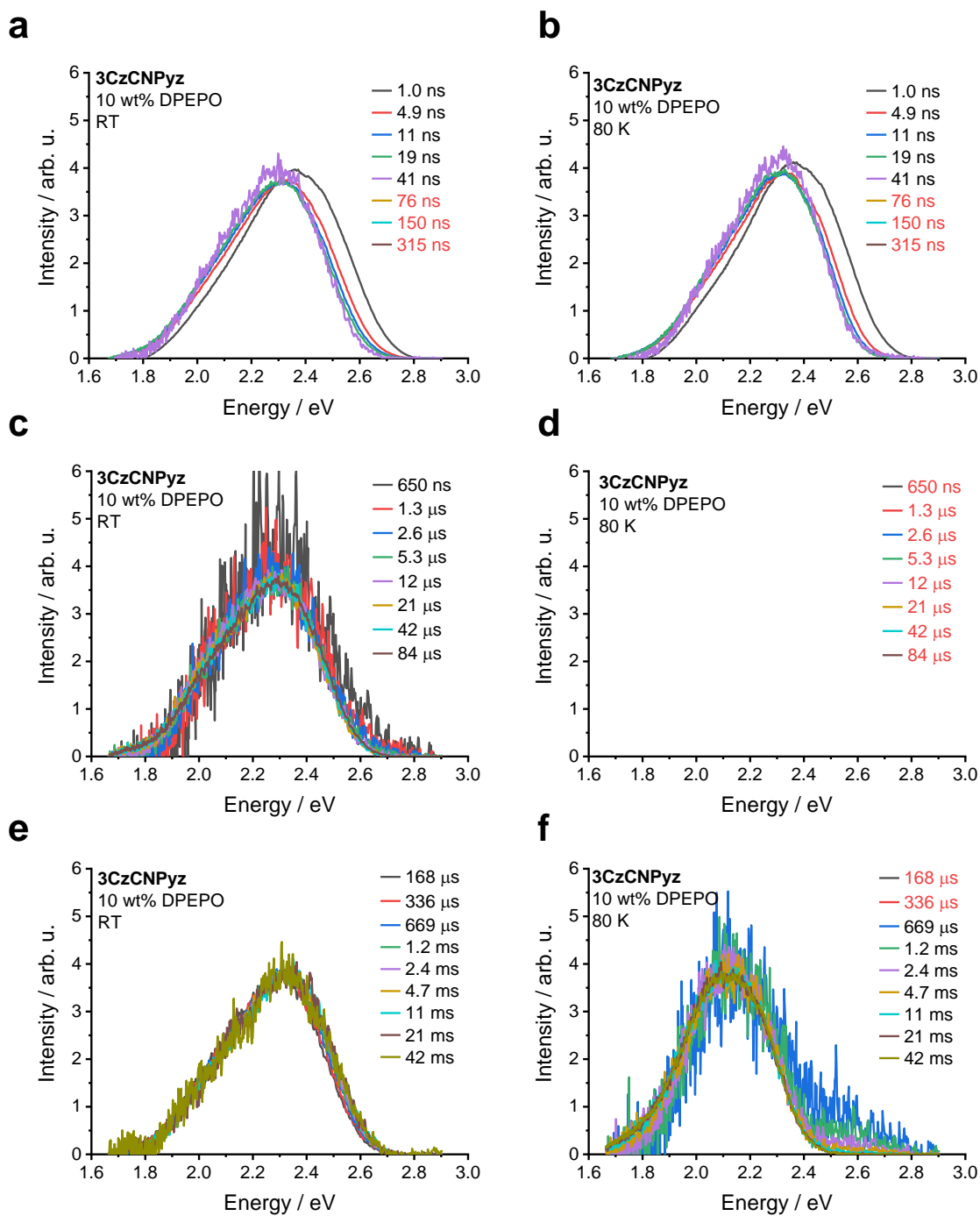
**Figure S42** The time-resolved photoluminescence spectra of a 1 wt% zeonex film of **4CzPyz** measured at (a,c,e) room temperature (RT) and (b,d,f) 80 K. The times in red indicate times where no measurable signal was found.



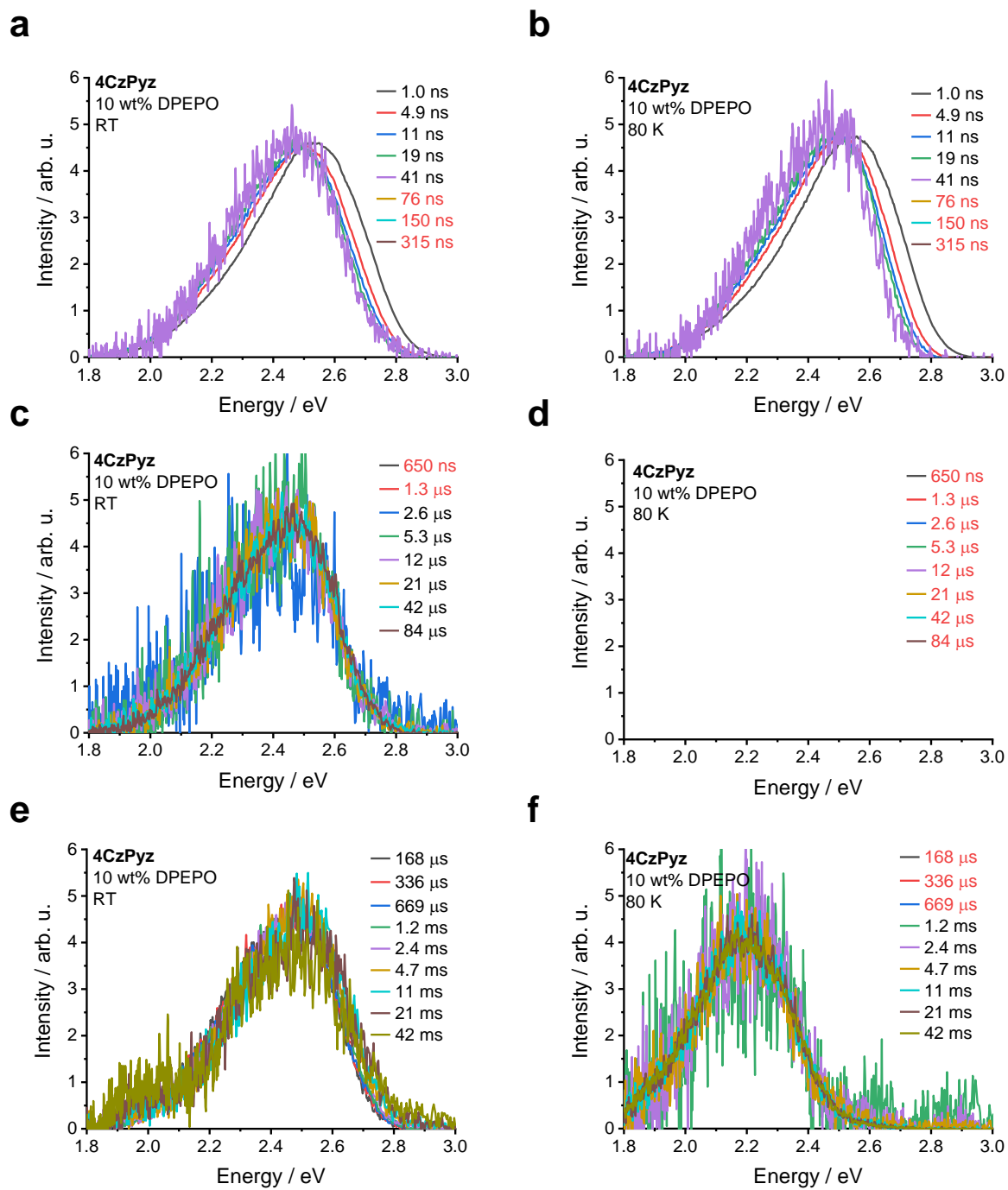
**Figure S43** The time-resolved photoluminescence spectra of (a) **2Cz2CNPyz**, (b) **3CzCNPyz** and (c) **4CzPyz** in a 10 wt% DPEPO film at room temperature (RT) and 80 K showing the singlet-triplet gaps between the prompt fluorescence (1.0 ns), delayed fluorescence (42 μs at room temperature) and phosphorescence (42 ms at 80 K)



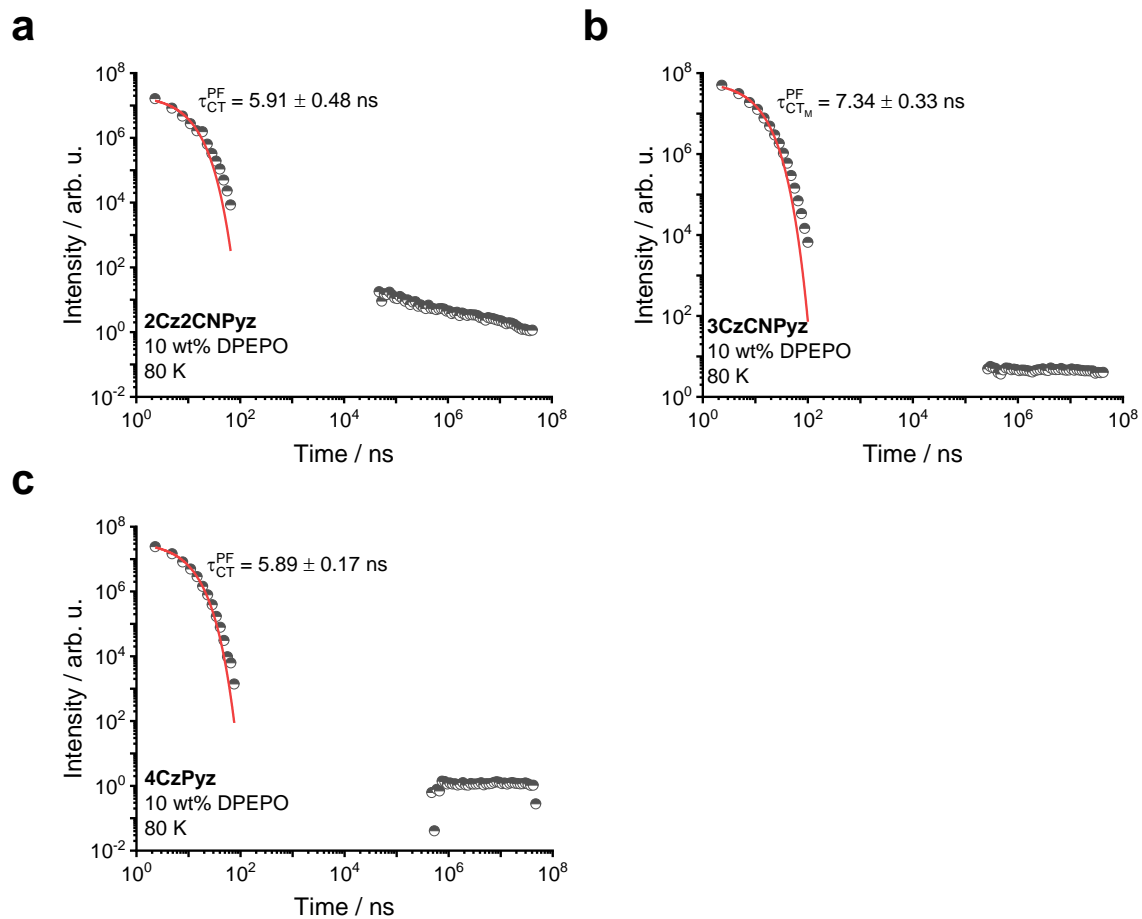
**Figure S44** The time-resolved photoluminescence spectra of a 10 wt% DPEPO film of **2Cz2CNPyz** at (a,c,e) room temperature (RT) and (d,e,f) 80 K. The times in red indicate times where no measurable signal was found.



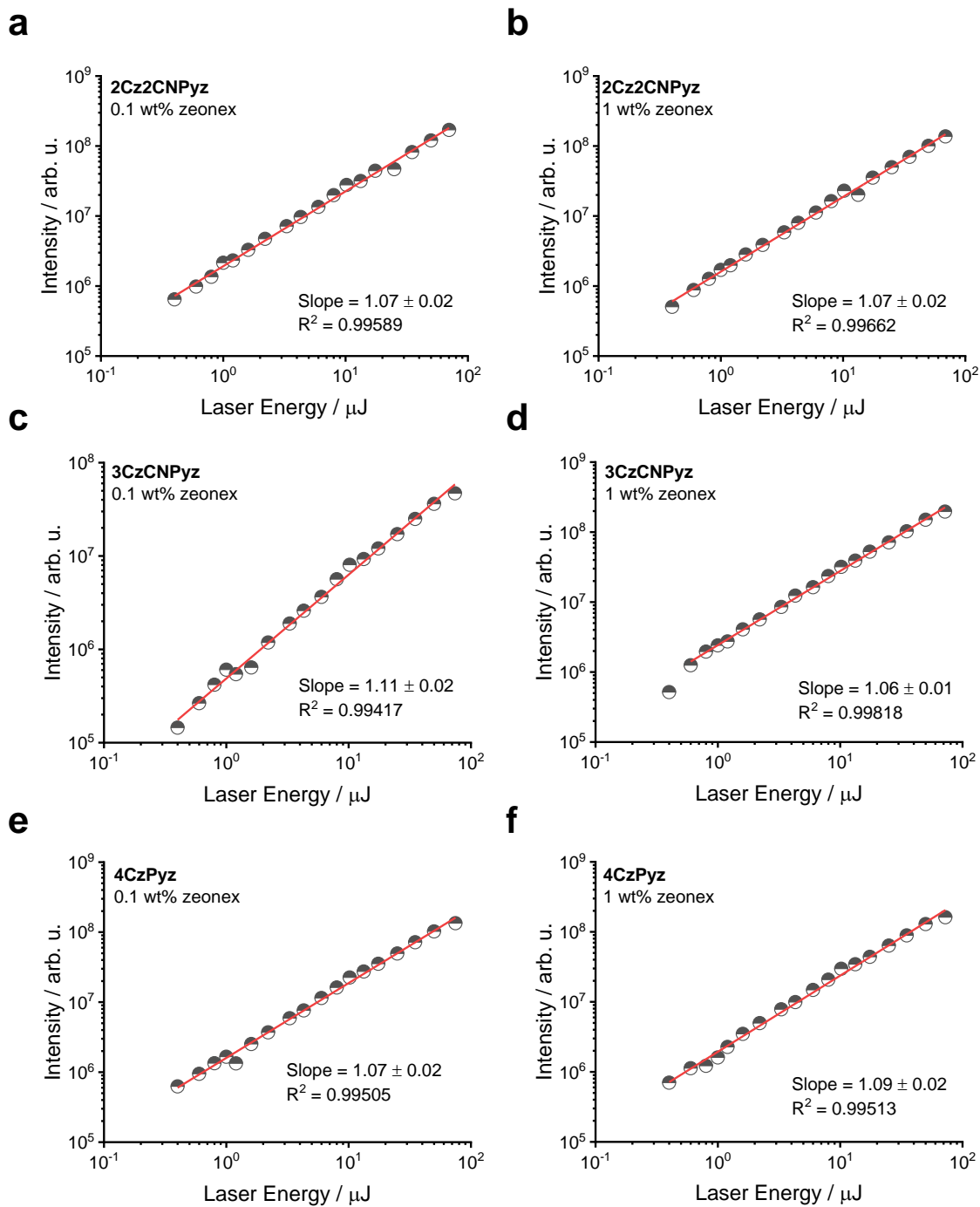
**Figure S45** The time-resolved photoluminescence spectra of a 10 wt% DPEPO film of **3CzCNPyz** at (a,c,e) room temperature (RT) and (d,e,f) 80 K. The times in red indicate times where no measurable signal was found.



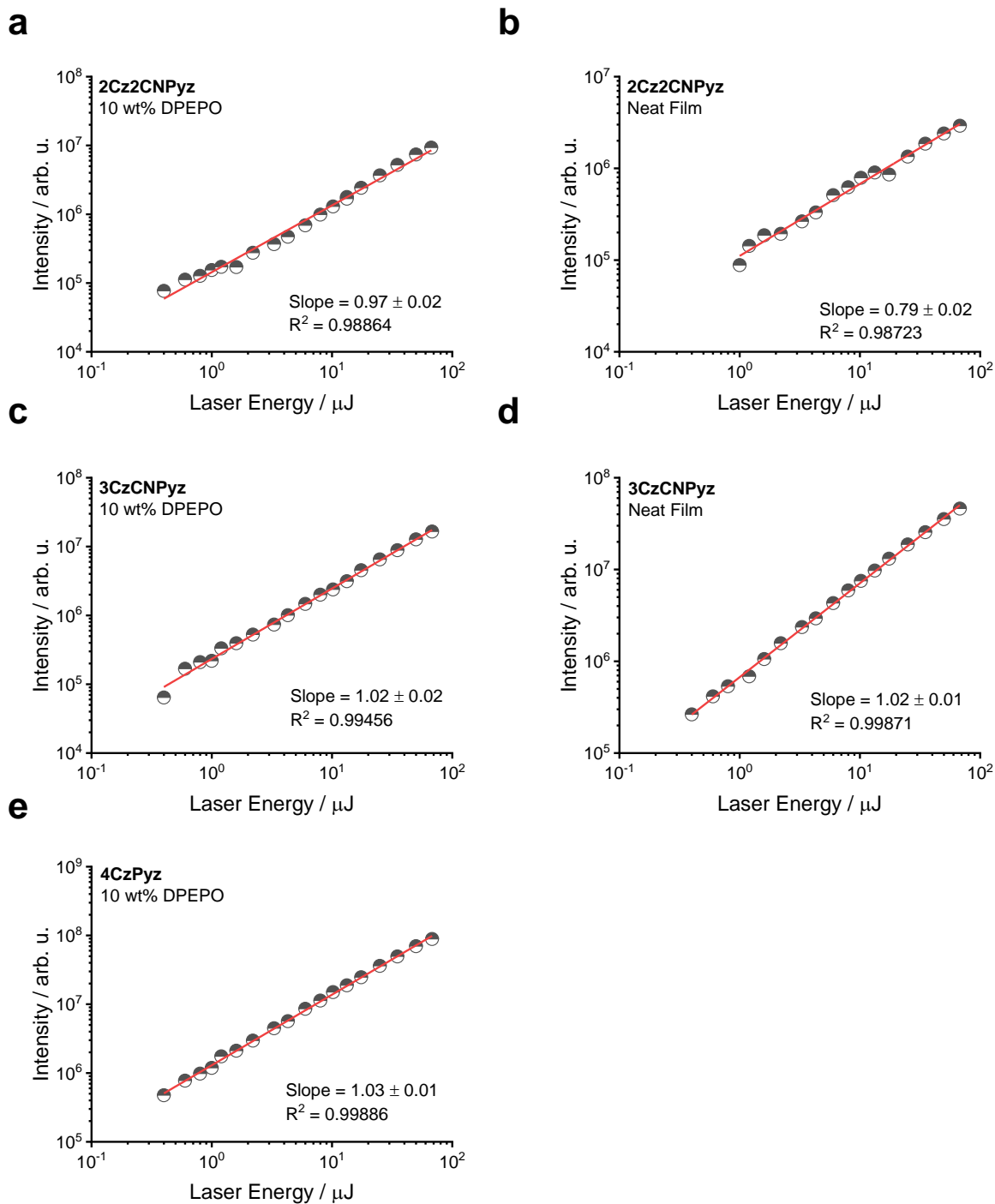
**Figure S46** The time-resolved photoluminescence spectra of a 10 wt% DPEPO film of **4CzPyz** at (a,c,e) room temperature (RT) and (d,e,f) 80 K. The times in red indicate times where no measurable signal was found.



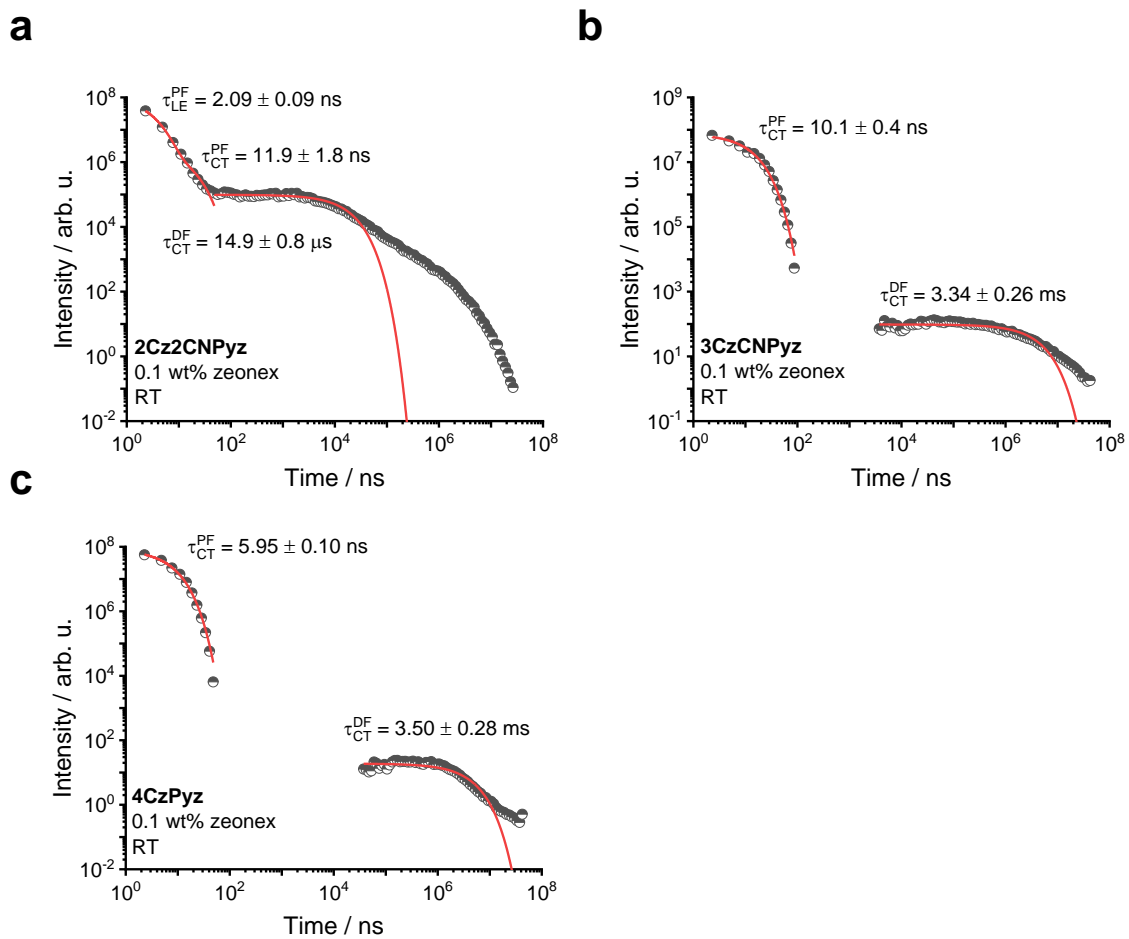
**Figure S47** The time-resolved photoluminescence kinetics of 10 wt% DPEPO films of (a) **2Cz2CNPyz**, (b) **3CzCNPyz** and (c) **4CzPyz** measured at 80 K.



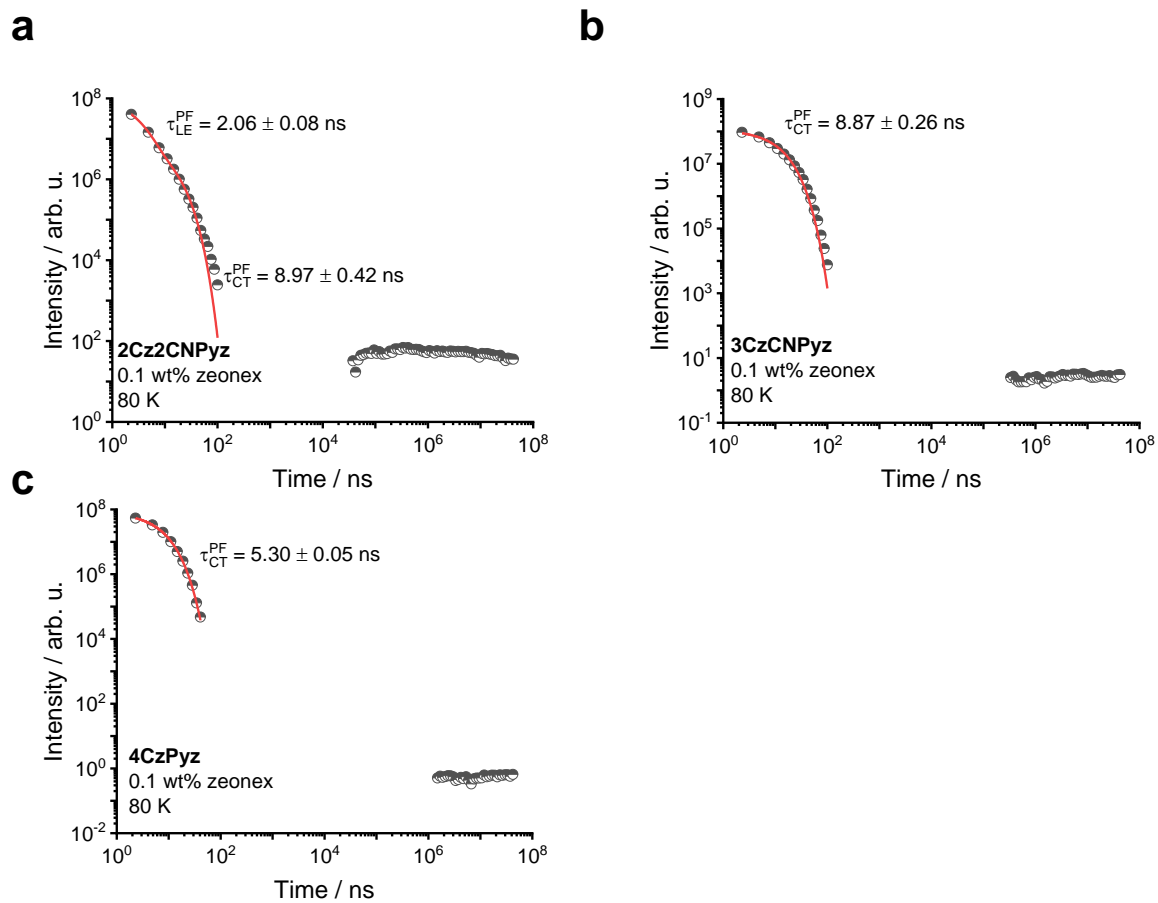
**Figure S48** Measurement of delayed fluorescence intensity versus laser energy for (a,c,e) 0.1 wt% zeonex films and (b,d,f) 1 wt% zeonex films of **2Cz2CNPyz**, **3CzCNPyz** and **4CzPyz** respectively.



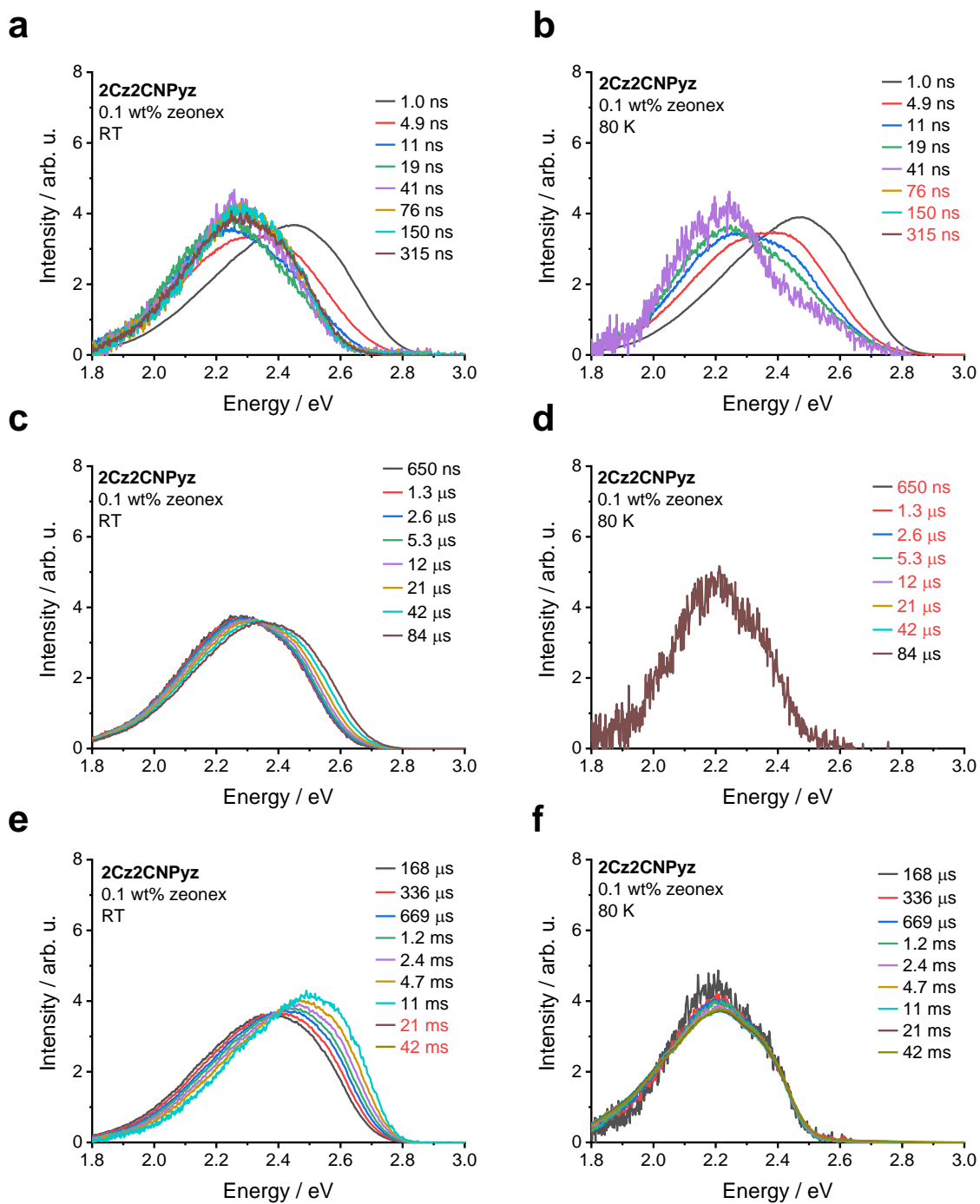
**Figure S49** Measurement of delayed fluorescence intensity versus laser energy for 10 wt% DPEPO films for (a) **2Cz2CNPyz**, (b) **3CzCNPyz** and (c) **4CzPyz**.



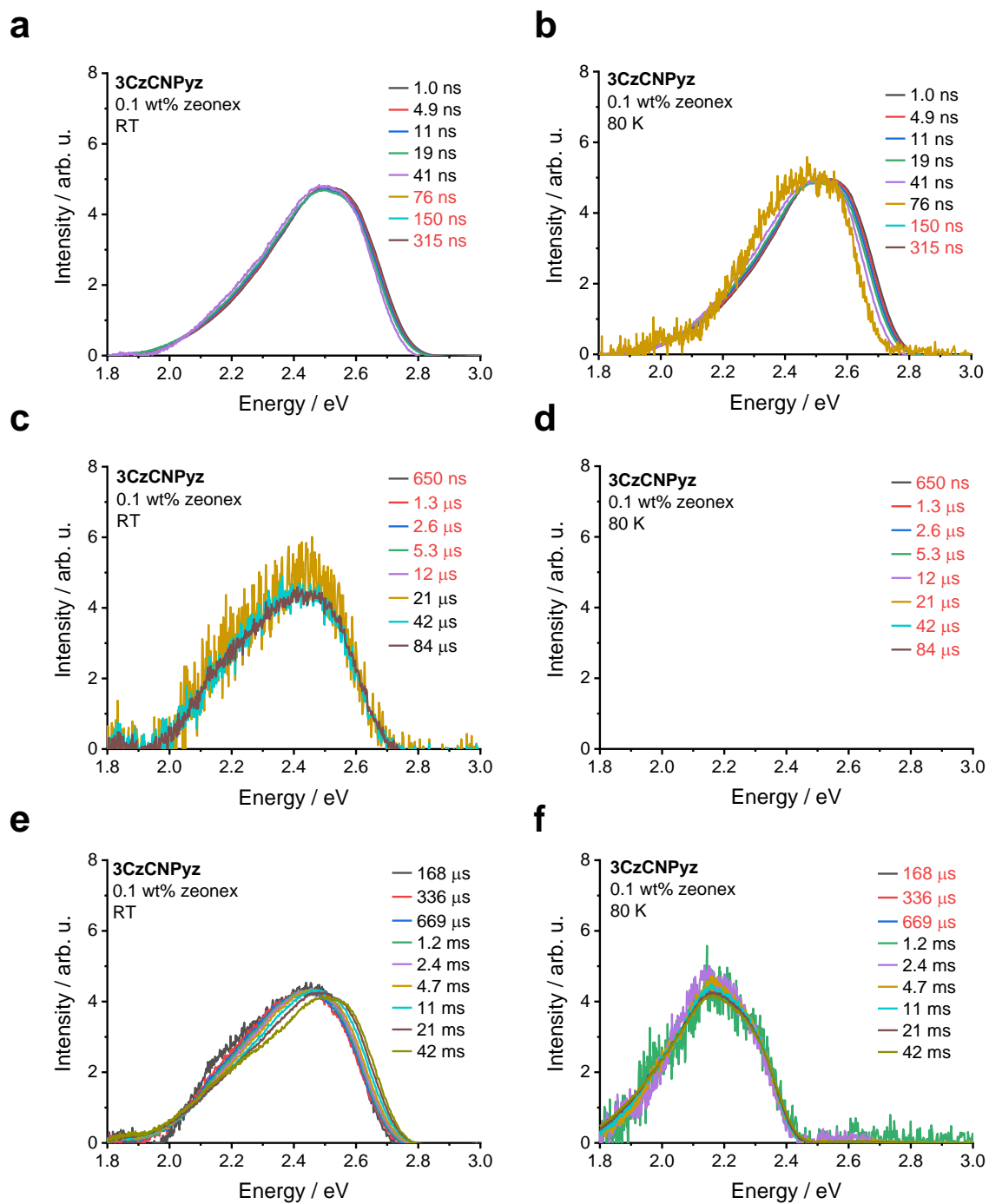
**Figure S50** The time-resolved photoluminescence kinetics of 0.1 wt% zeonex films of (a) **2Cz2CNPyz**, (b) **3CzCNPyz** and (c) **4CzPyz** at room temperature (RT).



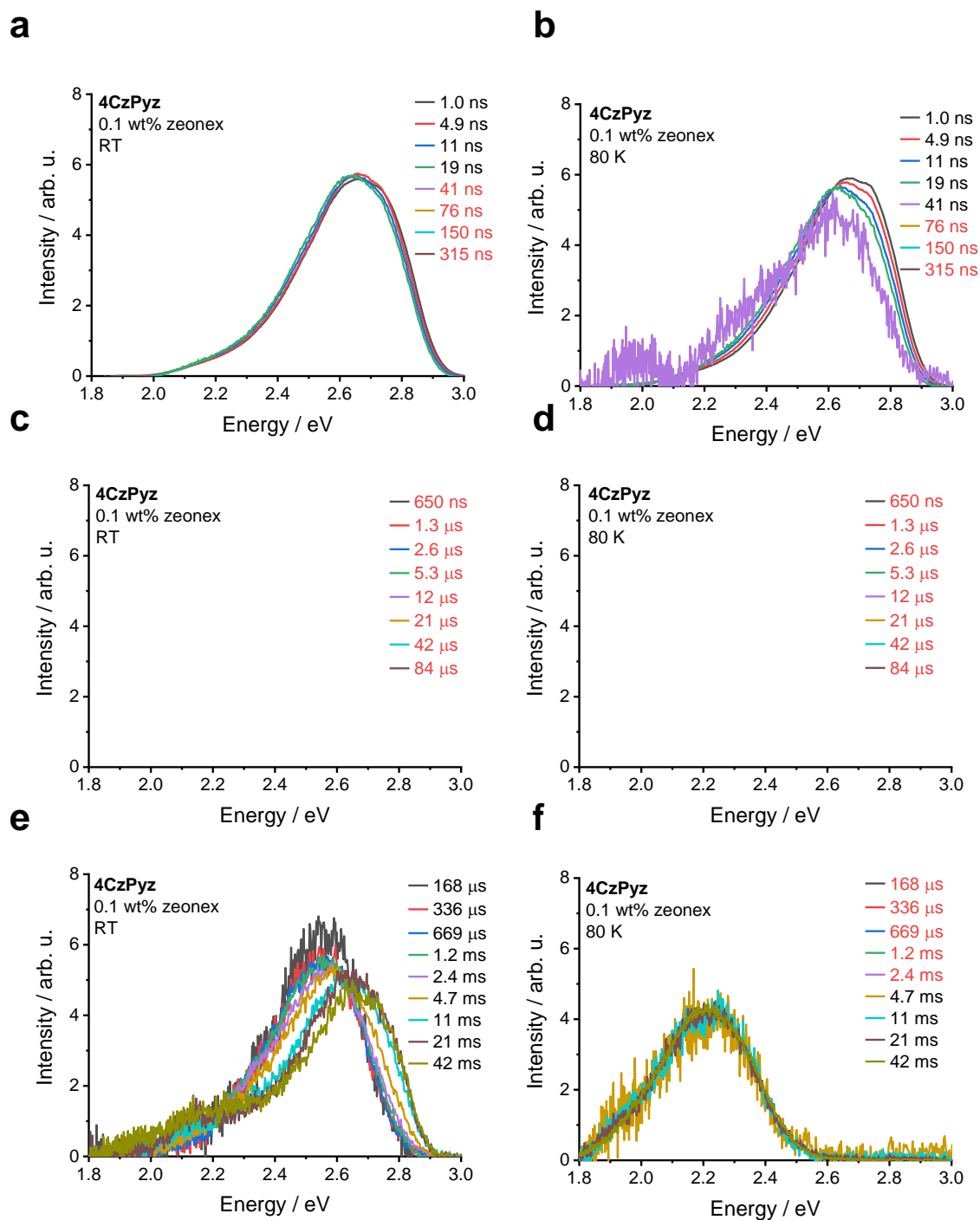
**Figure S51** The time-resolved photoluminescence kinetics of 0.1 wt% zeonex films of (a) **2Cz2CNPyz**, (b) **3CzCNPyz** and (c) **4CzPyz** at 80 K.



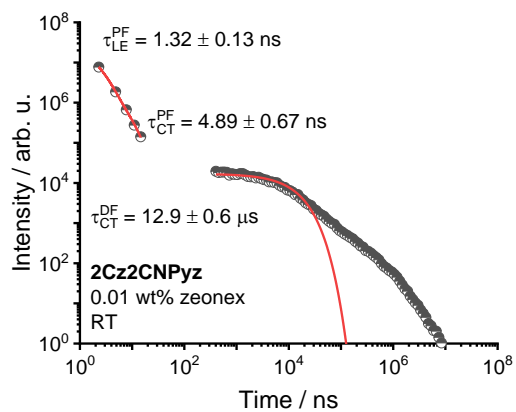
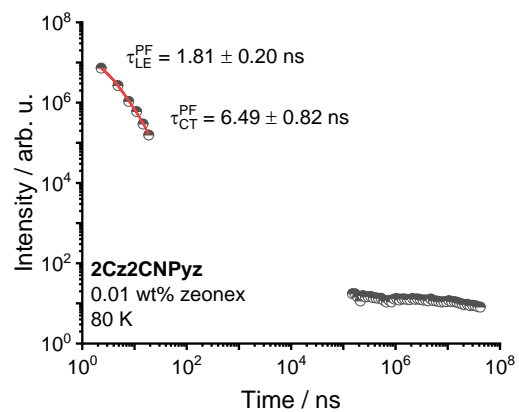
**Figure S52** The time-resolved photoluminescence spectra of a 0.1 wt% zeonex film of **2Cz2CNPyz** at (a,c,e) room temperature (RT) and (d,e,f) 80 K. The times in red indicate times where no measurable signal was found.



**Figure S53** The time-resolved photoluminescence spectra of a 0.1 wt% zeonex film of **3CzCNPyz** at (a,c,e) room temperature (RT) and (d,e,f) 80 K. The times in red indicate times where no measurable signal was found.



**Figure S54** The time-resolved photoluminescence spectra of a 0.1 wt% zeonex film of **4CzPyz** at (a,c,e) room temperature (RT) and (d,e,f) 80 K. The times in red indicate times where no measurable signal was found.

**a****b**

**Figure S55** The time-resolved photoluminescence kinetics of a 0.01 wt% zeonex film of **2Cz2CNPyz** at (a) room temperature (RT) and (b) 80 K.

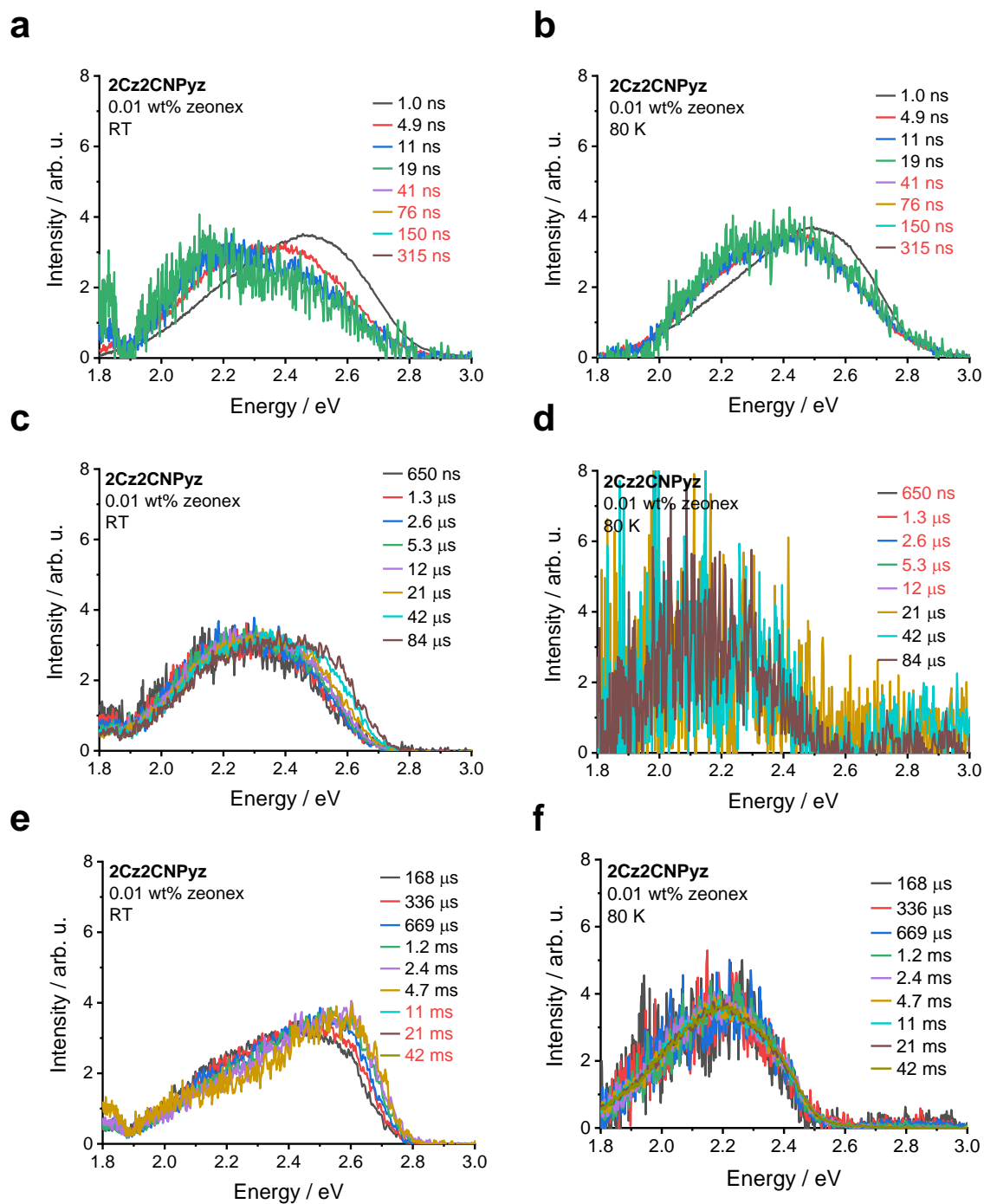


**Figure S56** The time-resolved photoluminescence spectra of a 0.01 wt% zeonex film of **2Cz2CNPyz** at (a,c,e) room temperature (RT) and (d,e,f) 80 K. The times in red indicate times where no measurable signal was found.

**Table S9** Amplitude (a) and lifetime ( $\tau$ ) parameters for **2Cz2CNPyz** neat film.  $R^2$  for prompt fluorescence (PF) is 0.98823 and for delayed fluorescence (DF) is 0.95739 and 0.9796 for the 80 K PF. CT stands for charge transfer state.

Temperature	aPF/CT	$\tau$ PF/CT	aDF/CT	$\tau$ DF/CT
RT	4.484E7 $\pm$ 0.317E7	3.035 $\pm$ 0.139	3.683E4 $\pm$ 0.131E4	7.304E2 $\pm$ 0.418E2
80 K	5.133E7 $\pm$ 0.389E7	4.531 $\pm$ 0.252		

**Table S10** Amplitude (a) and lifetime ( $\tau$ ) parameters for **3CzCNPyz** neat film.  $R^2$  for PF is 0.98753 and for DF is 0.95799 and 0.98473 for the 80 K PF. CT stands for charge transfer state.

Temperature	aPF/CT	$\tau$ PF/CT	aDF/CT	$\tau$ DF/CT
RT	5.147E7 $\pm$ 0.300E7	4.828 $\pm$ 0.209	6.110E2 $\pm$ 0.245E2	1.764E4 $\pm$ 0.113E4
80 K	1.102E8 $\pm$ 0.061E8	6.134 $\pm$ 0.268		

**Table S11** Amplitude (a) and lifetime ( $\tau$ ) parameters for **4CzPyz** neat film.  $R^2$  for PF is 0.99971 and 0.99829 for the 80 K PF. CTM stands for monomer charge transfer state and CTD stands for dimer charge transfer state.

Temperature	aPF/CTM	$\tau$ PF/CTM	aPF/CTD	$\tau$ PF/CTD
RT	4.267E7 $\pm$ 0.089E7	1.964 $\pm$ 0.062	4.230E6 $\pm$ 0.893E6	5.235 $\pm$ 0.272
80 K	1.077E8 $\pm$ 0.043E8	2.920 $\pm$ 0.187	1.721E7 $\pm$ 0.512E7	7.410 $\pm$ 0.650

**Table S12** Amplitude (a) and lifetime ( $\tau$ ) parameters for **2Cz2CNPyz** 20  $\mu$ M Toluene degassed solution.  $R^2$  for PF is 0.99898 and for DF is 0.96995. CT stands for charge transfer state.

Temperature	aPF/CT	$\tau$ PF/CT	aDF/CT	$\tau$ DF/CT
RT	1.035E8 $\pm$ 0.027E8	2.848 $\pm$ 0.046	4.095E4 $\pm$ 0.129E4	2.100E3 $\pm$ 0.100E3

**Table S13** Amplitude (a) and lifetime ( $\tau$ ) parameters for **3CzCNPyz** 20  $\mu$ M Toluene degassed solution.  $R^2$  for PF is 0.99789 and for DF is 0.95224. CT stands for charge transfer state.

Temperature	aPF/CT	$\tau$ PF/CT	aDF/CT	$\tau$ DF/CT
RT	3.742E8 $\pm$ 0.061E8	9.854 $\pm$ 0.232	8.435E2 $\pm$ 0.265E2	1.639E5 $\pm$ 0.104E5

**Table S14** Amplitude (a) and lifetime ( $\tau$ ) parameters for **4CzPyz** 20  $\mu$ M Toluene degassed solution.  $R^2$  for PF at RT is 0.99929. CT stands for charge transfer state.

Temperature	aPF/CT	$\tau$ PF/CT
RT	7.006E7 $\pm$ 0.089E7	5.729 $\pm$ 0.090

**Table S15** Amplitude (a) and lifetime ( $\tau$ ) parameters for **2Cz2CNPyz** 1 wt% zeonex film.  $R^2$  for PF is 0.99906 and for DF is 0.96688 and 0.9981 for the 80 K PF. LE stands for locally excited state and CT stands for charge transfer state.

Temperature	aPF/LE	$\tau$ PF/LE	aPF/CT	$\tau$ PF/CT	aDF/CT	$\tau$ DF/CT
RT	9.892E7 $\pm$	2.408 $\pm$	4.088E6 $\pm$	13.377 $\pm$	2.250E5 $\pm$	10.973E3 $\pm$
	0.293E7	0.074	0.696E5	1.373	0.050E5	0.584E3
80 K	9.004E7 $\pm$	2.668 $\pm$	9.995E6 $\pm$	11.110 $\pm$		
	0.320E6	0.116	1.245E6	0.610		

**Table S16** Amplitude (a) and lifetime ( $\tau$ ) parameters for **3CzCNPyz** 1 wt% zeonex film.  $R^2$  for PF is 0.99708 and for DF is 0.94527 and 0.96043 for 80 K PF. CT stands for charge transfer state.

Temperature	aPF/CT	$\tau$ PF/CT	aDF/CT	$\tau$ DF/CT
RT	1.346E8 $\pm$	8.388 $\pm$	2.108E2 $\pm$	1.615E6 $\pm$
	0.029E8	0.149	0.061E2	0.122E6
80 K	1.075E8 $\pm$	8.408 $\pm$		
	0.096E8	0.644		

**Table S17** Amplitude (a) and lifetime ( $\tau$ ) parameters for **4CzPyz** 1 wt% zeonex film.  $R^2$  for PF is 0.99975 and for DF is 0.98435 and 0.99934 for the 80 K PF. CT stands for charge transfer state.

Temperature	aPF/CT	$\tau$ PF/CT	aDF/CT	$\tau$ DF/CT
RT	8.084E7 $\pm$	5.268 $\pm$	3.161E1 $\pm$	1.473E6 $\pm$
	0.067E7	0.032	0.056E1	0.053E6
80 K	6.445E7 $\pm$	5.184 $\pm$		
	0.085E7	0.050		

**Table S18** Amplitude (a) and lifetime ( $\tau$ ) parameters for **2Cz2CNPyz** 10 wt% DPEPO film.  $R^2$  for RT is 0.97957 for PF and 0.97441 for DF and 0.95887 for 80 K PF. CT stands for charge transfer state.

Temperature	aPF/CT	$\tau$ PF/CT	aDF/CT	$\tau$ DF/CT
RT	1.836E7 $\pm$	4.299 $\pm$	2.258E4 $\pm$	3.997E3 $\pm$
	0.132E7	0.223	0.047E4	0.163E3
80 K	2.070E7 $\pm$	5.910 $\pm$		
	0.212E7	0.480		

**Table S19** Amplitude (a) and lifetime ( $\tau$ ) parameters for **3CzCNPyz** 10 wt% DPEPO film.  $R^2$  for PF is 0.99191 and for DF is 0.95668 and 0.98348 for 80 K PF. CT stands for charge transfer state.

Temperature	aPF/CT	$\tau$ PF/CT	aDF/CT	$\tau$ DF/CT
RT	1.103E8 $\pm$	6.884 $\pm$	4.391E3 $\pm$	9.918E4 $\pm$
	0.043E8	0.215	0.103E3	0.651E4
80 K	6.179E7 $\pm$	7.336 $\pm$		
	0.337E7	0.328		

**Table S20** Amplitude (a) and lifetime ( $\tau$ ) parameters for **4CzPyz** 10 wt% DPEPO film.  $R^2$  for PF is 0.97622 and for DF is 0.9383 and 0.99368 for the 80 K PF. CT stands for charge transfer state.

Temperature	aPF/CT	$\tau$ PF/CT	aDF/CT	$\tau$ DF/CT
RT	7.219E7 $\pm$	5.021 $\pm$	5.950E2 $\pm$	1.739E5 $\pm$
	0.543E7	0.285	0.172E2	0.141E5
80 K	3.386E7 $\pm$	5.887 $\pm$		
	0.123E7	0.165		

**Table S21** Amplitude (a) and lifetime ( $\tau$ ) parameters for **2Cz2CNPyz** 0.1 wt% zeonex film.  $R^2$  for PF is 0.99657 and for DF is 0.9705 and 0.99862 for the 80 K PF. LE stands for locally excited state and CT stands for charge transfer state.

Temperature	aPF/LE	$\tau$ PF/LE	aPF/CT	$\tau$ PF/CT	aDF/CT	$\tau$ DF/CT
RT	1.079E8 $\pm$	2.094 $\pm$	2.561E6 $\pm$	11.876 $\pm$	9.807E4 $\pm$	1.494E4 $\pm$
	0.057E8	0.091	0.749E6	1.838	0.202E4	0.075E4
80 K	1.026E8 $\pm$	2.063 $\pm$	8.581E6 $\pm$	8.971 $\pm$		
	0.037E8	0.076	0.937E6	0.425		

**Table S22** Amplitude (a) and lifetime ( $\tau$ ) parameters for **3CzCNPyz** 0.1 wt% zeonex film.  $R^2$  for PF is 0.98609 and for DF is 0.93666 and 0.99254 for the 80 K PF. CT stands for charge transfer state.

Temperature	aPF/CT	$\tau$ PF/CT	aDF/CT	$\tau$ DF/CT
RT	7.514E7 $\pm$	1.006E1 $\pm$	9.649E1 $\pm$	3.341E6 $\pm$
	0.362E7	0.042	0.268E1	0.258E6
80 K	1.139E8 $\pm$	8.870 $\pm$		
	0.040E8	0.264		

**Table S23** Amplitude (a) and lifetime ( $\tau$ ) parameters for **4CzPyz** 0.1 wt% zeonex film.  $R^2$  for Prompt is 0.99792 and for delayed is 0.91786 and 0.99954 for the 80 K prompt. CT stands for charge transfer state.

Temperature	aPF/CT	$\tau$ PF/CT	aDF/CT	$\tau$ DF/CT
RT	8.434E7 $\pm$	5.950 $\pm$	1.885E1 $\pm$	3.495E6 $\pm$
	0.188E7	0.099	0.075E1	0.281E6
80 K	8.311E7 $\pm$	5.303 $\pm$		
	0.096E7	0.045		

**Table S24** Amplitude (a) and lifetime ( $\tau$ ) parameters for **2Cz2CNPyz** 0.01 wt% zeonex film.  $R^2$  for PF is 0.99923 and for DF is 0.96278 and 0.99885 for the 80 K PF. LE stands for locally excited state and CT stands for charge transfer state.

Temperature	aPF/LE	$\tau$ PF/LE	aPF/CT	$\tau$ PF/CT	aDF/CT	$\tau$ DF/CT
RT	3.448E7 $\pm$	1.318 $\pm$	2.675E6 $\pm$	4.891 $\pm$ 0.672	1.690E3 $\pm$	1.289E4 $\pm$
	0.370E7	0.126	0.892E6		0.449E3	0.645E4
80 K	1.866E7 $\pm$	1.811 $\pm$	2.832E6 $\pm$	6.486 $\pm$ 0.816		
	0.137E7	0.195	0.820E6			

## 9. Theoretical Study

### Computational details

Ground-state geometry optimizations of **2Cz2CNPyz**, **3CzCNPyz** and **4CzPyz** were performed *in vacuo*, using density-functional theory (DFT).<sup>12</sup> We employed the PBE0<sup>13</sup> exchange-correlation functional along with the def2-SVP<sup>14</sup> basis set and Grimme's D3 dispersion correction<sup>15</sup> with Becke-Johnson damping<sup>16</sup> – the level of theory is denoted as PBE0-D3BJ/def2-SVP.

Singlet and triplet excited states were computed *in vacuo*, with linear-response time-dependent density-functional theory (LR-TDDFT)<sup>17,18</sup> using the Tamm-Dancoff approximation.<sup>19</sup> Vertical excitation energies were calculated with PBE0/def2-SVP and  $\omega$ B97XD<sup>20</sup>/def2-SVP, while excited-state geometry optimizations were performed with PBE0-D3BJ/def2-SVP. Note that the dispersion correction does not affect single-point calculations, but only geometry optimizations. Although the D3 dispersion correction is designed for the ground state, it is often employed in the context of excited states.<sup>21</sup> Nevertheless, we verified that excited-state optimizations with and without dispersion correction yield very similar emission energies. Ground and excited-state frequencies were also computed to estimate  $E_{0-0}$  transition energies.

Excitation energies from LR-TDDFT were compared to the wavefunction-based second-order algebraic diagrammatic construction method, ADC(2),<sup>22,23</sup> used along with def2-SVPD<sup>24</sup> basis set. ADC(2) calculations employed the resolution of the identity and frozen-core approximations. We note that the D1 diagnostic was around 0.05 for all three molecules, which is slightly higher than the recommended limit value of 0.04,<sup>25</sup> although this limit was recently deemed as too conservative.<sup>26</sup>

PBE0 and ADC(2) electronic structure calculations were performed with Turbomole 7.4.0 program package,<sup>27</sup> while Gaussian09<sup>28</sup> was used for  $\omega$ B97XD. To analyse the characters of the LR-

TDDFT transitions, natural transition orbitals (NTO) and charge transfer numbers were computed with TheoDRE 1.5.1 package.<sup>29</sup> Structures and orbitals were visualized with VMD 1.9.2.<sup>30</sup>

## Supporting calculations

The optimized ground-state minima of **2Cz2CNPyz** and **3CzCNPyz** resemble structures from the crystal (see Figures S13 and S16). For **4CzPyz** we found two conformers that are close in energy (Figure S57), with conformer **A** being 0.17 eV more stable. However, conformer **B** corresponds to the crystal structure geometry (see Figure S19). Conformer **A** may be less likely to crystallize due to its propeller-like structure, which also implicates axial chirality. Double peaked photoluminescence (Figure 2) implies that both conformers are present in solution (see discussion below).

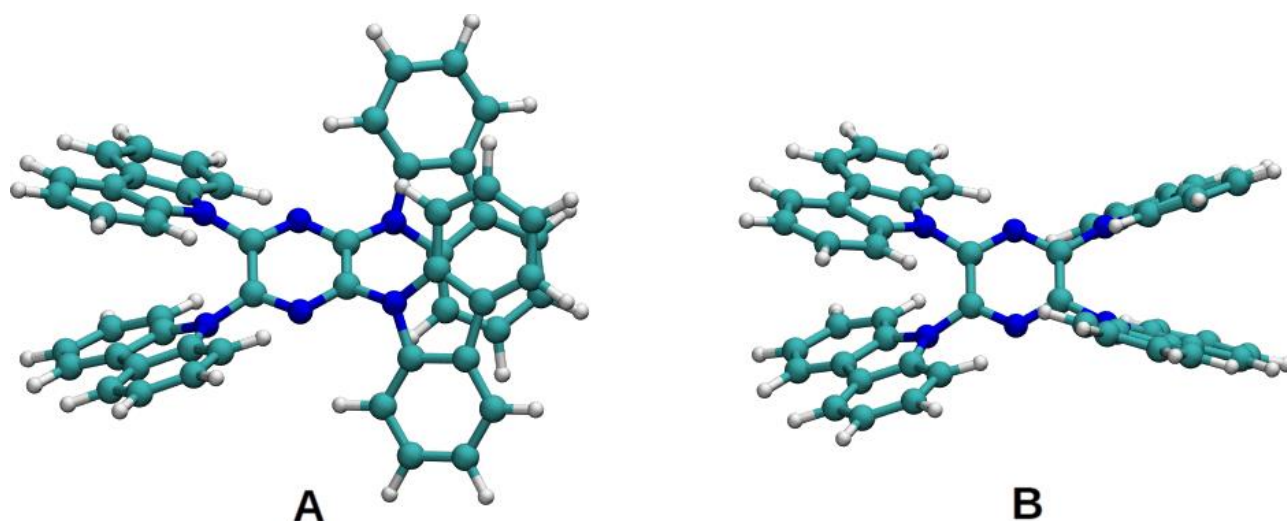


**Figure S57** Ground state conformers of **4CzPyz**.

Tables S25 and S26 compare vertical excitation energies of the lowest singlet and triplet excited states, respectively, computed with different levels of theory. Apart from the energy shifts, the trends are consistent for all three methods. **3CzCNPyz** has the lowest transition energy to  $S_1$ , while **2Cz2CNPyz** and **4CzPyz** have higher vertical transition to this state, both in the same energy range. **3CzCNPyz** exhibits the lowest  $T_1$  state (at the ground-state optimized geometry), followed by

**2Cz2CNPyz** and **4CzPyz**. PBE0 energies are in good agreement with ADC(2), although it is expected that hybrid functional will underestimate singlet excited states with a partial charge-transfer (CT) character (Figure S58). This is partly compensated by the small basis set and the upshift from the Tamm-Dancoff approximation, which is likely the reason why range-separated functional,  $\omega$ B97XD, overestimates the energy of the singlet transitions. We note that singlet-triplet gaps are difficult to predict accurately by electronic structure methods, and to facilitate the comparison with experimental estimates it is often necessary to sample many different conformations.<sup>31</sup>

**Table S25** Vertical absorption energies to  $S_1$  state. Energies are in eV and oscillator strengths are given between parentheses.

	<b>2Cz2CNPyz</b>	<b>3CzCNPyz</b>	<b>4CzPyz (A / B)</b>
PBE0	3.06 (0.059)	2.94 (0.064)	3.15 (0.370) / 3.08 (0.256)
$\omega$ B97XD	3.67 (0.252)	3.59 (0.226)	3.68 (0.578) / 3.69 (0.435)
ADC(2)	3.13 (0.184)	2.99 (0.131)	3.10 (0.345) / 3.08 (0.263)

**Table S26** Vertical absorption energies to  $T_1$  state. Energies are in eV.

	<b>2Cz2CNPyz</b>	<b>3CzCNPyz</b>	<b>4CzPyz (A / B)</b>
PBE0	2.58	2.43	2.62 / 2.68
$\omega$ B97XD	2.95	2.78	2.95 / 3.07
ADC(2)	2.88	2.71	2.90 / 2.93

The lowest singlet and triplet excited states are all of  $\pi\pi^*$  character (Figure S57), with a similar nodal structure for all three compounds. Some degree of  $n\pi^*$  character appears, most notably in

**2Cz2CNPyz**, which is likely due to the out-of-plane distortion of the pyrazine ring. The highest occupied NTO (HONTO) is delocalized on both the pyrazine and carbazole rings, while the lowest unoccupied NTO (LUNTO) is mostly localized on the pyrazine. Partial CT character with still a good orbital overlap is an important trade-off for TADF systems, since the former controls the singlet-triplet gap, while the latter ensures non-vanishing oscillator strengths.<sup>32</sup>

Charge transfer numbers for singlet and triplet excited states were computed (following Plasser<sup>29</sup>) between donor (carbazole) and acceptor (pyrazine, nitrile) groups, and listed in Table S27. Value of 1 means complete charge separation, while value of 0 means LE character. Singlet CT character is slightly overestimated by PBE0, as compared to ADC(2). In general, triplet states are more localized than singlet states, with character between CT and LE.

**Table S27** Charge transfer numbers for PBE0 and ADC(2) excitations.

		<b>2Cz2CNPyz</b>	<b>3CzCNPyz</b>	<b>4CzPyz (A / B)</b>
PBE0	S <sub>1</sub>	0.732	0.808	0.750/0.786
	T <sub>1</sub>	0.542	0.614	0.605/0.653
ADC2	S <sub>1</sub>	0.661	0.701	0.668/0.730
	T <sub>1</sub>	0.558	0.582	0.621/0.669

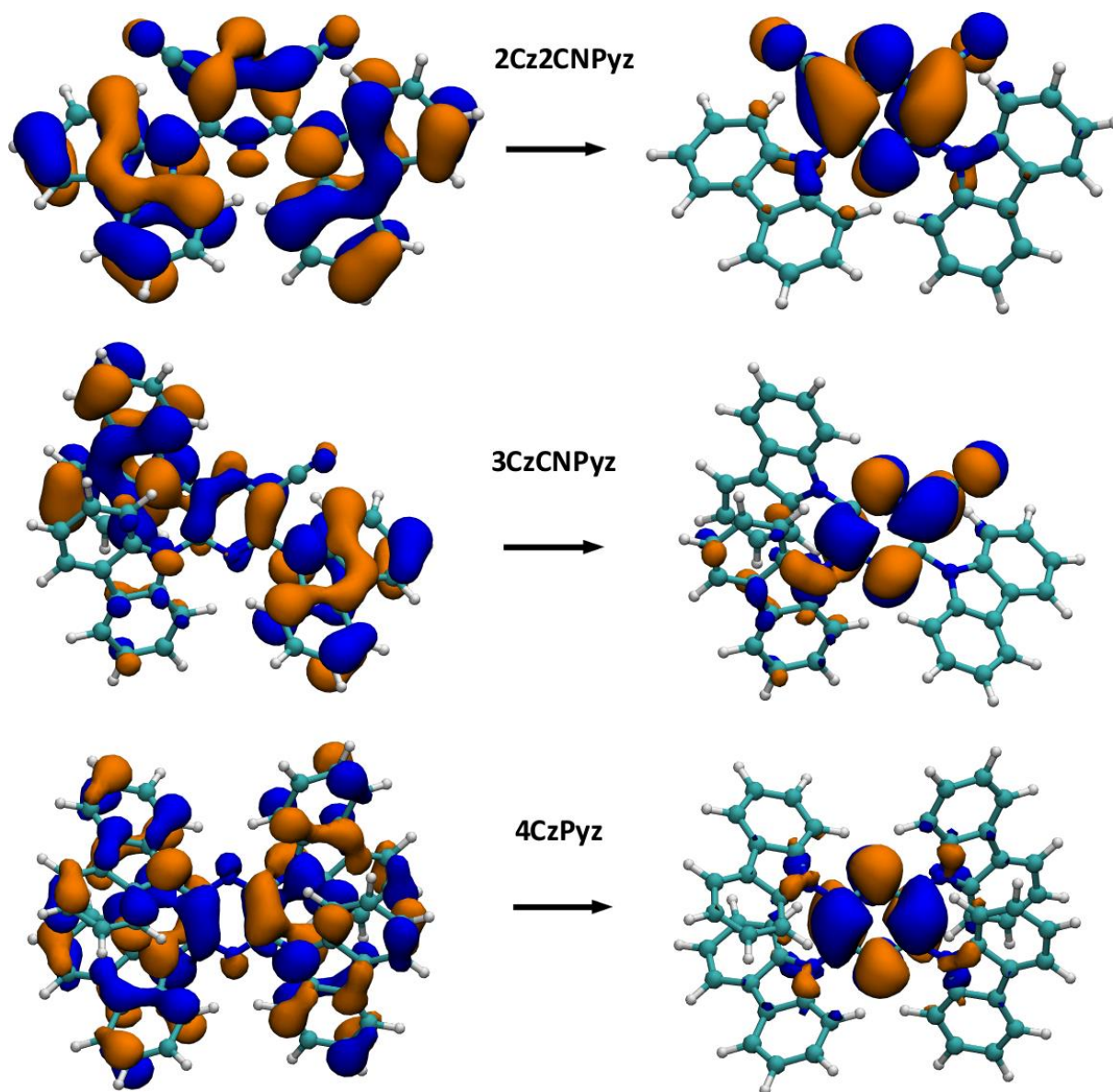


**Figure S58** HONTO (left) and LUNTO (right) orbitals involved in  $S_1$  transitions of three compounds. The corresponding  $T_1$  NTOs exhibit the same nodal structure, although in case of triplets HONTO orbitals are slightly less delocalized to carbazole groups. PBE0/def2-SVP level; isovalue=0.02.

Vertical emission energies are reported in Table S28. For **4CzPyz** distinct excited-state minima could be optimized for the **A** and **B** conformers. In the  $S_1$  state, the conformer **A** is only 0.02 eV more stable than conformer **B**, indicating an easy interconversion, while in  $T_1$  the difference is 0.19 eV in favour of conformer **A**. The calculated singlet emission energies may be compared with the photoluminescence in non-polar MCH solvent (Figure 2). The experimental maxima are approximately

peaked at 2.35, 2.45 and 2.6/2.7 eV for **2Cz2CNPyz**, **3CzCNPyz** and **4CzPyz** (two maxima), respectively. This trend is not fully reproduced by the computed results reported in Table S28. However, it is known that vertical absorption and emission energies do not strictly correspond to experimental band maxima,<sup>33,34</sup> and (among other reasons) the intrinsic energy shift arises due to the difference between ground and excited-state frequencies.<sup>34</sup> For that reason, we compute  $E_{0-0}$  transitions (Table S29), which excellently reproduce the experimental trends: the emission of **3CzCNPyz** being slightly blue-shifted with respect to the one of **2Cz2CNPyz** and red-shifted from the double-peaked **4CzPyz** emission.

**Table S28** Vertical emission energies from  $T_1$  and  $S_1$  minima. PBE0-D3BJ/def2-SVP level; energies in eV.

	<b>2Cz2CNPyz</b>	<b>3CzCNPyz</b>	<b>4CzPyz (A / B)</b>
$T_1$	1.71	1.81	1.90 / 2.15
$S_1$	1.83	1.69	2.20 / 2.09

**Table S29**  $E_{0-0}$  transitions between  $S_1$  and the ground state. PBE0-D3BJ/def2-SVP level; energies in eV

	<b>2Cz2CNPyz</b>	<b>3CzCNPyz</b>	<b>4CzPyz (A / B)</b>
$E_{0-0}$	2.26	2.36	2.75 / 2.61

## 10. References

- (1) Perrin, D. D.; Armarego, W. L. F. *Purification of Laboratory Chemicals*, 3rd Edition.; Pergamon Press: Oxford, 1988.
- (2) Uoyama, H.; Goushi, K.; Shizu, K.; Nomura, H.; Adachi, C. Highly Efficient Organic Light-Emitting Diodes from Delayed Fluorescence. *Nature* **2012**, *492*, 234–238.
- (3) Etherington, M. K.; Kukhta, N. A.; Higginbotham, H. F.; Danos, A.; Bismillah, A. N.; Graves, D. R.; McGonigal, P. R.; Haase, N.; Morherr, A.; Batsanov, A. S.; Pflumm, C.; Bhalla, V.; Bryce, M. R.; Monkman, A. P. Persistent Dimer Emission in Thermally Activated Delayed Fluorescence Materials. *J. Phys. Chem. C* **2019**, *123*, 11109–11117.
- (4) Dolomanov, O. V.; Bourhis, L. J.; Gildea, R. J.; Howard, J. A. K.; Puschmann, H. OLEX2: A Complete Structure Solution, Refinement and Analysis Program. *J. Appl. Crystallogr.* **2009**, *42*, 339–341.
- (5) Sheldrick, G. M. A Short History of SHELX. *Acta Crystallogr. Sect. A Found. Crystallogr.* **2008**, *64*, 112–122.
- (6) Tang, C.; Bi, R.; Tao, Y.; Wang, F.; Cao, X.; Wang, S.; Jiang, T.; Zhong, C.; Zhang, H.; Huang, W. A Versatile Efficient One-Step Approach for Carbazole–Pyridine Hybrid Molecules: Highly Efficient Host Materials for Blue Phosphorescent OLEDs. *Chem. Commun.* **2015**, *51*, 1650–1653.
- (7) Spackman, M. A.; Jayatilaka, D. Hirshfeld Surface Analysis. *CrystEngComm* **2009**, *11*, 19–32.
- (8) Turner, M. J.; McKinnon, J. J.; Wolff, S. K.; Grimwood, D. J., Spackman, P. R., Jayatilaka, D.; Spackman, M. A. Crystal Explorer17. University of Western Australia 2017.
- (9) Cao, X.; Zhang, X.; Duan, C.; Xu, H.; Yuan, W.; Tao, Y.; Huang, W. Simple Phenyl Bridge between Cyano and Pyridine Units to Weaken the Electron-Withdrawing Property for Blue-Shifted Emission in Efficient Blue TADF OLEDs. *Org. Electron.* **2018**, *57*, 247–254.
- (10) Zhang, D.; Cao, X.; Wu, Q.; Zhang, M.; Sun, N.; Zhang, X.; Tao, Y. Purely Organic Materials for Extremely Simple All-TADF White OLEDs: A New Carbazole/Oxadiazole Hybrid Material as a Dual-Role Non-Doped Light Blue Emitter and Highly Efficient Orange Host. *J. Mater. Chem. C* **2018**, *6*, 3675–3682.
- (11) Tang, C.; Yang, T.; Cao, X.; Tao, Y.; Wang, F.; Zhong, C.; Qian, Y.; Zhang, X.; Huang, W. Tuning a Weak Emissive Blue Host to Highly Efficient Green Dopant by a CN in Tetracarbazolepyridines for Solution-Processed Thermally Activated Delayed Fluorescence Devices. *Adv. Opt. Mater.* **2015**, *3*, 786–790.
- (12) Parr, R. G.; Yang, W. *Density Functional Theory of Atoms and Molecules*; Oxford University Press, 1989.
- (13) Adamo, C.; Barone, V. Toward Reliable Density Functional Methods without Adjustable Parameters: The PBE0 Model. *J. Chem. Phys.* **1999**, *110*, 6158.
- (14) Weigend, F.; Ahlrichs, R. Balanced Basis Sets of Split Valence, Triple Zeta Valence and Quadruple Zeta Valence Quality for H to Rn: Design and Assessment of Accuracy. *Phys. Chem. Chem. Phys.* **2005**, *7*, 3297–3305.

- (15) Grimme, S.; Antony, J.; Ehrlich, S.; Krieg, H. A Consistent and Accurate Ab Initio Parametrization of Density Functional Dispersion Correction (DFT-D) for the 94 Elements H-Pu. *J. Chem. Phys.* **2010**, *132*, 154104.
- (16) Grimme, S.; Ehrlich, S.; Goerigk, L. Effect of the Damping Function in Dispersion Corrected Density Functional Theory. *J. Comput. Chem.* **2011**, *32*, 1456–1465.
- (17) Runge, E.; Gross, E. K. U. Density-Functional Theory for Time-Dependent Systems. *Phys. Rev. Lett.* **1984**, *52*, 997–1000.
- (18) Casida, M. E. Time-Dependent Density Functional Response Theory for Molecules. In *Recent Advances in Density Functional Methods*; Chong, D. P., Ed.; World Scientific: Singapore, 1995; pp 155–192.
- (19) Hirata, S.; Head-Gordon, M. Time-Dependent Density Functional Theory within the Tamm–Dancoff Approximation. *Chem. Phys. Lett.* **1999**, *314*, 291–299.
- (20) Chai, J.-D.; Head-Gordon, M. Long-Range Corrected Hybrid Density Functionals with Damped Atom–Atom Dispersion Corrections. *Phys. Chem. Chem. Phys.* **2008**, *10*, 6615.
- (21) Fabrizio, A.; Corminboeuf, C. How Do London Dispersion Interactions Impact the Photochemical Processes of Molecular Switches? *J. Phys. Chem. Lett.* **2018**, *9*, 464–470.
- (22) Trofimov, A. B.; Schirmer, J. An Efficient Polarization Propagator Approach to Valence Electron Excitation Spectra. *J. Phys. B At. Mol. Opt. Phys.* **1995**, *28*, 2299–2324.
- (23) Dreuw, A.; Wormit, M. The Algebraic Diagrammatic Construction Scheme for the Polarization Propagator for the Calculation of Excited States. *Wiley Interdiscip. Rev. Comput. Mol. Sci.* **2015**, *5*, 82–95.
- (24) Rappoport, D.; Furche, F. Property-Optimized Gaussian Basis Sets for Molecular Response Calculations. *J. Chem. Phys.* **2010**, *133*, 134105.
- (25) Janssen, C. L.; Nielsen, I. M. B. New Diagnostics for Coupled-Cluster and Møller–Plesset Perturbation Theory. *Chem. Phys. Lett.* **1998**, *290*, 423–430.
- (26) Tuna, D.; Lefrancois, D.; Wolański, Ł.; Gozem, S.; Schapiro, I.; Andruniów, T.; Dreuw, A.; Olivucci, M. Assessment of Approximate Coupled-Cluster and Algebraic-Diagrammatic-Construction Methods for Ground- and Excited-State Reaction Paths and the Conical-Intersection Seam of a Retinal-Chromophore Model. *J. Chem. Theory Comput.* **2015**, *11*, 5758–5781.
- (27) Furche, F.; Ahlrichs, R.; Hättig, C.; Klopper, W.; Sierka, M.; Weigend, F. Turbomole. *Wiley Interdiscip. Rev. Comput. Mol. Sci.* **2014**, *4*, 91–100.
- (28) Frisch, M. J.; Trucks, G. W.; Schlegel, H. B.; Scuseria, G. E.; Robb, M. A.; Cheeseman, J. R.; Scalmani, G.; Barone, V.; Mennucci, B.; Petersson, G. A.; Katsuji, H. N.; Caricato, M.; Li, X.; Hratchian, H. P.; Izmaylov, A. F.; Bloino, J.; Zheng, G.; Sonnenberg, J. L.; Hada, M.; Ehara, M.; Toyota, K.; Fukuda, R.; Segawa, J. H.; Ishida, M.; Nakajima, T.; Honda, Y.; Kitao, O.; Nakai, H.; Vreven, T.; J. A. Montgomery, J.; Peralta, J. E.; Ogliaro, F.; Bearpark, M.; Heyd, J. J.; Brothers, E.; Kudin, K. N.; Staroverov, V. N.; Kobayashi, R.; Normand, J.; Ghavachari, K. R.; Rendell, A.; Burant, J. C.; Iyengar, S. S.; Tomasi, J.; Cossi, M.; Rega, N.; Millam, J. M.; Klene, M.; Knox, J. E.; Cross, J. B.; Bakken, V.; Adamo, C.; Jaramillo, J.; Gomperts, R.; Stratmann, R. E.; Yazyev, O.; Austin, A. J.; Cammi, R.; Pomelli, C.; Ochterski, J. W.; Martin, R. L.; Morokuma, K.; Zakrzewski, V. G.; Voth, G. A.; Salvador, P.; Dannenberg, J. J.; Dapprich, S.; Daniels, A. D.; Farkas, Ö.; Foresman, J. B.; Ortiz, J. V.; Cioslowski, J.; Fox, D. J. Gaussian 09, Revision D.01. Gaussian Inc., Wallingford, CT 2009.

- (29) Plasser, F. TheoDORÉ: A Toolbox for a Detailed and Automated Analysis of Electronic Excited State Computations. *J. Chem. Phys.* **2020**, *152*, 084108.
- (30) Humphrey, W.; Dalke, A.; Schulten, K. VMD: Visual Molecular Dynamics. *J. Mol. Graph.* **1996**, *14*, 33–38.
- (31) Weissenseel, S.; Drigo, N. A.; Kudriashova, L. G.; Schmid, M.; Morgenstern, T.; Lin, K.-H.; Prlj, A.; Corminboeuf, C.; Sperlich, A.; Brütting, W.; Nazeeruddin, M. K.; Dyakonov, V. Getting the Right Twist: Influence of Donor–Acceptor Dihedral Angle on Exciton Kinetics and Singlet–Triplet Gap in Deep Blue Thermally Activated Delayed Fluorescence Emitter. *J. Phys. Chem. C* **2019**, *123*, 27778–27784.
- (32) Chen, X.; Tsuchiya, Y.; Ishikawa, Y.; Zhong, C.; Adachi, C.; Brédas, J. A New Design Strategy for Efficient Thermally Activated Delayed Fluorescence Organic Emitters: From Twisted to Planar Structures. *Adv. Mater.* **2017**, *29*, 1702767.
- (33) Laurent, A. D.; Jacquemin, D. TD-DFT Benchmarks: A Review. *Int. J. Quantum Chem.* **2013**, *113*, 2019–2039.
- (34) Bai, S.; Mansour, R.; Stojanović, L.; Toldo, J. M.; Barbatti, M. On the Origin of the Shift between Vertical Excitation and Band Maximum in Molecular Photoabsorption. *J. Mol. Model.* **2020**, *26*, 107.